Alma Mater Studiorum - Università di Bologna

DOTTORATO DI RICERCA IN

AUTOMOTIVE PER UNA MOBILITÀ INTELLIGENTE

Ciclo 34

Settore Concorsuale: 09/C1 - MACCHINE E SISTEMI PER L'ENERGIA E L'AMBIENTE

Settore Scientifico Disciplinare: ING-IND/08 - MACCHINE A FLUIDO

DEVELOPMENT OF PREDICTIVE ENERGY MANAGEMENT STRATEGIES FOR HYBRID ELECTRIC VEHICLES SUPPORTED BY CONNECTIVITY

Presentata da: Alessandro Capancioni

Coordinatore Dottorato

Nicolò Cavina

Supervisore

Nicolò Cavina

Esame finale anno 2022

A tutti coloro che hanno creduto in me.

A smooth sea never made a skilled sailor.

[Franklin D. Roosevelt]

Abstract

Nowadays, the spreading of the air pollution crisis enhanced by greenhouse gases emission is leading to the worsening of the global warming. In this context, the transportation sector plays a vital role, since it is responsible for a large part of carbon dioxide production.

In order to address these issues, the present thesis deals with the development of advanced control strategies for the energy efficiency optimization of plug-in hybrid electric vehicles (PHEVs), supported by the prediction of future working conditions of the powertrain.

In particular, a Dynamic Programming algorithm has been developed for the combined optimization of vehicle energy and battery thermal management. At this aim, the battery temperature and the battery cooling circuit control signal have been considered as an additional state and control variables, respectively. Moreover, an adaptive equivalent consumption minimization strategy (A-ECMS) has been modified to handle zero-emission zones, where engine propulsion is not allowed.

Navigation data represent an essential element in the achievement of these tasks. With this aim, a novel simulation and testing environment has been developed during the PhD research activity, as an effective tool to retrieve routing information from map service providers via vehicle-to-everything connectivity.

Comparisons between the developed and the reference strategies are made, as well, in order to assess their impact on the vehicle energy consumption.

All the activities presented in this doctoral dissertation have been carried out at the *Green Mobility Research Lab* (GMRL), a research center resulting from the partnership between the University of Bologna and FEV Italia s.r.l., which represents the industrial partner of the research project.

Keywords

hybrid electric vehicles (HEVs) · Software-in-the-Loop (SiL) · Hardware-in-the-Loop (HiL) · vehicle-to-everything (V2X) · zero-emission zone (ZEZ) · predictive functions · energy management · equivalent consumption minimization strategy (ECMS) · dynamic programming (DP)

Acknowledgments

Mamma, Babbo,
Bea, Whisky, tutta la famiglia, Lize, Gab,
Vez, GMRLab, DIN, sala prove motori, Stefano, Faustino e gli
elettricisti, DIVIncenzo, FEV, Alma Mater Studiorum - Università
di Bologna, gli amici di Giù, Valle di Preda, Falentex House, Escape
con el Room, Edimbraaaa, Engedinnerini, le domeniche d'Agosto,
I ciuffolotti sono belli, Frati di Trimoni, i Pranzi dei Poeti, Bologna,
Via del Pratello, il biliardino del Caffè De Marchi, i Gini Tonici
di Jiani's Bar, Jimmy di Bar Jimmy, gli Spritz del Venerdi del
Barazzo, la Cotoletta del Bocconcino, Bar il Piratello, ex-Bar
da Nico, Indegna - La crescentina 2.0, Bar Anarchico,
ex Stomp, Il Cucchiaio d'Oro, Bar Miky & Max,
Lilium Caffè, Babilonia, Trattoria Da Vito, TPO,
Parco del Cavaticcio, Biografilm Festival,
BOtanique, ex Mikasa, Mercato
Sonato, Cumbiamberos,
Estragon Club,
Làbas

Contents

List of figures

List of tables

Nomenclature

Acronyms

4WD	Four-Wheel Driving
A-ECMS	Adaptive-ECMS
ACC	Air-Conditioning Compressor
ADAS	Advanced Driver Assistance System
BEV	Battery Electric Vehicle
BMS	Battery Management System
BTM	Battery Thermal Management
BVM	Backward Vehicle Model
c-HiL	Connected HiL
CAHEV	Connected Autonomous HEV
CAV	Connected Autonomous Vehicles
CB	Charge Blended
CD	Charge Depleting
CG	Central Gateway
CI	Charge Increasing
CS	Charge Sustaining
CW	(Traffic) Code Weight
DDP	Discrete Dynamic Programming
DP	Dynamic Programming
ECMS	Equivalent Consumption Minimization Strategy
ECU	Electronic Control Unit
EM	Electric Motor
EMS	Energy Management Strategy

EV	Electric Vehicle
FC	Fuel Consumption
HCU	Hybrid Control Unit
HD	Hybridization Degree
HEV	Hybrid Electric Vehicle
HiL	Hardware-in-the-Loop
HMI	Human-Machine Interface
HV	High-Voltage
ICE	Internal Combustion Engine
ISG	Integrated Starter Generator
ITS	Intelligent Transport Systems
KPI	Key Performance Indicator
LEZ	Low-Emission Zone
LV	Low-Voltage
MAE	Mean Absolute Error
MAS	Maximum Allowable Speed
MiL	Model-in-the-Loop
MPC	Model-Predictive Control
MSP	Map Server Provider
NEDC	New European Drive Cycle
OBC	On-Board Charger
OBU	On-Board Unit
OCV	Open Circuit Voltage
OVC	Off-Vehicle Charger
PF	Predictive Function
PHEV	Plug-in HEV
PMP	Pontryagin's Minimum Principle
PTC	Positive Temperature Coefficient
RBS	Rule-Based Strategy
RDE	Real-Driving Emissions (test)
RESS	Rechargeable Energy Storage System
RMSE	Root-Mean-Square Error
RSU	Road Side Unit

SAE	Society of Automotive Engineers
SiL	Software-in-the-Loop
SoC	State of Charge
SoH	State of Health
SPP	Speed Profile Prediction
TAT	Turnaround Time
TeCU	Telecommunication Control Unit
ULEZ	Ultra Low-Emission Zone
V2C	Vehicle-To-Cloud
V2I	Vehicle-To-Infrastructure
V2N	Vehicle-To-Network
V2V	Vehicle-To-Vehicle
V2X	Vehicle-To-Everything
WLTP	Worldwide harmonized Light vehicles Test Procedure
ZEZ	Zero-Emission Zone

Roman symbols

$a(\cdot)$	Adaptive term of the equivalence factor [-]
A_h	Amplitude of the h-th harmonic of the noise-related MAS [km/h]
$a_{a,\max}$,$a_{d,\max}$	Vehicle maximum acceleration/deceleration [m/s^2]
b_{ECMS}	Control signal of ECMS activation [-]
$BSFC(\cdot)$	Brake specific fuel consumption [kg/J]
$CO_{2,c}$	Corrected CO_2 production [g/km]
$C_1(\cdot)$	Capacitance of the RC circuit [F]
$C_n(\cdot)$	Battery nominal capacity [Ah]
c_p	Battery pack specific heat capacity (at constant pressure) [J/(kg·K)]
COP	Coefficient of performance of the refrigerant cycle [-]
CW	Traffic code weight [-]
CO_2	CO_2 production [g/km]
$d(\cdot)$	Traveled distance [km]
d_i,d_f	Initial/final distance delimiting CB mode [km]
$d_{i,Z}$,$d_{f,Z}$	Initial/final distance delimiting the ZEZ [km]

d_Z	ZEZ length [km]
$F(\cdot)$	Force [N]
f_0,f_1,f_2	Coast-down parameters [N], [N/(km/h)], [N/(km/h)^2]
f_h	Frequency of the h-th harmonic of the noise-related MAS [1/m]
$F_r(\cdot)$	Force acting on the wheels [N]
	Rolling friction force [N]
$F_a(\cdot)$	Aerodynamic friction force [N]
$F_g(\cdot)$	Gravitational force [N]
$F_{I^+}(\cdot)$,$F_{I^-}(\cdot)$	Positive/negative inertial force [N]
$F_{mot}(\cdot)$	Propulsion force for vehicle traction [N]
$F_{res}(\cdot)$	Resistant force acting on the vehicle [N]
$F_{RL}(\cdot)$	Road load [N]
$\mathbf{g}$	Vector of the discretized engaged gear [-]
g	Gravitational acceleration [m/s^2]
	Engaged gear [-]
H	Number of dominant harmonics of the noise-related MAS [-]
h_a	Convective heat transfer coefficient of the environmental air [W/(K·m^2)]
h_c	Convective heat transfer coefficient of the battery coolant [W/(K·m^2)]
$I_b(\cdot)$	Battery current [A]
$I_c(\cdot)$	Cell current [A]
$I_{ACC}(\cdot)$	Air-conditioning HV compressor current [A]
$I_{DCDC}(\cdot)$	DCDC current [A]
$I_{EM}(\cdot)$	Electric motors current [A]
$I_{ISG}(\cdot)$	ISG current [A]
$I_{OBC}(\cdot)$	OBC current [A]
$I_{PTC}(\cdot)$	HV PTC current [A]
I_p	Pulse test current [A]
$J(x_0,u)$,$J(x_0,u^*)$	Admissible/minimum cost for the optimal problem
$J(x_k,u_k)$	Cost-to-go
k	Discrete time index (or stage)
$k_a(\cdot)$	Adaptive factor [-]

k_a,k_d	Reductive factor of the vehicle maximum acceleration/deceleration [-]
k_p	Penalty factor [-]
k_{CO_2}	CO_2 conversion factor [g_{CO_2}/l_{fuel}]
L_k	Arc or instantaneous cost
L_N	Cost associated to the last stage
$\dot{m}_c$	Battery coolant mass flow rate [kg/s]
$\dot{m}_{f,b}(\cdot)$	Virtual fuel mass flow rate associated to battery usage [kg/s]
$\dot{m}_{f,eq}(\cdot)$	Equivalent fuel mass flow rate [kg/s]
$\dot{m}_f(\cdot)$	Fuel mass flow rate [kg/s]
m	Battery mass [kg]
m_f	Fuel mass [kg]
m_v	Vehicle mass [kg]
$m_{f,c}$	Corrected fuel consumption [kg]
MAS	Vehicle maximum allowable speed [km/h]
MAS_n	Noise-related MAS [km/h]
MAS_r	Reference MAS [km/h]
N	Number of sub-segments of the speed profile prediction [-] Number of iterations of the backward vehicle model [-] Number of stages of the DP-based optimization algorithm [-]
$n(\cdot)$	Engine revolution speed [rpm]
N_h	Number of magnitudes for each harmonic [-]
n_p	Number of cells strings [-]
N_s	Number of segments [-]
n_s	Number of series-connected cells [-]
$n_w(\cdot)$	Wheels revolution speed [rpm]
$P(\cdot)$	Power [W]
$p(\cdot)$	Penalty term of the equivalence factor [-]
$P_b(\cdot)$	Battery net power output [W]
$P_c(\cdot)$	Battery cooling power request [W]
P_{aux}	Auxiliary power [W]
$P_{b,loss}(\cdot)$	Battery power losses [W]
$p_{bme}(\cdot)$	Brake mean effective pressure [bar]

$P_{el}(\cdot)$	Electrical power [W]
P_{eP}	Electrical pump power [W]
$P_{fuel}(\cdot)$	Chemical power associated to the fuel [W]
$P_{mech}(\cdot)$	Mechanical net power at the crankshaft [W]
	Mechanical power [W]
$\dot{Q}_{air}(\cdot)$	Thermal power related to the air-battery convective heat exchange [W]
$\dot{Q}_{cool}(\cdot)$	Cooling heat rate due to battery-coolant convective heat exchange [W]
Q	Maximum speed [km/h]
Q_{lhv}	Fuel lower heating value [J/kg]
$R_0(\cdot)$	Ohmic resistance [Ω]
$R_1(\cdot)$	Resistance of the RC circuit [Ω]
r_w	Wheel radius [m]
$s(\cdot)$	Equivalence factor [-]
S_a	Surface of the air-battery convective heat transfer [m^2]
S_c	Surface of the battery-coolant convective heat transfer [m^2]
$\mathbf{T}_s$	Vector of the discretized load point shifting torque [Nm]
$T(\cdot)$	Torque [Nm]
$T_r(\cdot)$	Torque request at the wheels [Nm]
$T_s(\cdot)$	Engine load point shifting torque [Nm]
$T_{EM}(\cdot)$	Electric machines torque [Nm]
$T_{fr}(\cdot)$	Engine friction torque [Nm]
$T_{ICE}(\cdot)$	Internal combustion engine torque [Nm]
$T_{in}(\cdot)$	Engine indicated torque [Nm]
$T_q(\cdot)$	Driver torque request [Nm]
$T_{t,in}(\cdot)$	Torque request at the transmission input [Nm]
$T_{w,f}(\cdot)$,$T_{w,r}(\cdot)$	Torque request at the front/rear wheels [Nm]
$T_w(\cdot)$	Driver torque request at the wheels [Nm]
t	Time [s]
t_i,t_f	Initial/final time instant delimiting CB mode [s]
t_s	Computational time step [s]
$t_u(\cdot)$	Update time [s]

t_{exp}	Data acquisition time [s]
$t_{i,Z}$,$t_{f,Z}$	ZEZ entrance/exit time instant [s]
$\mathbf{u}$	Control variables vector
$\mathbf{u}_c$	Vector of the discretized control signal of battery cooling [-]
$\mathbf{u}_E$,$\mathbf{u}_T$,$\mathbf{u}_C$	Control variables vector of the energy/thermal/combined-DP
$\mathbf{u}_s$	Vector of the discretized torque split factor [-]
U	Set of all admissible control policies
u,u^*	Admissible/optimal control policy for the optimal problem
$u_s(\cdot)$	Torque split factor [-]
$\dot{V}_c$	Battery coolant volume flow rate [m^3/s]
$\mathbf{v}$	Predicted vehicle speed profile [km/h]
V	Predicted speed [km/h]
$v(\cdot)$	Vehicle longitudinal speed [km/h]
$V_0(\cdot)$	Voltage drop related to the ohmic resistance [V]
$V_1(\cdot)$	Voltage drop related to the RC circuit [V]
$V_b(\cdot)$	Battery voltage [V]
$V_c(\cdot)$	Cell voltage [V]
V_d	Engine displacement [m^3]
V_{lim}	Legal speed limit [km/h]
$V_{OC}(\cdot)$	Open circuit voltage [V]
$\mathbf{w}$	Disturbance vector
$W(\cdot)$	Work [J]
$\mathbf{x}$	State variables vector
$\mathbf{x}_E$,$\mathbf{x}_T$,$\mathbf{x}_C$	State variables vector of the energy/thermal/combined-DP

Greek symbols

$\alpha(\cdot)$	Angle of slope [rad]
$\alpha_{\%}(\cdot)$	Percentage road slope [%]
$\boldsymbol{\alpha}_{\%}$	Predicted road slope profile [%]
γ	Gear ratio [-]
$\bar{\eta}_{EM}$	Electric motors average efficiency [-]
$\bar{\eta}_{ICE}$	Engine average efficiency [-]

$\bar{\eta}_{ISG}$	ISG average efficiency [-]
η	Efficiency [-]
η_{ch}	Chiller efficiency [-]
η_c	Coulombic efficiency [-]
η_{DCDC}	DCDC efficiency [-]
$\eta_{tot}(\cdot)$	Engine total efficiency [-]
$\eta_t(\cdot)$	Transmission efficiency [-]
$\boldsymbol{\vartheta}$	Battery predicted temperature [℃]
	Vector of the discretized battery temperature [℃]
$\Delta\vartheta_{ml,c}(\cdot)$	Logarithmic mean temperature difference [℃]
$\vartheta(\cdot)$	Battery temperature [℃]
$\vartheta_{\max}$	Maximum allowed battery temperature [℃]
ϑ_{amb}	Ambient temperature [℃]
$\vartheta_{c,in}$, $\vartheta_{c,out}(\cdot)$	Coolant temperature at battery cooling plate inlet/outlet [℃]
$\vartheta_{cool}(\cdot)$	Coolant temperature [℃]
ϑ_f	Desired battery temperature at the final stage [℃]
ϑ_i	Initial battery temperature [℃]
$\vartheta_{oil}(\cdot)$	Lubricant temperature [℃]
$\boldsymbol{\xi}$	Battery predicted SoC [-]
	Vector of the discretized SoC [-]
$\Delta\xi_t$	Target SoC tolerance [-]
$\Delta\xi_Z$	Net SoC for ZEZ in eDrive [-]
$\xi(\cdot)$	Battery state of charge [-]
ξ_0	SoC at the beginning of the driving cycle [-]
ξ_i	Initial SoC [-]
$\xi_{\min,el}$, $\xi_{\max,el}$	Minimum/maximum SoC in CS mode for the RBS [-]
$\xi_{\min}$, $\xi_{\max}$	Minimum/maximum SoC in CS mode for the modified RBS [-]
	Minimum/maximum allowed SoC [-]
ξ_f	Final SoC [-]
	Desired SoC at the final stage [-]
$\xi_{i,Z}$, $\xi_{f,Z}$	SoC at ZEZ entrance/exit [-]
$\xi_{r,f}$	Final value of the reference SoC (at ZEZ entrance) [-]
$\xi_r(\cdot)$	Reference SoC [-]

ξ_s	Safety SoC margin for target SoC evaluation [-]
ξ_t	Target SoC at ZEZ entrance [-]
ρ_c	Battery coolant density [kg/m^3]
ρ_f	Fuel density [kg/l]
$\tau(\cdot)$	Time constant of the vehicle acceleration transient [s]
$\tau_1(\cdot)$	Time constant of the RC circuit [s]
$\tau_t(\cdot)$	Total transmission gear ratio [-]
$\tau_{dif,f}$	P4 transmission ratio [-]
$\omega(\cdot)$	Engine revolution speed [rad/s]

Notation

$a(\cdot)$,$A(\cdot)$	functions
$\mathbf{a}$,$\mathbf{A}$	vector or matrix
$[\mathbf{a}]_i$	element i of the vector $\mathbf{a}$
$[\mathbf{A}]_{i,j}$	element i,j of the matrix $\mathbf{A}$

Chapter 1

Introduction

In this chapter, an overview of the current automotive background is given in order to practically comprehend the reasons and motivations lying behind the research project. In particular, the electric hybridization of the vehicles is presented as a valid solution to address the air pollution crisis concerning the transportation sector. Then, a brief introduction to the concept of Smart Mobility is offered for a better comprehension of why it is important focusing efforts on urban and sustainable mobility.

1.1 Motivation

In the last century the spreading of industrialization has led to an incessantly growing emission of carbon dioxide (CO_2) and other greenhouse gas (GHG) which heavily impacts one of the most demanding challenges of present times, global warming. This issue is even related to automotive sector, in which individual mobility has been increasing over the past decades.

In fact, the amount of CO_2 emitted per capita is now more than 4 tons per year and 21% comes from the transportation sector [1], which led to stricter regulations in terms of emitted CO_2 mass per driven kilometer. As an example, the EU has set the limit of 95 g/km of CO_2 for 2021 and 80 g/km for 2025 [2], as shown in Fig. 1.1.

This issue, in conjunction with the large and growing proved discrepancies

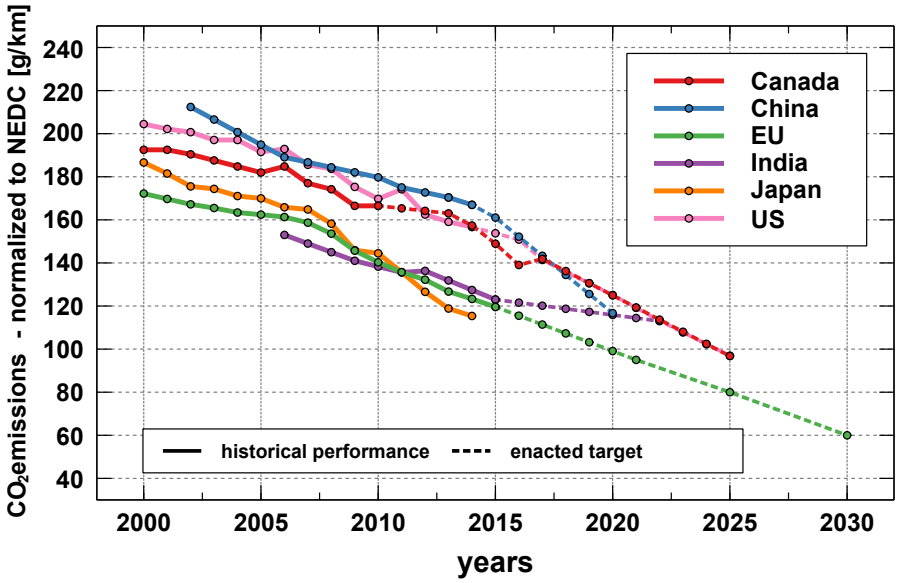

Figure 1.1: Historical fleet CO_2 emissions and current standards for passenger cars [3].

between laboratory (new European driving cycle, NEDC) and on-road emissions, especially for nitrogen oxide (NO_x) emissions from diesel cars, has led to the development of a real-driving emissions (RDE) test procedure by the European Commission. Such a kind of test does not replace the worldwide harmonized light vehicles test procedure (WLTP), but complements it. In the RDE cycle, a car is driven on public roads and over a wide range of different conditions which are designed to be representative of driving conditions normally encountered on European roads [4]. On-board emissions measuring is performed by means of portable emission measuring systems (PEMS) that provide a complete real-time monitoring of the key pollutants emitted by the vehicle.

Moreover, in addition to European legislations, a possible interesting technical solution in order to overtake the global CO_2 emissions challenge can be represented by vehicle powertrain hybridization. In hybrid vehicles, two or more power sources are employed in order to satisfy the driver torque demand. As a consequence, additional degrees of freedom concerning on-board energy management are introduced, which implies the development of more complex control strategies. Despite this disadvantage, several ways now can be pursued in order

to optimize energy use, with particular attention to fuel consumption minimization. Moreover, the adoption of an hybrid architecture allows energy recuperation, which can be achieved by regenerative braking, for example.

Even though several auxiliary energy sources have been taken into account for hybridization, the most widely-spread hybrid vehicles are hybrid electric vehicles (HEV), which use a high-voltage battery as an additional energy storage system. If the electric energy used for propulsion can be derived from renewable energy sources, this vehicle technology is a promising way to reduce global warming. As a consequence, the penetration of HEVs in the automotive market is supposed to increase in the next decades [5], with a 48% of the total volume of passenger cars represented by hybrid vehicles in 2030 [6]. Therefore, this will lead to an increasing in battery capacity and then in the all-electric range of the vehicles[7]. In light of this consideration, HEVs could represent a valid solution for addressing not only the CO_2, but even the pollutant emissions. This possibility has been addressed and further investigated during this research activity by focusing on the urban air pollution crisis, as further described in Section 1.4. In particular, predictive energy management strategies for HEVs have been developed on the basis of navigation data retrieved via in-vehicle connectivity in order to allow and ensure all-electric driving mode in urban areas. With this aim, an advanced connected Hardware-in-the-Loop system has been set up to effectively test the control strategies in a simulation environment with real-time, up-to-date route information.

1.2 Hybrid electric vehicles

A vehicle can be considered *hybrid* if more than one energy source is available on-board, in addition to the fuel which represents the chemical energy source (conventional vehicle). Hybrid electric vehicles are hereby introduced to give a comprehensive overview of this technology to properly understand the concepts described in this work.

1.2.1 Electric hybridization

Nowadays, hybrid electric vehicles are a widely discussed and well-known topic in literature, and numerous studies analyzed this technology in terms of powertrain configuration, control strategies and achievable benefits [8–11].

They comprehend also an electric rechargeable energy storage system (RESS) which is usually represented by a battery. The voltage and the capacity of this component are chosen on the base of the desired power output, defining the degree of electrification of the vehicle. One or more electric motors (EM) are installed, as well, not only for traction purpose, but even for transforming vehicle kinetic in electric energy for battery recharging during deceleration phases (braking). Therefore, the energy stored on board is chemical, flowing from the fuel tank to the internal combustion engine, and electrochemical, flowing from the battery to the electric machines and viceversa.

The major advantage in developing HEVs consists in combining the characteristics of pure-electric and conventional ICE-based vehicles, allowing to reduce the global energy consumption of the vehicle. The main benefits related to HEVs are:

- regenerative braking
  the possibility to recover energy during braking phases instead of using mechanical brakes to dissipate it as heat. Especially in urban cycles, where accelerations and decelerations are more frequent, this opportunity allows to considerably improve the global energy efficiency of the vehicle;

- engine operating point can be optimized
  for a given speed, the operating point of the engine could be shifted to a higher efficiency area by increasing the requested torque, performing the so-called load point shift. This energy surplus can be used by the electric motor to recharge the battery. This functionality can be achieved with an energy management strategy of the power required to the engine;

- downsizing
  to achieve better performance, the engine size could be reduced since electric machines can provide part of the torque requested for traction;

- zero emission policy can be achieved
  as explained in the next sections, in certain areas the use of the engine could be prohibited to maintain air pollution levels below a certain threshold. This task can be achieved by a HEV by addressing the full amount of torque request to the electric motors.

1.2.2 Topologies and classifications

Concerning HEVs, several categories based on powertrain layout and thus energy flow can be defined, as shown in Fig. 1.2, which are

- *series* topology
  it is similar to a pure electric drivetrain with the addition of the engine as an auxiliary power unit. Thus, the latter is not directly connected to the wheels and no mechanical power summation occurs;

- *parallel* topology
  both the engine and the electric motor(s) can directly propel the vehicle, and so a mechanical power summation is possible;

- *power split* topology
  both series and parallel working modes are applied simultaneously. This layout allows higher degrees of freedom than the parallel one, and a higher efficiency than the series one;

- *serial-parallel* topology
  can act either as a series or as a parallel layout depending on the status of one or more clutches, hence it is more flexible than the power-split.

With regard to HEVs parallel topology, several architectures based on electric machines position within the driveline are possible. As shown in Fig. 1.3, they are as follows

- P0
  the motor is coupled to the engine by mean of a belt. In this case, the electric machine is called Belt-driven Starter Generator (BSG);

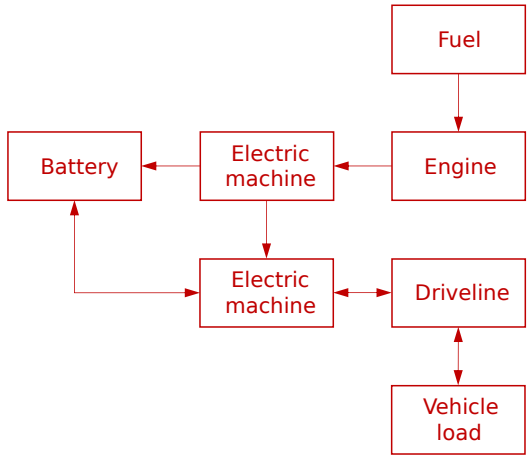

(a) Series.

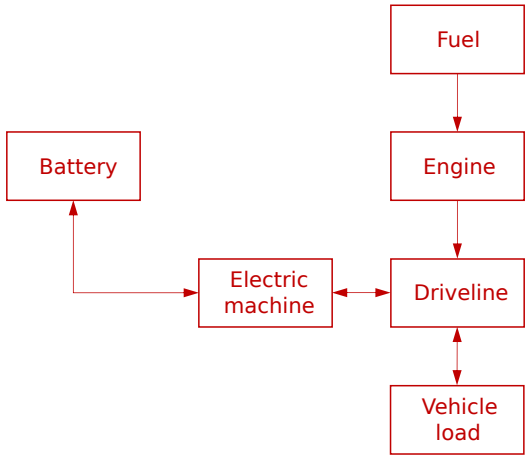

(b) Parallel.

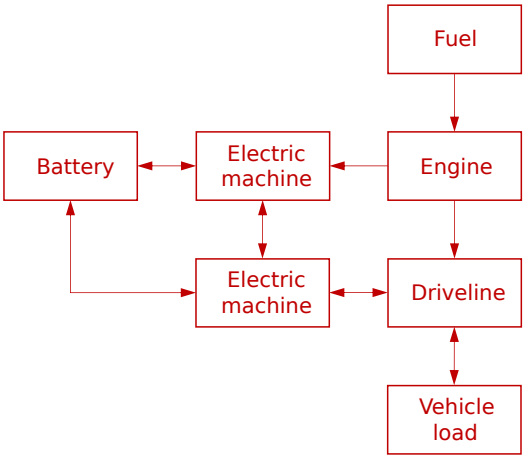

(c) Power split.

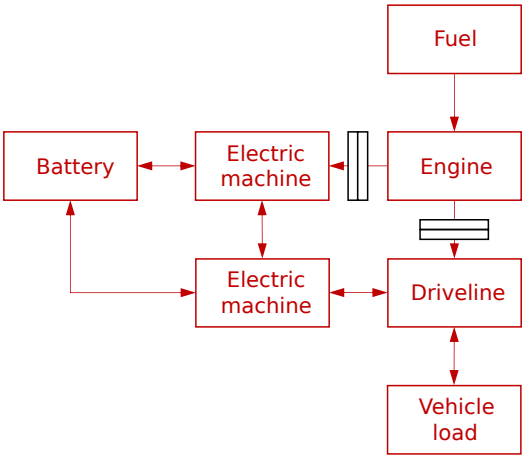

(d) Serial-parallel.

Figure 1.2: HEVs topologies.

- P1
  the motor/generator is directly mounted on the crankshaft upstream of the clutch. Here, the motor is an Integrated Starter Generator (ISG)
- P2
  the motor is still installed before the gearbox, but it is decoupled from the engine by a clutch and pure electric driving mode is available;
- P3
  the motor is mounted on the secondary shaft of the gearbox;
- P4
  the motor is directly mounted on the front or rear axle.

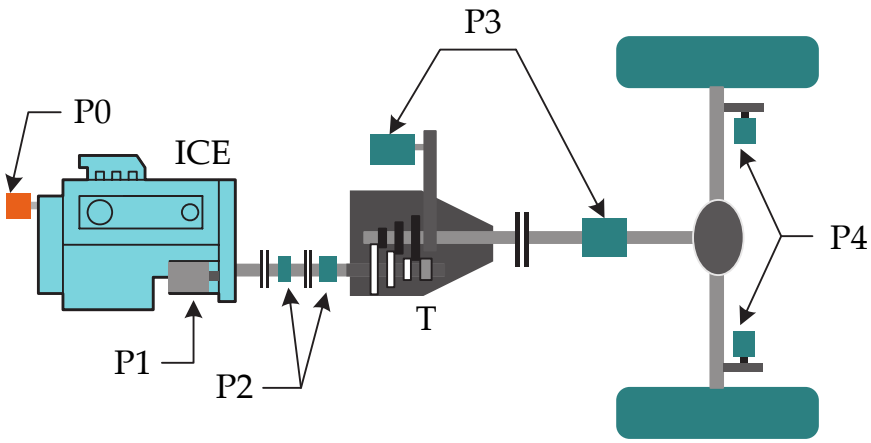

Figure 1.3: Parallel hybrid architectures depending on electric motor(s) position [8].

An additional classification of HEVs can be made depending on their *hybridization degree* (HD), which can be defined as:

$$HD = \frac{P_{S,\max}}{P_{S,\max} + P_{ICE,\max}} \tag{1.1}$$

where $P_{S,\max}$, $P_{ICE,\max}$ are, respectively, the maximum power deliverable by the secondary energy source and the internal combustion engine.

Such a classification, with ascending electrification degree, is presented as follows:

- conventional vehicle (no electrification)
  the chemical energy of the fuel is the only on-board energy source. The driver torque request is fully provided by an internal combustion engine;

- micro HEV
  the installed battery can not be used for traction. The degree of electrification is so minimum that a micro HEV can be considered as a conventional vehicle with only the Start-Stop function available;

- mild HEV
  the higher capacity of the battery allows not only the regenerative braking, but also motor assist, thus improving the driveability of the vehicle (lower torque oscillations), especially at low speed (turbo-lag reduction). Although power boosting is available, all-electric driving mode can not be applied;

- full HEV
  the capacity of the battery is high enough to perform pure electric driving and thus to completely fulfill the electric traction;

- plug-in HEV (PHEV)
  it presents an off-vehicle charging (OVC) function which is justified by the higher capacity of the high-voltage battery. The reason is that this kind of vehicles has been conceived to operate in all-electric driving mode so as to cover the average daily traveled distance in a urban cycle. Thus, the standard operating mode of a PHEV is represented by an initial charge depleting (CD) phase, during which the usage of the electric energy is encouraged as much as possible, followed by a charge sustaining (CS) phase, aimed at maintaining the state of charge (SoC) of the battery almost constant and low, within a certain narrow range.

A schematic representation of the hybridization degree and the CO_2 reduction capability for HEVs is depicted in Fig. 1.4.

Since two batteries are implemented on board of HEVs, the standard low-voltage (LV) and the high-voltage (HV) ones, for a matter of simplicity hereafter in this document the HV battery will be referred to as BATTERY.

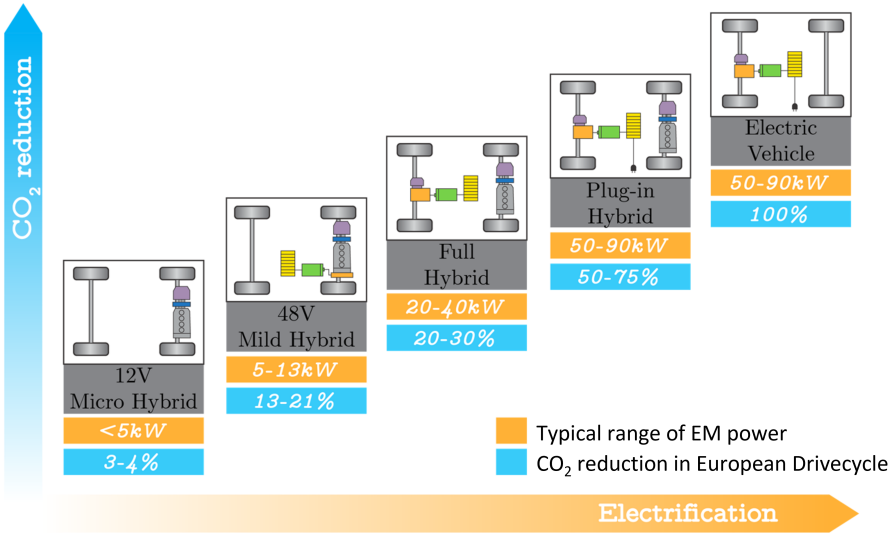

Figure 1.4: Hybridization degree (HD) and CO_2 reduction capability for HEVs [12].

1.3 Connected Autonomous Vehicles

A possible definition for autonomous or self-driving vehicles is given by the U.S. Department of Transportation's National Highway Traffic Safety Administration (NHTSA), which consider such vehicles as "those in which operation of the vehicle occurs without direct driver input to control the steering, acceleration, and braking and are designed so that the driver is not expected to constantly monitor the roadway while operating in self-driving mode" [13, 14].

Connected Autonomous Vehicles (CAVs) have gained increasing attention in the last decades due to several advancements and features aimed to increase driver comfort and safety, such as adaptive cruise control and collision avoidance systems. Therefore, together with hybrid electric vehicles, this kind of technology is strongly penetrating in the automotive industry. If these technologies are combined together, the term CAHEV is often adopted to denote hybrid electric vehicles equipped with connectivity-enabling technologies. The latter enable the vehicle to exchange data with the surrounding environment, as explained in the next sections. This can be considered a turning point for a practical on-board implementation of predictive functions, since they are based on navigation data that can actually be received by the vehicle.

1.3.1 Vehicle-to-Everything technologies

Advancements in wireless communication technologies, sensor fusion, imaging technologies, Big Data, and analytics have created opportunities for automotive manufacturers to discover a wide range of solutions for multiple applications. Miniaturization of electronic components, advancements in navigation, and adoption of smart devices is expected to fuel advancements in the Vehicle-to-Everything (V2X) communications industry [15–19]. It is expected to show high growth potential for the development of future connected cars that will be able to interact with the surrounding environment to improve driver safety. One of the practical applications of such technologies imply reducing traffic congestions, which lead to an increase of fuel consumption and to a worsening of the urban air pollution. As an additional drawback, the economic impact of traffic jam-related problems is not negligible [20], as well.

According to 3GPP [21], V2X technologies include communication between different entities and the ego-vehicle, both for safety and non-safety application. Navigation data exchange is made via different vehicular communication networks, also called nodes. Depending on the type of the node, the following classification applies:

- Vehicle-to-Vehicle (V2V)
  the moving nodes are represented by the vehicles communicating with each other

- Vehicle-to-Infrastructure (V2I)
  road infrastructures transmit navigation data regarding traffic lights timing, road works, traffic congestions, and so on

- Vehicle-to-Network (V2N)
  the ego-vehicle communicates with IT networks and/or data centers

- Vehicle-to-Pedestrian (V2P)
  vehicles connect with pedestrians or bikers on the road to prevent accidents

1.3.2 Advanced Driver Assistance Systems

Since navigation systems are increasingly entering the automotive sector, the available map data may not only be used for routing purposes but also to enable advanced in-vehicle applications [22]. The area of potential features reaches from headlight control up to active safety applications. With the ongoing development of navigation based ADAS features the interface to access the so-called ADAS Horizon is of rising importance. At this end, Advanced Driver Assistant Systems Interface Specifications (ADASIS) is an industrial platform where map provider and automotive developers work together to standardize the map data. The method of how a vehicle's control unit could be provided with the navigation data is specified as well in the ADASIS protocols [23, 24].

To enable this kind of technology, on-board vehicle sensors play a vital role on driving automation, providing the spreading concept of data fusion in order to improve navigation data availability as well as reconstruct an electronic horizon of the upcoming events. As shown in Fig. 1.5, these sensors include

- LIDAR (LIght Detection And Ranging)
  surveying method that measures the distance to a target by illuminating that target with a pulsed laser light;
- RADAR (RAdio Detection And Ranging)
  object-detection system that uses radio waves to determine the range, angle, or velocity of road objects;
- camera
  a video sensor used to analyze the environment outside and inside the vehicle.

ADAS systems, supported by on-board sensors, are leading the way to the actual self-driving car revolution. There have been multiple definitions for various levels of automation and for the sake of standardization, to aid clarity and consistency, NHTSA has adopted the *autonomy levels* proposed by the international Society of Automotive Engineers (SAE) in [25]. These levels are based on the concept *who does what, when* and span from no automation (Level 0) to full automation (Level 5). They can be summarized as follows:

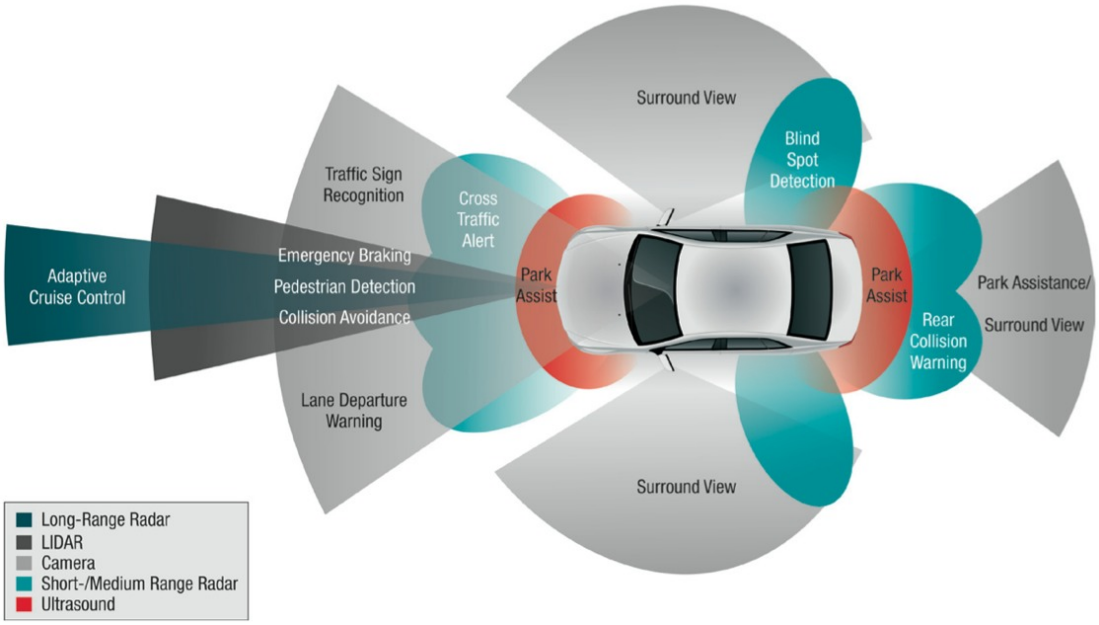

Figure 1.5: On-board vehicle sensors.

- Level 0: No Automation
  the human driver does all the driving;

- Level 1 : Driver Assistance (*hands-on*)
  an ADAS on the vehicle can sometimes assist the human driver with either steering or braking/accelerating, but not both simultaneously;

- Level 2: Partly Automated Driving (*hands-off*)
  an ADAS on the vehicle can itself actually control both steering and braking/accelerating simultaneously under some circumstances. The human driver must continue to pay full attention ("monitor the driving environment") at all times and perform the rest of the driving tasks.

- Level 3: Conditional Automation (*eyes off*)
  an automated driving system (ADS) on the vehicle can itself perform all aspects of the driving task under some circumstances. In those circumstances, the human driver must be ready to take back control at any time when the ADS requests the human driver to do so. In all other circumstances, the human driver performs the driving task.

- Level 4: High Automation (*mind off*)
  An ADS on the vehicle can itself perform all driving tasks and monitor the driving environment – essentially, do all the driving – in certain circumstances. The human need not pay attention in those circumstances.

- Level 5: Full Automation (*brain off*)
  an ADS on the vehicle can do all the driving in all circumstances. The human occupants are just passengers and need never be involved in driving.

1.4 Smart Mobility

Connected and autonomous vehicles, equipped with on-board sensors, ADAS systems and V2X technologies, could represent a first step toward Smart Mobility, which can be considered a new way of conceiving mobility aimed to improve its social, environmental and economical impact [26]. In particular, the goal is to reduce air and acoustic pollution, road congestion and accidents.

This topic has recently gained an increasing attention. The reason is that, starting from the last decades of the twentieth century, the industrialization has seen exponential growth that has led to a massive migration of people from the rural areas to the urban centers. In [27] it is reported that, in 2016, 5 billion people lived in urban areas and this number is projected to increase to 7 billion by 2050 [28]. This led to a worsening of the air pollution crisis in urban areas and urban mobility, in general.

Thus, from one hand, manufacturers are responding with innovative solutions such as more efficient conventional engines and the introduction of hybrid electric vehicles. On the other hand, legislation and regulations are focusing on enhancing sustainable urban mobility, especially in Europe [29]. In particular, the introduction of Low (LEZ), Ultra-Low (ULEZ), Zero (ZEZ) Emission Zones are being adopted to reduce pollutant emission from the transportation sector in urban contexts. As reported in [30], more than 250 European cities have already taken such measures. As an example, a ULEZ is constantly active in London, operating 24 hours a day, 7 days a week, every day of the year [31]. Remarkable benefits in terms of air quality improvement due to emission reduction have been measured:

a reduction of 31% for NO_x and 4% for CO_2 have been estimated with respect to a no ULEZ scenario in the period July-September 2019 [32].

For this reason, this project is focused on energy management strategies of hybrid powertrains which could play an important role for handling such reduced emission zones.

Chapter 2

Literature review

A comprehensive literature review on the topics studied in this research project is here presented.

In particular, different energy management strategies (EMSs) have been analyzed in order to improve the energy efficiency of plug-in hybrid electric vehicles. Since V2X technologies enhanced the possibility of retrieving navigation data and make them available on board, the prediction of future conditions of the powertrain has been investigated with the main objective to provide the supervisory controller detailed information regarding the status of the components. In this way, it is then possible to optimize the power distribution of the hybrid vehicle and, at the same time, to ensure global constraints for different scenarios, such as ensuring all-electric driving in a Zero-Emission Zone.

In order to speed up the testing and the validation of the aforementioned strategies and functions, an advanced simulation environment such as a Hardware-in-the-Loop (HiL) has been developed and set up.

2.1 Energy management strategies for HEVs

In order to control the power distribution, and then the energy flow, among the conventional and the electric powertrain of a HEV, different energy management strategies are available for this purpose, depending on the parameters involved in the control policy, the degree of hybridization and the complexity of the vehicle

topology (parallel, series, or a combination of the previous ones).

They are usually implemented in a supervisory controller, known as hybrid (HCU) or vehicle (VCU) control unit, because the main objective is coordinating all the other on-board controllers, such as the transmission control unit or the battery managements system (BMS), as further explained in Section 3. Thus, from this point of view, the powertrain control can be defined as *hierarchical*.

Energy management strategies are then used to control every component of the powertrain (engine, motors, battery, transmission, etc.) by requiring certain set-points for each of them in order to satisfy the hybrid features of the vehicle. Although EMSs are very different in terms of approach and mathematical formulation, many of these features can be found in all of them as common practices for HEVs.

As outlined in Chapter 1, during traction the driver torque request, $T_q(t)$, is fulfilled by the engine or the electric motors. To this aim, in order to establish the power distributions between those actuators, a torque-split factor, $u_s(t)$, is calculated by the HCU. For a parallel hybrid, which is the one considered in this dissertation, the torque request to the engine and the electric motor(s) are, respectively, $T_{ICE}(t) = (1 - u_s(t))T_q(t)$ and $T_{EM}(t) = u_s(t) \cdot T_q(t)$. During all-electric driving mode ($u_s(t) = 1$), only the electric motors provide the needed power output. In case that vehicle propulsion is addressed only to the conventional powertrain ($u_s(t) = 0$), the engine is managed by the HCU in such a way that a torque surplus could be generated to recharge the battery. This technique, called *load-point shifting*, allows the engine to be operated at higher efficiency points, given the speed of the vehicle and then the engaged gear. On the other hand, during braking, the kinetic energy is converted by means of the electric motors which apply the required torque to decelerate the vehicle ($u_s(t) < 1$). Since these components can be used also as generators, the mechanical input (resistant torque) is converted into an electrical output (current flow), which is used to increase the state of charge of the battery. This feature is also known as *regenerative braking*. This energy saving gives the opportunity to extend the all-electric range of the vehicle, with consequent benefits on fuel saving.

Different classifications of EMSs are available and are hereby reported.

A first distinction can be made whether optimal control theory is adopted to

define the control policy or not. As proposed in [33, 34], EMSs can be classified as:

- *heuristic*
  such strategies are defined on physical considerations or intuitions and are usually developed considering maps or rules to define the operative working conditions of the powertrain. No explicit optimization of the power distribution is performed;

- *sub-optimal*
  the main objective of the control algorithm is achieved by optimizing the energy flow within the powertrain, thus minimizing a certain cost function, which could represent the energy consumption of the vehicle. Since the optimization is performed locally, namely at each calculation step of the HCU, the solution of the minimization process is inherently sub-optimal;

- *optimal*
  a global optimization is performed, meaning that the solution is the one with the best performance in terms of cost function minimization all over the possible actuation set-points. This implies the a-priori knowledge of the driving cycle, with consequent high computational load.

The control strategy can be referred to as

- *causal*
  when no prevision on the route ahead is available and then used.Tthen, the powertrain control is governed by a cause-effect relationship between the actuator set-points and the state variables;

- *non-causal*
  when state variables are predicted on the base of the available information of the driving mission.

Numerous investigations have been conducted on the energy management strategies [35–38]. More extensive reviews on the topic are available in literature, spanning among different characteristics such as numerical comparisons [39, 40], real-time applicability [41] and future trends for EMSs [42, 43].

2.1.1 Heuristic control strategies

As suggested by their name, heuristic energy management control strategies are based on intuitions and physical considerations for calculating the required power distribution among the powertrain.

Although a wide range of possibilities exist in choosing the vehicular parameters and the conditions to be satisfied for this task, several common design guidelines can be found.

Since HEVs have been introduced to reduce the fuel consumption and then the CO_2 production, the first assumption could be represented by using the internal combustion engine as less as possible (for PHEVs), and, in general, in high efficiency working areas (for HEVs), characterized by high load conditions. Another guiding principle suggests to maintain the battery state of charge (SoC) within a certain range (for HEVs), which may correspond to the entire working range of the battery defined by the manufacturer (for PHEVs). As a result of the application of these principles, the operative mode of a HEV, without off-board charging capabilities, is typically represented by a charge-sustaining (CS) mode around a certain target value of SoC. For HEVs, since the battery can be recharged by plugging the vehicle to the grid, the operative mode may result in a combination of charge-depleting (CD) and then charge-sustaining modes. Therefore, the use of the electric energy stored in the RESS is always encouraged, if the respective conditions are satisfied, because the conversion efficiency of the chemical energy of the fuel to the electro-chemical one of the battery is quite low. As a consequence, battery discharge is applied until the minimum SoC allowed for a correct usage of the component is reached. At that point, the SoC level is maintained constant within a certain narrow range.

The aforementioned principles can be applied by means of different approaches: map-based and rule-based approach.

The first ones are defined by multi-dimensional look-up tables usually depending on the driver torque request, the vehicle speed and the battery SoC. In order to limit the complexity of the strategy, no more than three parameters are typically taken into account. In particular, the boundaries between regions can

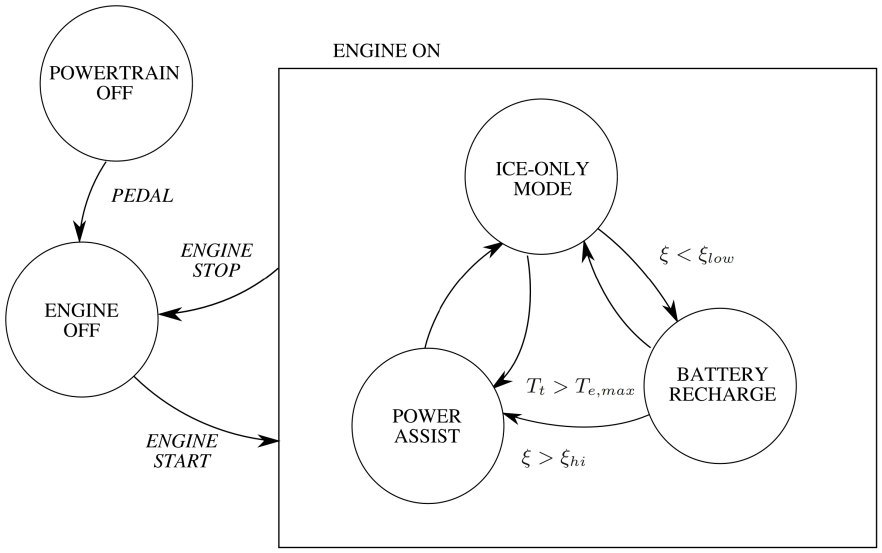

Figure 2.1: Control logic for a heuristic, rule-based energy management strategy [33].

be dynamically managed by means of *fuzzy-logic* rules [44, 45]. Rule-based strategies rely on a set of conditions defined considering vehicular parameters such as the ones above mentioned [46]. Other parameters such as the power limitations of the electric machine during pure electric driving [47] can be considered for this purpose. In this case, fixed thresholds have to be established to fulfill all the boolean conditions, which can be considerably numerous since the limit of a multi-dimensional map is not present. Such rules are generally implemented in the control policy by means of finite state machines, representing the state condition to be fulfilled for the transition to one state to another, as shown in Fig. 2.1. In this case, if the SoC level is below the lower threshold ξ_{lo}, the engine provides an additional torque to recharge the battery ($u_s < 0$). If the battery is sufficiently charged ($\xi > \xi_{hi}$), the engine is used only for vehicle propulsion ($u_s = 0$). If the engine is not able to address the total power output, electric motors are used for power assist ($0 < u_s < 1$). On the other hand, if the torque requested by the driver can be totally delivered by the motors and, at the same time, the energy stored in the battery is high enough and the vehicle speed is low, all-electric driving is allowed ($u_s = 1$), and the engine is switched off.

Since no optimization is performed, this kind of strategies are not affected by

high computational load. Moreover, the heuristic approach does not require to develop any optimization algorithm, which is usually more complex due to its mathematical formulation. This implies a lower computational burden required instant by instant to the supervisory controller. For those reasons, heuristic strategies, especially the rule-based ones, are widely used in the industry of the automotive fields to control the energy management of the hybrid powertrain. Nevertheless, a intensive calibrations campaign is needed to properly tune the look-up tables or the threshold values of such strategies. In order to speed up this process and increase the energy efficiency of the power distribution, optimal energy management strategies can be used as benchmarks for this purpose [48, 49].

2.1.2 The optimal energy management problem for HEVs

To properly understand the optimization-based control strategies, the analytical formulation of the energy management problem for HEVs is provided in this section.

In general, given a certain topology of hybrid vehicles, the aim of an optimal energy management strategy is to minimize the global energy consumption and then the CO_2 production. Thus, a mathematical function describing the impact (energy cost) of such parameters depending on actuator set-points and state variables shall be defined. It usually known as *cost function*, or *performance index*. In this case, the energy management strategies aim to provide a solution to this problem, which is represented by the control law that minimizes the cost function over a certain time horizon.

Thus, as proposed in [40, 50], a formulation of the cost function J for HEVs involving the fuel consumption can be expressed as:

$$J = \int_{t_0}^{t_f} \dot{m}_f \left(\mathbf{x}(t), \mathbf{u}(t), t\right) dt \tag{2.1}$$

where $\dot{m}_f$ is the instantaneous fuel mass flow rate, $\mathbf{x}(t)$ and $\mathbf{u}(t)$ are the vectors of the variables states of the system and the control inputs, and $[t_0, t_f]$ is the time domain in which the optimal control problem is defined. Its solution is then represented by the control policy $\mathbf{u}^*(t)$ that minimizes the performance index over

the given time interval and subjected to global boundary conditions, related to the state of the system:

$$\psi\left(x(t_f),t_f\right) = 0 \tag{2.2}$$

and local constraints, representing the admissible actuator set-points and the physical limitations of the system in terms of available torque and power, admissible speed and SoC:

$$\begin{cases} G(\mathbf{x}(t),t) \leq 0 \\ \mathbf{u}(t) \in U(t) \end{cases} \tag{2.3}$$

2.1.3 Sub-optimal control strategies

Sub-optimal control policies solve the optimal energy management problem defined in Eq. (2.1) by locally minimizing the cost function, which means considering a time horizon compatible to the calculation step of the supervisory controller.

The main applications of this approach are represented by

- Model Predictive Control (MPC) [51]
- Equivalent Consumption Minimization Strategy (ECMS)

The local optimization is a reliable trade-off between the real-time capability of heuristic EMSs and the optimal solution guaranteed by non-causal controllers. In particular, the ECMS has been demonstrated in [52] to be directly deducible from the optimal Pontryagin's Minimum Principle, if properly formulated. Sub-optimal strategies are inherently implementable on-line and do not require an intensive calibration effort.

2.1.3.1 Equivalent Consumption Minimization Strategy

The Equivalent Consumption Minimization Strategy was initially formulated by Gino Paganelli in 1999 [53] and then applied as a practical solution for the energy management problem in HEVs [54, 55].

It is based on the empirical consideration that a virtual fuel consumption can be attributed to the usage of the electric energy of the battery. Under this

assumption, the cost function to be minimized can be represented by an equivalent fuel consumption that can be formulated as follows:

$$\dot{m}_{f,eq} = \dot{m}_f + \dot{m}_{f,b} \tag{2.4}$$

where

$$\dot{m}_{f,b} = s(t)\frac{P_b(t)}{Q_{lhv}} \tag{2.5}$$

In other words, the electrical energy used by the battery and the chemical energy of the fuel are correlated by an *equivalence factor* $s(t)$.

Other supervisory controllers perform a local minimization of an equivalent fuel consumption that considers both the real fuel consumption and the electrical power requested to the battery. Such controllers are usually considered as sub-optimal [48, 52, 56–58]. Another option is represented by optimization-based controllers, which are based on optimal control algorithms and can determine the global optimal solution for the powertrain control [34, 59, 60]. Such methodology guarantees the best energy management, but still presents issues related to online implementation, due to the high computational effort required, and the need to exactly predict future operating conditions. These energy management strategies have been deeply studied and several of them have been already deployed on board of vehicles on the market. To keep the pace of the regulations, innovative technologies are being implemented both on the vehicle and the infrastructure, such as wireless communication, and cloud computing. These technologies are divided into vehicle-to-vehicle (V2V), vehicle-to-infrastructure (V2I), and vehicle-to-network (V2N) communication. In fact, they can provide the aforementioned strategies with a forecast of the driving path ahead, resulting in more efficient energy management.

Several studies highlighted the benefits of future driving information for energy management strategies. An improved A-ECMS based on long-term target driving cycle recognition and short-term vehicle speed prediction is presented in [61]. It can optimize the equivalence factor based on mileage, SoC, long-term driving cycle and real-time vehicle speed, resulting in a reduction of fuel consumption of 8.7%. Similarly, algorithms can determine the optimal SoC trajectory according

to the traffic information, while the Equivalence factor is regulated dynamically, thus enabling effective tracking of the reference SoC trajectory [62, 63]. In [64] is presented a different A-ECMS that uses a historical driving profile for EF estimation, the proposed strategy is able to foresee the change of the driving behaviors and adjust the EF more reasonably. Furthermore, in [65] a LEZ-anticipating control strategy for a PHEV bus with P2-type parallel powertrain configuration. The control strategy is based on a combined RB/ECMS, and it is superimposed by generating an optimal SoC reference trajectory aimed at enabling pure electric driving through forthcoming LEZs and minimizing the overall fuel consumption. The optimal SoC reference trajectory is generated by minimizing its length over traveled distance.

2.1.4 Optimal control strategies

The main applications of this approach are represented by

- Dynamic Programming (DP)
- Pontryagin's Minimum Principle (PMP)
- Convex Optimization (CVX)

2.1.4.1 Dynamic Programming

Dynamic Programming is an optimal, non-casual algorithm that relies on a numerical approach based on the *Principle of Optimality* proposed by the mathematician Richard E. Bellman in 1952 [66–68]. It is stated as follows:

An optimal policy has the property that whatever the initial state and initial decision are, the remaining decisions must constitute an optimal policy with regard to the state resulting from the first decision.

Thus, considering the powertrain as a generic dynamic system evolving over time, and assuming that all the intermediate states of this evolution are known (non-causality), the aim is to find the control policy that minimizes a given cost

function, which can be formulated as:

$$J = L_N(x_N) + \sum_{k=0}^{N-1} L_k(x_k, u_k, w_k) \tag{2.6}$$

where:

k : discrete time index, or stage;
N : total number of stages, which defines the time horizon length;
$x_k \in S_k$: system state vector at stage k;
$u_k \in U_k(x_k)$: control inputs vector at stage k;
w_k : vector representing the disturbances acting on the system at stage k.

The stage cost L_k is the cost associated to each state for the applied actuator set-point, while the terminal cost L_N ensures the desired state of the system at the final stage. The objective of the algorithm is to determine, at each stage, the optimal control input u_k^* between the all admissible ones (multi-stage decision) which minimizes the cost function from that stage to the final one, also known as *cost-to-go*. The Bellman's principle ensures that the policy $\{u_k^*, \ldots, u_{N-2}^*, u_{N-1}^*\}$ related to the last part of the problem represents the optimal control policy. Therefore, the optimization is performed in a backward-facing approach, starting from the final stage N to the initial one, and establishing the optimal control input at each stage. In this way, it can be noticed that an a-priori knowledge, or at least a prediction, of the state vector x_k is needed. Moreover, the dynamic, multi-stage decision process strongly increases the computational load required to numerically solve the problem. For this reason, optimization-based algorithms are theoretically non online implementable. Nevertheless, since the optimality of the solution provided, they are used as benchmarks for the calibrations of other energy management strategies [48].

Only after several decades from its formulation Dynamic Programming has been applied to the energy management problem of HEVs [69, 70], and it is nowadays a well-established topic in the automotive control field [71–74]. Considerable effort has been put to reduce the computational load of the algorithm. In [75] a novel approach for state variables definition is proposed. In particular, the SoC has

been substituted by the cumulative battery power whose shorter discretization contributes to reduce the size of the state variables vector and, then, the computational burden. However, although half of the running time can be saved, the proposed algorithm is still applied as a benchmark tool.

Since the developed DP algorithm take into account the battery thermal behavior for defining the state variable, as further described in Section 2.3, the following state-of-the-art analysis is here given. First of all, it must be said that, from a thermal management point of view, the electrical battery pack in HEVs must deal with important thermal issues, which can seriously compromise reliability, safety and aging of the involved components. Nowadays, most of the in-vehicle strategies rely on rule-based controllers, as well, which require large calibration campaigns ad are usually heavily restrictive to avoid power de-rating and battery premature aging. Consequently, an advanced battery thermal management system (BTMS) is needed [76]. A predictive thermal strategy has been proposed and analyzed in [77]. The study is focused on the possibility to attain a certain cooling power reduction by means of plugged-in battery thermal pre-conditioning. During grid charging active pre-conditioning is realized by cooling down the battery and thus no cooling power has to be supplied during the driving cycle because the battery temperature does not reach the upper threshold set for actuators activation.

In [78] a thermal management strategy for CAEHVs using DP is proposed. In particular, air and liquid mass flow rates are adopted as control inputs to control the thermal behavior of the battery. Moreover, to enable the real-time implementation of the algorithm, the grid dimension due to the number of state variables and control inputs has been reduced by means of an iterative approach, called Iterative Dynamic Programming (IDP). It is a numerical method which consists in applying several times the base DP algorithm and regenerating a coarser grid at every iteration. Thus, a time horizon of 60 seconds has been achieved and tested at HiL level, where the BTM strategy has been implemented in a rapid control prototyping hardware. A multi-objective DP focused on battery life optimization has been proposed in [79, 80]. For this reason, a battery severity factor has been evaluated by means of a capacity degradation model in order to take into account battery aging in the cost function of the DP algorithm.

Several ways to employ route information for energy-efficiency targets are

under research. One of these is represented by the use of a Model-Predictive Control (MPC) strategy in which a model of the investigated system is developed in order to fully describe the associated thermal dynamics. Such an accurate model is needed to calculate the predicted control as a function of several input signals [81]. Thus, the control law can be obtained by optimizing an objective function. In [82] a control-oriented non-linear model is first developed for the system and a Non-linear Model Predictive Control (NMPC) scheme is formulated to make it possible to use the knowledge of the predicted future drive cycle and the battery thermal system model for an efficient battery thermal management. An interesting study has been conducted in [83] with the aim of developing an MPC design as an alternative solution for thermal management cabin heating for HEVs. Here, the challenging possibility of the cabin thermal management to influence the vehicle energy management is shown. In particular, the torque split factor is evaluated so as to distribute the workload between the heater core and the PTC heater in an optimal way, i.e. minimizing fuel consumption.

2.2 Testing environment

The development and validation of predictive control strategies collide with the shortening of the vehicle time-to-market [84]. A recent survey shows that 68% of the automotive companies have now a product development and launch cycle under two years [85]. The old consolidated methodologies (reliable road tests above all) do not fit anymore because the safety validation of a current driver assistance system alone requires up to 2 million test kilometers [86]. Besides, most of the functions under test regard dangerous and highly variable conditions that are difficult and expensive to replicate with conventional tests. Thus, the tendency is to move the driven kilometers from the road to advanced simulation environments in a process called Road-to-Rig-to-Desktop [87]. Among all the advantages of a virtual test, there is the possibility to control every variable, granting repeatable tests especially for conditions hard to recreate in the reality. In particular, the validation and verification of connectivity-related functionalities are becoming more demanding as they must be tested in a huge number of scenarios, regarding dangerous (e.g., emergency brake) and highly unpredictable situations

(e.g., collaborative adaptive cruise control and connectivity-related functions) to be declared reliable. The challenge is therefore to develop a testing and validation framework that can replicate the effectiveness of road conditions and traffic scenarios.

To deal with this problem, advanced HiL testing environments have been developed among the last decades.

Following this tendency, specific commercial software were developed and made available on the market, such as PreScan and ITS Modeller presented in [88], whose aim is to provide the automotive industry with a tool for developing connected vehicle systems from concept to production. A simulation framework, consisting of driving, traffic, and network-simulators, has been presented in [89]. Its main objective is testing and evaluation of Co-operative Intelligent Transport Systems (C-ITS) applications.

Once the simulation of vehicles and networks in a virtual environment is established, in [90] it has been improved with optimal energy management, which is tested using the short horizon information coming from the leading vehicle in the collaborative environment.

In [91], from Bosch, this simulation framework has been adopted to evaluate the advantages of a route preview (long horizon) in order to determine in which part of the trip it would be more convenient to regenerate the diesel particulate filter. In the same way, in [92], from Ford, that example is applied to a real prototype controller mounted on a prototype vehicle. On the other hand, the short horizon communication is not implemented in this contribution. A similar on-road test is proposed in [93], where a short-range wireless communication is tested with an intersection collision warning function and then verified on a real vehicle. On the other hand, the long horizon is left apart as well as the vehicle dynamics. An evolution of that work is presented in [94], where several OBU/RSU hardware have been connected to a microscopic traffic simulator (Simulator of Urban Mobility, SUMO) to integrate real vehicular communication devices. Anyway, it focuses on the C-ITS simulation for automated vehicles while it does not simulate the vehicles' dynamics nor the long horizon connectivity. Simulation frameworks like these are used also for Automated Vehicles functions development, as shown in [95], where a Hardware-in-the-Loop simulator for developing automated driving

algorithms has been set up. In this case, the real-time PC carries out the simulations of other moving vehicles while also generating traffic scenarios while the prototype control unit runs the algorithm. However, the long horizon is not simulated even in this work. A step further was made in [96], where an Engine-in-the-Loop system integrated with a real-time traffic simulator (named VISSIM) has been developed to evaluate the performance of emerging connected vehicle applications. This allows a systematic evaluation of connected vehicle mobility and energy savings, as emissions and fuel consumption can be measured precisely. Then, a real vehicle equipped with an OBU is driving along with other connected vehicles. That vehicle data is transmitted to the HiL, which reacts consequently. There is nothing concerning the long horizon, and, besides, it has been assumed that perfect communication is available between vehicles.

Finally, the development of a sustainable framework for testing control strategies for CAVs is proposed in [97]. In particular, in the given HiL the vehicle dynamics are up to ETAS DESK-LabCar, controlled by on-board control units, i.e. MicroAutoBox and Matrix embedded PC-Adlink. The latter oversees the communication with the OBU and the cloud, respectively through Ethernet and LTE. The environment and the perceptive sensors are simulated with PreScan, while the micro-traffic with PTV VISSIM. Although such an advanced simulation framework is very interesting, it has been presented with a short driving routine.

2.3 Innovative contributions of the research project

The present dissertation is focused on three different typologies of energy managements strategies. The first is represented by rule-based strategies, which are the default strategies, developed by the industrial partner and implemented in the prototype vehicle. Furthermore, an Adaptive-ECMS for PHEV based on navigation data has been developed in order to handle zero-emission zones [98]. Finally, an algorithm based on Discrete Dynamic Programming for combined energy and battery thermal optimization is proposed [99]. With regards to the simulation environments, V2X technologies have been implemented in a Hardware-in-the-Loop to enable vehicular connectivity for navigation data retrieving [100].

An algorithm based on the equivalent consumption minimization strategy has

been investigated. In particular, an A-ECMS combined with predictive navigation data and topological information about upcoming ZEZ is proposed. The development, testing and validation of this strategy follows the V-Model methodology [101]. First, a conventional ECMS has been presented in [102, 103] where the benefits of the ECMS for a PHEV are highlighted by using a Model-in-the-Loop (MiL) simulation environment. In this paper, the speed profile and the road slope are used as input for an on-board predictive control strategy developed for a PHEV. After that, a dedicated algorithm predicts the amount of necessary energy to complete the city event in full-electric mode, giving an SoC target value. To this end, an A-ECMS has been modified to use navigation data for approaching the ZEZ with the target SoC. The strategy has been implemented and tested with a Software-in-the-Loop (SiL) simulation environment. In particular, it is implemented in the same software architecture that it is used for the final application on the prototype vehicle. The paper finally quantifies the benefits of such an approach in terms of CO_2 emissions by comparing it with a heuristic, rule-based one, adapted to receive the same input data and calculate the SoC target. In parallel, the HiL simulation environment setup has been carried out and presented in [100]. So, it will be possible to test the strategy with navigation data coming from the server, through the V2N communication, as if the vehicle were on the real road.

Concerning the dynamic programming algorithm, it is aimed to simultaneously optimize both the energy and battery thermal management controls. With this solution, the battery temperature is taken into account when optimizing the energy management and, at the same time, controlling the thermal management in a more energy-efficient way, while still respecting the battery-related constraints. In [104] a combined optimization of the energy and thermal management is proposed, but in this case, the thermal behavior considered is the engine one, while this study considers the high-voltage battery thermal management. Instead, in [105], the authors considered the thermal state of the battery in the energy management as a soft-constraint, following a PMP approach. The novelty of the proposed approach relies on the derivation of the energy and battery thermal management strategies within the same optimization loop, by considering the interaction of the propulsion and the battery cooling system, allowing a more effective usage of the battery. The obtained results are compared with the standard

controllers implemented in the model-in-the-loop environment of the vehicle, in order to assess the value of the proposed solution.

Regarding the simulation environment in which the previous strategies have been developed and tested, this work counts on a highly detailed vehicle model (validated over experimental data) supervised by the production level HCU software unlike those presented in [88, 93, 94], with complete access to the components and controllers models. The HCU is then equipped with the typical V2X communication technologies, both for the long horizon such as in [91, 92], and the short horizon such as in [93–96]. Moreover, the connection to the private server enables the testing of cloud computing and predictive maintenance functions, as in [96]. So, the proposed HiL-based validation platform results in a more modular and universal tool for testing and validating predictive eHorizon functions. On one hand, it provides higher flexibility due to the possibility to test a different kind of predictive functions (long and short horizon, predictive maintenance) and the capability of acting on each component and controller model. On the other hand, it grants higher reliability, as both the hardware and the software are the same as those implemented on the vehicle, allowing seamless functions implementation on-board once validated at the HiL. Thus, it will shorten the validation process and further reduce the gap between laboratory and on-vehicle tests.

2.4 Organization of the dissertation

Following this introduction on the research topics and the presented novel contributions, the organization of the dissertation is as follows:

- in Chapter 3 the powertrain modeling of the vehicle under study is analyzed, with particular attention the models of the high-voltage battery, the Battery Management System (BMS) and the supervisory controller;

- in Chapter 4 the simulation environments are presented. From one hand, the Software in-the-Loop (SiL) system used for the development of the control strategies is presented, including the powertrain validation. On the other hand, the connected HiL set up for strategies testing and validation is shown;

- Chapter 5 is focused on the control strategies for the energy management of the vehicle. At first, the standard RBS strategies are introduced. Then, both the control algorithms and the predictive functions are presented. Their mathematical formulations are provided, as well;
- in Chapter 6 the results obtained by comparing the reference and the tested strategies are presented and discussed. In particular, fuel consumption and CO_2 production are estimated;
- in Chapter 7 the achievements of this work are analyzed, together with the possible future works to overcome the limits of the research project.

Chapter 3

Control-oriented powertrain modeling

The modeling of the considered hybrid electric powertrain is here presented. The main objective of this model is to properly represent the energy flows within the powertrain in order to evaluate the fuel and energy consumption. At this aim, since several modeling approaches can be adopted, a brief overview is given to clarify each aspect of them. They will be applied in different contexts, as further explained in the next chapters. Moreover, the components of the powertrain are individually introduced and analytically described, with particular attention to the high-voltage battery, which plays a crucial role in HEVs.

3.1 Vehicle under test

For the sake of comprehension, before analyzing the powertrain modeling approach, the examined vehicle is here described. It is represented by a prototype plug-in HEV with a parallel P1-P4 topology. Its powertrain is depicted in Fig. 3.1, while the main specifications are listed in Tab. 3.1. A detailed description can be found in [106].

As previously introduced, according to Fig. 1.2b, the vehicle propulsion can be provided by two different energy paths: the pure electrical one and the hybrid one. The former includes two identical electric machines (EMs) mounted on the front

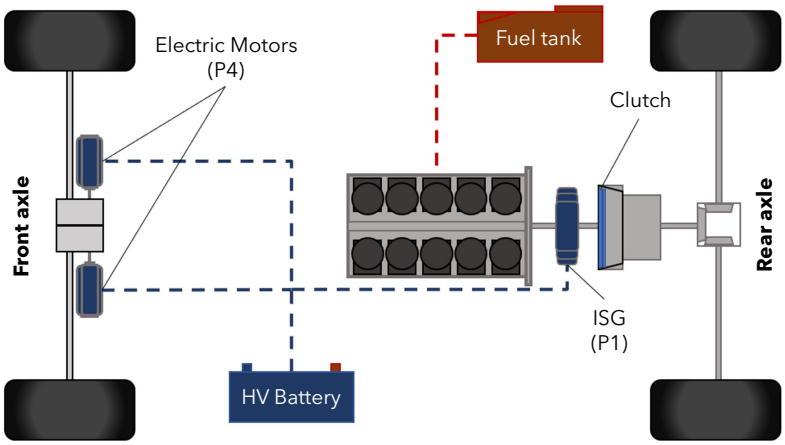

Figure 3.1: Powertrain architecture for the considered prototype vehicle [100].

Table 3.1: Vehicle powertrain data [100].

Parameter(s)	**Value(s)**	
Battery nominal capacity (1C@25°C)	19.4	Ah
Battery nominal/maximum voltage	384/391	V
Electric machines maximum torque (cont./peak)	145/350	Nm
Electric machines maximum power (cont./peak)	64/140	kW
Engine maximum torque	533	Nm
Engine maximum power	449	kW
Overall maximum power (cont./peak)	577/729	kW

axle, which can serve either as motors or generators (for regenerative braking). They are directly coupled to the front wheels (P4) by means of a fixed gear ratio. A Li-ion high-voltage (HV) battery is the electrochemical energy source for electric propulsion. The hybrid path, instead, includes a 5.2 liter Fuel Stratified Injection engine, another electrical machine used as an Integrated Starter-Generator (ISG) and directly mounted on the crankshaft (P1), a six-gear dual-clutch automatic manual transmission, and a differential gear. The motors and the ISG are represented by the same electrical machine, whose performance are listed in Tab. 3.1.

Depending on the selected driving mode, the two propulsion paths can work independently or together. If the vehicle is in pure electric mode, the propulsion comes only from the electrical machines on the front axle, so the engine is kept switched off and the clutch is open. In this condition, a Front-Wheel-Driving

(FWD) is performed. If the vehicle is in hybrid mode, both the engine and P4 motors can work in combination to fulfill the torque request, and thus Four-Wheel-Drive (4WD) can be achieved.

A schematic and simplified representation of the in-vehicle battery cooling circuit is given in Fig. 3.2. As it can be seen, it comprehends two different thermodynamic loops: the refrigerant and the coolant one.

Data regarding battery cooling circuit actuators are listed in Tab. 3.2.

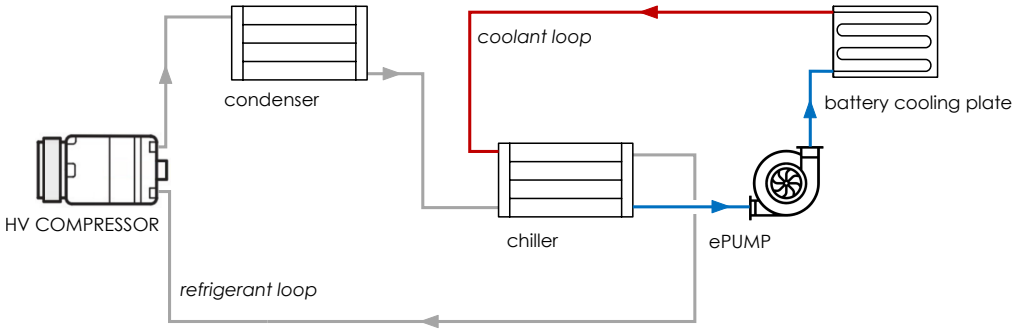

Figure 3.2: Schematic representation of the in-vehicle battery cooling circuit.

Table 3.2: Battery cooling circuit data.

Parameter(s)	**Value(s)**	
Pump nominal speed	7000	rpm
Pump nominal volume flow	20	l/min
Pump nominal power	50	W
Compressor nominal speed	3000	rpm
Compressor max power	4	kW

In the refrigerant loop, a high-voltage compressor, directly supplied by the battery, pressurizes the refrigerant, which is a two-phase fluid. This means that it is subjected to different phase transitions during the refrigeration cycle: from vapor to liquid in the condenser, releasing heat into the environment, and viceversa, in the chiller, where heat is absorbed from the coolant. Thus, the chiller represents the common heat exchanger where the heat transfer between the refrigerant and the coolant takes place. In the other loop, the coolant (a water-glycol mixture) absorbs the heat generated within the battery pack by flowing through a cooling plate. An

electrical (low-voltage) pump is installed to provide the necessary coolant flow rate.

3.2 Modeling approach for energy analysis

In order to provide an energy and efficiency assessment of a vehicle, the fuel consumption has to be estimated and with this aim different simulation approaches can be adopted.

In a *forward-facing* simulator, the source of the energy flow is represented by the propellers and the sink corresponds to the wheels, at which velocity and acceleration are evaluated. As shown in Fig. 3.3a, these output signals are involved in a closed-loop control (using a PI controller) operated by an effective driver model with the role of following a target input signal, namely the speed profile of a certain driving cycle. Thus, this approach can include dynamic effects and consequently performance- and drivability-focused simulations can be performed. In fact, the adoption of a driver model introduces realistic discrepancies between the target and the effective vehicle speed, evaluated as a consequence of the applied control actions. For this reason, this methodology can be referred to as *dynamic* approach.

On the other hand, a *backward-facing* simulator is based on the inverted path of the energy flow inside the vehicle. Here, as it can be noticed in Fig. 3.3b, the traction force, and consequently torque and power, are evaluated on the basis of the vehicle speed and the other parameters representing the given driving missions, which is then assumed to be perfectly followed. Therefore, there is no closed-loop control on the latter parameter, i.e. a driver model is not needed. Since this approach does not involve any powertrain dynamics, it is also referred to as *quasi-static*.

A *forward-backward* approach, resulting form a combination of the presented methodologies, can also be used. As shown in Fig. 3.3c, the powertrain is dynamically modeled with a forward approach, since the vehicle speed is the result of the control chain. The latter is based on a backward model, used by the driver to compute the torque set-point. In this way, the advantages of both the approaches

are achieved. From one hand, the accuracy of the speed-following control is increased due to the feedback of the effective vehicle speed, as it would happen for a realistic driver. On the other, the dynamic powertrain model ensures power limitations of each component, introduced by the forward-facing energy flow.

3.2.1 Approaches used in this work

As will be explained in Chapter 5, the main objective of the predictive function is represented by the evaluation of the battery power request, and thus the temperature behavior, with no particular attention to the energy management optimization problems, and therefore the backward approach is used in this case. Moreover, since dynamic effects such as torque control are not inherently included, a quasi-static approach results in a less complex model with benefits regarding the computational load. In addition to the benefits in terms of real-time capability, this characteristic is of fundamental importance when a significant amount of data, such as those related to navigation, has to be processed for the prediction of future working conditions of the components.

A backward-facing approach has been adopted, as well, for the backward optimization algorithm of dynamic programming. The reason for this choice relies on the evaluation of the objective function of the optimal control strategies. In fact, to evaluate the cost associated to each control policy, all the state variables of the system, from which the cost-to-go is evaluated, have to be recursively evaluated from the given driving mission, i.e. speed and slope traces, that act as disturbances on the dynamic system represented by the hybrid powertrain.

In order to properly conduct the energy analysis of the vehicle comprehending the developed control strategies, a forward-backward simulator has been chosen for vehicle modeling at Software-in-the-Loop level, which is further described in Chapter 4. In this way, the actuators set-points evaluated by each tested strategy can be applied to the powertrain. Moreover, the input drive cycle can be followed with high accuracy by considering the power limitation of each component.

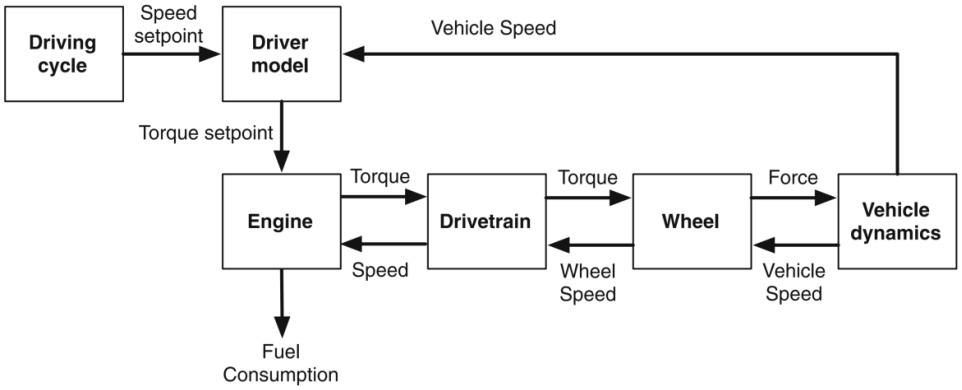

(a) Forward.

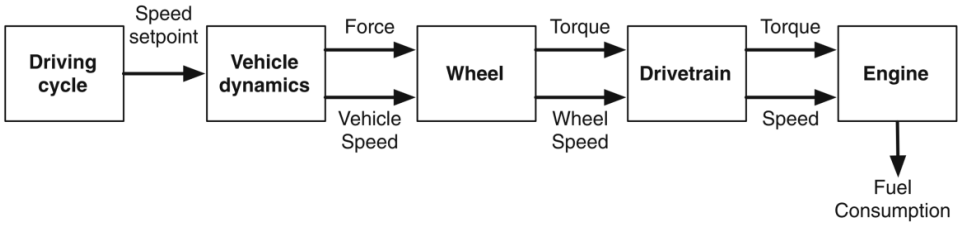

(b) Backward.

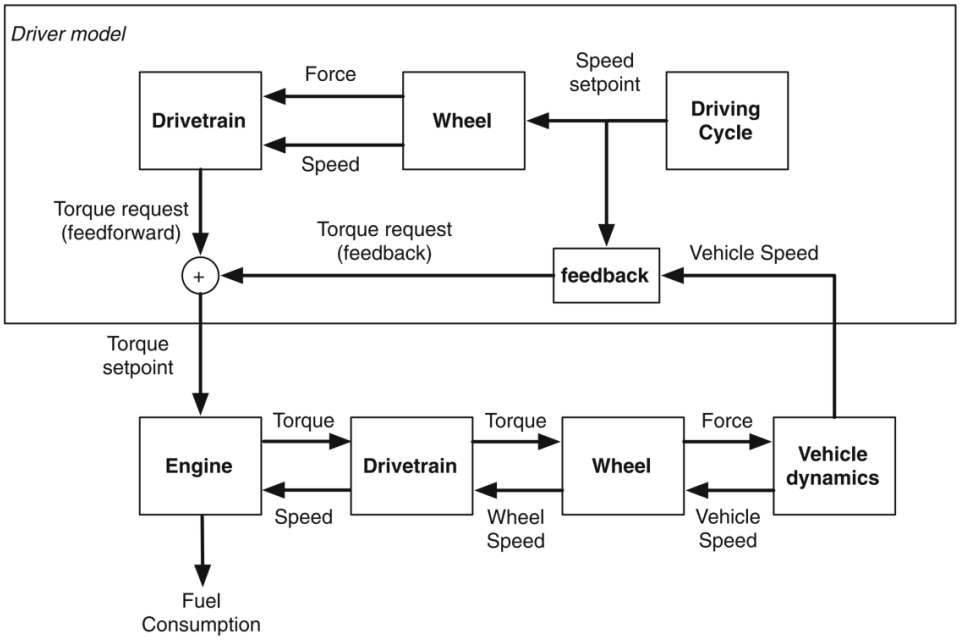

(c) Forward-backward.

Figure 3.3: Powertrain modeling approaches based on the direction of the energy flow [50].

3.3 Powertrain components

In this section, the modeling of the main powertrain components is presented, from vehicle dynamics to the electrical and thermal characterization of the high-voltage battery.

3.3.1 Longitudinal dynamics

Since the objective of the present work is represented by energy assessments of HEVs, performance analyses focused on drivability (vehicle stability, handling, etc.) and comfort (noise, harshness. and vibrations) issues are neglected. For this reason, lateral and horizontal vehicle dynamics are not taken into account. Hence, considering Fig. 3.4, the fundamental equation representing the longitudinal dynamics of a vehicle in motion is the following:

$$m_v \cdot \frac{d}{dt} v(t) = F_{mot}(t) - F_{res}(t) \tag{3.1}$$

where m_v, v are the mass and the speed of the vehicle, F_{mot} is the propulsion force supplied by the internal combustion engine and/or the electrical machines (P4), and F_{res} is the resistant force acting on the vehicle. The latter can be expressed as follows:

$$F_{res}(t) = F_a(t) + F_r(t) + F_g(t) \tag{3.2}$$

where:

F_a : aerodynamic friction losses generated by viscous friction of the surrounding air on the vehicle surface and pressure difference between the front and the rear of the vehicle due to air flow separation;

F_r : rolling friction losses at the contact surface between wheels and road, mainly affected by vehicle speed, tires pressure and road conditions;

F_g : gravitational force caused by driving the vehicle on an inclined road.

Because both air and rolling friction losses depend on vehicle speed, it is a matter of practicality considering drag and friction forces not separately. In particular, their contributions can be gathered in a single polynomial expression

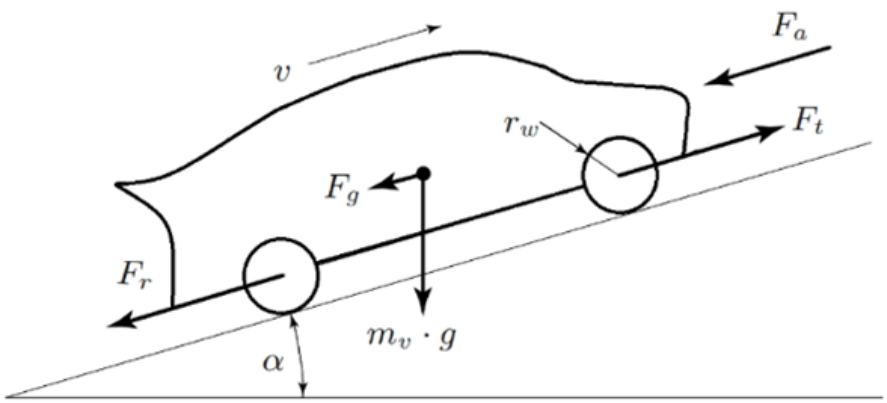

Figure 3.4: Forces acting on a vehicle in motion.

as a function of $v(t)$ with coefficients depending on the considered vehicle and which can be practically obtained by means of a *coast-down test*.

As explained in [107], the test consists in driving the vehicle in a flat road at a certain reference speed and then starting the coast-down deceleration phase, which means the transmission shall be in neutral and the engine shall run in idle. Moreover, the brakes shall not be operated during coasting. Experimental data of measured vehicle speed are then fit with a regression curve, namely the *total-resistance curve*, which has the following form:

$$F_{cd}(t) = F_a(t) + F_r(t) = f_0 + f_1 \cdot v(t) + f_2 \cdot v^2(t) \tag{3.3}$$

where f_0 is the constant term [N], f_1 is the coefficient of the first-order term [N/(km/h)], f_2 is the coefficient of the second-order term [N/(km/h)^2].

The force induced by gravitational field on the vehicle when driving on a road with non-null gradient is as follows:

$$F_g(t) = m_v \cdot g \cdot \sin \alpha(t) \tag{3.4}$$

where $\alpha(t)$ is the slope angle [rad] of the road, which can be derived from percentage slope $\alpha_{\%}(t)$ by the relationship

$$\alpha(t) = \arctan \frac{\alpha_{\%}(t)}{100} \tag{3.5}$$

Hence, the resistant force has the following expression:

$$F_{res}(t) = f_0 + f_1 \cdot v(t) + f_2 \cdot v^2(t) + m_v \cdot g \cdot \sin \alpha(t) \tag{3.6}$$

By substitution of Eq. (3.3), Eq. (3.4) in Eq. (3.2), the fundamental equation Eq. (3.1) can be written in the form of a non-homogeneous first-order non-linear ODE.

Therefore, the acceleration and the velocity of the vehicle, which represent the output of the vehicle model, can be evaluated, resulting in the forward-facing approach. On the other hand, if the driving cycle is assumed to be perfectly followed, and then the vehicle speed is considered an input variable, the traction force F_{mot} is evaluated from the same equation. In this way, the backward approach is realized.

3.3.2 Internal combustion engine

The internal combustion engine model is based on static maps and a lumped-parameter dynamic sub-model, which considers the inertia of the crankshaft and the flywheel. It is modeled as a torque generator, where the requested torque input is evaluated by the supervisory controller and then saturated according to engine limitations:

$$T_{req} = \min \left(T_{\max}(\omega), T_{in} - T_{fr}(\omega, \vartheta_{cool}, \vartheta_{oil}) \right) \tag{3.7}$$

where T_{max} is the maximum available engine torque at the current speed ω, T_{in} and T_{fr} are the indicated and the friction torque, respectively, with the latter depending on the engine speed and the temperature of the coolant ϑ_{cool} and the lubricant ϑ_{oil}.

As shown in Fig. 3.5a, a fuel consumption map is adopted, having as input variables the torque and the speed of the engine. For reasons of confidentiality, the fuel consumption has been normalized with respect to the maximum value. An engine efficiency map, depicted in Fig. 3.5b, is also implemented for the energy analyses and results discussion, as shown in Chapter 6. In both maps the maximum torque curve, depending on the engine speed and represented in terms of brake mean effective pressure (BMEP) by a black line in bold , can be noticed. The fuel consumption map has been generated by engine characterization at the test cell,

while the efficiency map has been obtained as follows.

The *brake mean effective pressure*, p_{bme}, is defined as:

$$p_{bme} = \frac{4\pi}{V_d} T \tag{3.8}$$

being V_d the engine displacement and T the provided torque.

The total engine efficiency can be then evaluated as the ratio between the output and input energies. The former is the mechanical energy transferred to the crankshaft, while the latter is the chemical energy stored in the fuel. Since the definition involving powers has a higher practical approach, the engine efficiency η_{tot} is usually defined as:

$$\eta_{tot} = \frac{P_{mech}}{P_{fuel}} = \frac{T \cdot w}{\dot{m}_f \cdot Q_{lhv}} \tag{3.9}$$

where $\dot{m}_f$ is the fuel mass flow, available from Fig. 3.5a, and Q_{lhv} is the lower heating value of the fuel, i.e. the amount of chemical energy par unit of fuel mass.

It is not unusual to map the *brake specific fuel consumption*, $BSFC$, instead of the engine efficiency, which is defined as the amount of fuel per unit of mechanical energy output (work, W):

$$BSFC = \frac{m_f}{W} = \frac{\dot{m}_f}{P_{mech}} \tag{3.10}$$

Then, combining Eq. (3.10) with Eq. (3.9), the relationship between the total engine efficiency and the $BSFC$ can be obtained:

$$\eta_{tot} = \frac{1}{BSFC \cdot Q_{lhv}} \tag{3.11}$$

3.3.3 Electric machines

The electric machines, namely the P1 (ISG) and P4 motors, have been modeled following the same approach presented for the internal combustion engine.

In particular, since all the installed motors are identical machines, a unique efficiency map accounts for energy losses occurring at the motor-inverter side.

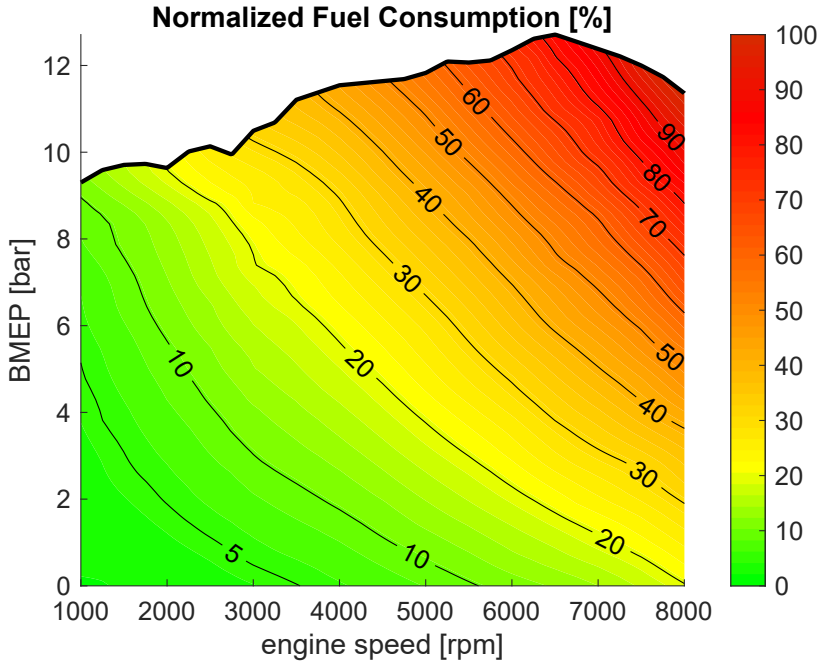

(a) Normalized fuel consumption.

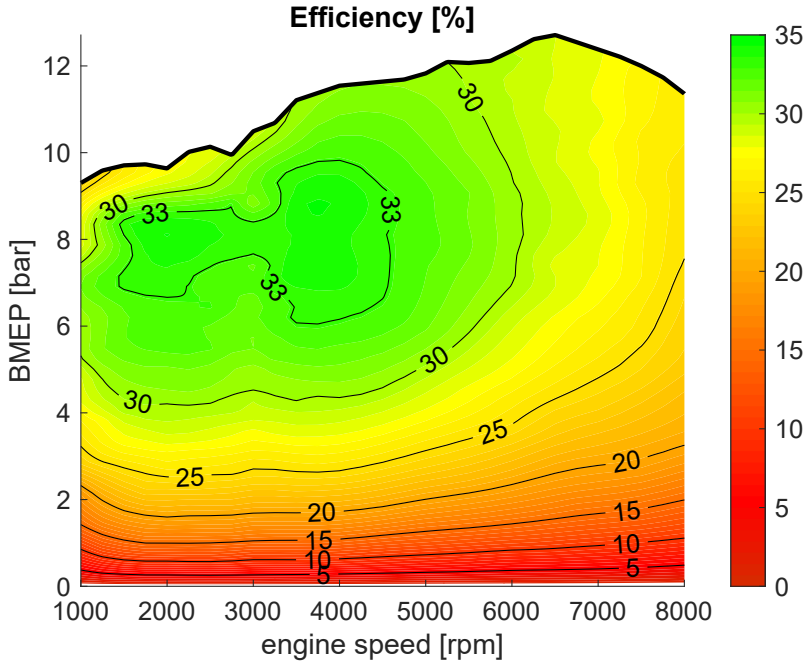

(b) Efficiency.

Figure 3.5: Maps used for engine modeling.

As can be noticed from the map shown in Fig. 3.6, provided by the component manufacturer, the motor efficiency depends on speed and torque and iso-efficiency lines are shown, as well. As it is well-known, the efficiencies characterizing an electric machine are much higher than the ones of an internal combustion engine, which is strongly penalized by the conversion of the thermal energy into the mechanical one and by thermal power losses through the wall of the combustion chambers and the exhaust gases.

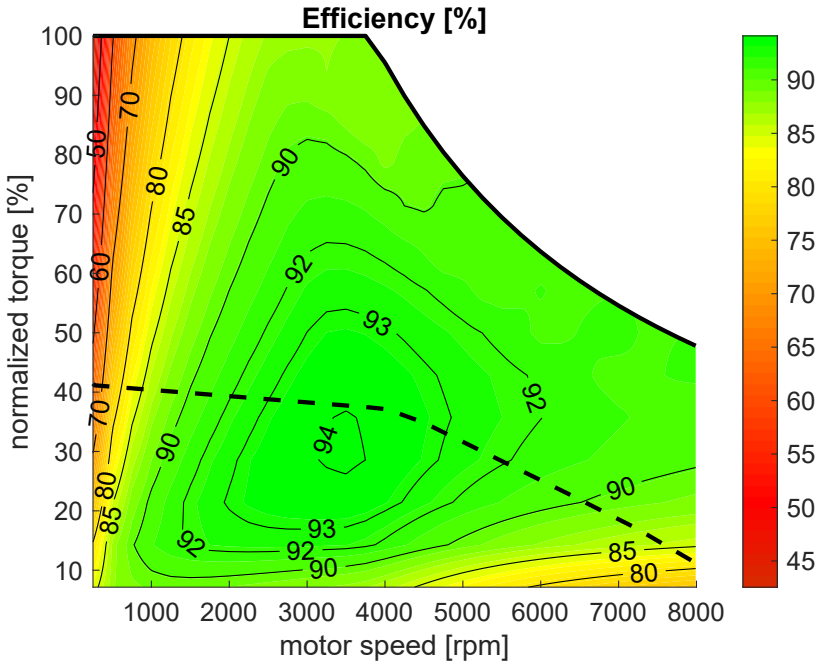

Figure 3.6: Efficiency map used for motors modeling.

The standard operating mode of an electric machine consists in a continuous power rating, which can be supported for long period of time. In case of high performance request, such a component is able to provide a peak power for brief time intervals. As a consequence, two threshold curves of maximum torque can be defined, namely in *continuous* and *peak* operating modes. Another benefit of using electric machines is that the maximum torque can be provided even at low speeds. In this way, considering Fig. 3.7, two different trends in terms of maximum performance can be pointed out: the first phase is characterized by a constant-torque behavior exhibits, followed by a constant-power one. The value

of speed at which this transition takes place is called *base speed*, ω_b. For the sake of simplicity, neglecting electrical and magnetic effects (flux weakening, etc.), a simple mathematical description from a mechanical point of view of this behavior of electric machines may be expressed as:

$$\begin{cases} T_{lim} = T_{\max} = const. \Rightarrow P_{lim} = T_{\max}\omega \propto \omega, & \omega \leq \omega_b \\ P_{lim} = P_{\max} = const. \Rightarrow T_{lim} = P_{\max}/\omega \propto 1/\omega, & \omega > \omega_b \end{cases} \tag{3.12}$$

where the maximum torque $T_{\max}$ is provided for $\omega \leq \omega_b$, and hence the maximum power $P_{\max}$ can be delivered only at higher speeds $\omega > \omega_b$.

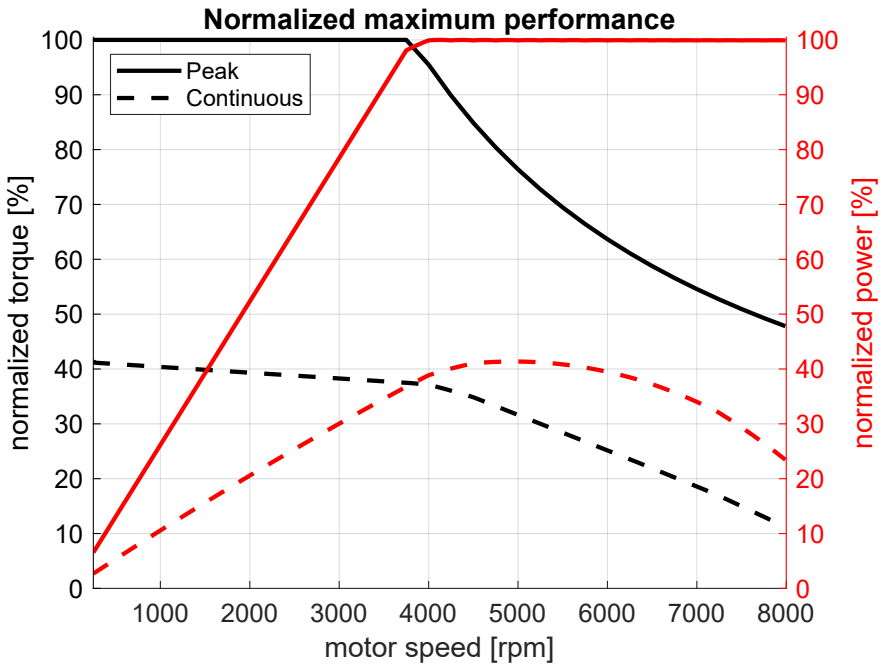

Figure 3.7: Motors maximum torque and power, in peak and continuous conditions.

Since electric machines can act as motor as well as generator, in the latter case all the considerations previously made are still valid. This means that the same maximum performance, with negative signs (resistant torque and power), are achieved. Moreover, as a generator, the electric machine is able to convert the input mechanical energy in electrical energy. This is the case of regenerative braking, when the kinetic energy of the vehicle is reduced by the generator whose rotor is

mechanically driven, and thus a current flow is produced. The same concepts lies behind the load point shifting strategy, since the engine provides a torque surplus which is absorbed by the generator. In both cases, the produced electrical energy is transferred to the battery for charge increasing. Nevertheless, it is worth to point out that the direction of the energy flow within the electric machine affects the efficiency of the energy conversion, from mechanical to electrical (generator) and viceversa (motor). In formulas:

$$P_{el} = \frac{P_{mech}}{\eta^{\alpha}(\omega,T)} = \frac{T\ \omega}{\eta^{\alpha}(\omega,T)}, \quad \alpha = \begin{cases} 1, & T \geq 0 \text{ (motor)} \\ -1, & T < 0 \text{ (generator)} \end{cases} \tag{3.13}$$

with obvious meanings of the symbols.

3.3.4 Driver

As introduced in Section 3.2.1, a driver model is implemented in the simulator with the aim to follow the speed set-point related to the given driving mission.

Since the simulator is based on a forward-backward approach, the measured (calculated) vehicle speed, resulting from the application of the control chain on the driveline, is used as a feedback signal to improve the accuracy of the speed following capability. In particular, the error of the calculated and the target speed is fed into different proportional-integral (PI) controllers to compute accelerator and brake pedal signals.

The steering angle is not calculated because only vehicle longitudinal dynamics are taken into account. The gear is not evaluated, as well, since the transmission control is set to automatic. The driver torque request, mapped as a function of vehicle speed and accelerator pedal, is estimated by the supervisory controller, which then evaluates the torque split factor according to the chosen energy management strategy.

3.3.5 Electric power distribution

The electric power distribution of the considered vehicle is depicted in Fig. 3.8. it consists of a high-voltage (HV, red line) and a low-voltage (LV, blue line) bus.

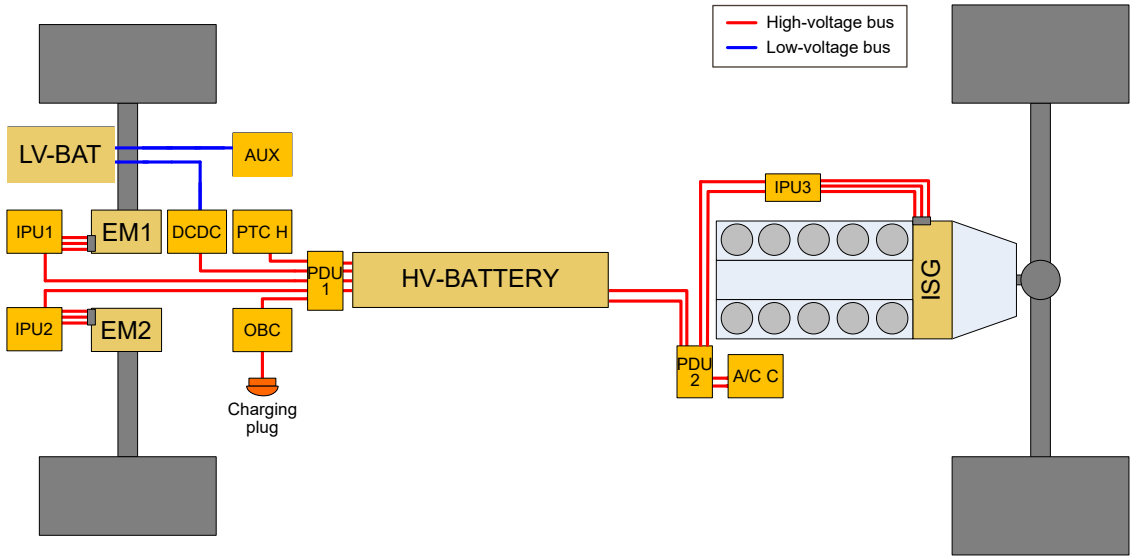

Figure 3.8: Diagram of the electric power distribution.

The HV battery, the electric machines (EM, ISG) including inverters (IPUs, intelligent power units), the air-conditioning (AC) compressor, the PTC (positive temperature coefficient) heater, the DC-to-DC (DCDC) converter and the on-board charging (OBC) device are all connected to the high-voltage bus. The power inverters convert the direct-current (DC) power input of the HV battery into an alternating-current (AC) three-phase output for electric motors speed control. The AC compressor is used not only for cabin conditioning, but even for battery cooling, as previously described in Section 3.1. The electric power distribution among these components is managed by specific devices, named power distribution units (PDUs). In formula, the battery power output P_b can be expressed as:

$$P_b = V_b \cdot I_b = V_b \left(I_{EM1} + I_{EM2} + I_{ISG} + I_{DCDC} + I_{ACC} + I_{PTC} + I_{OBC}\right) \tag{3.14}$$

where V_b is the voltage of the battery and, then, of the bus, and I denotes the current flow. Considering the last term, by multiplying V_b for each current, the power request for each component is calculated. The battery power request can be either negative or positive, depending on the current flow. The convention adopted in this work considers a negative power output as an incoming current

flow to the battery, resulting in charge increasing. On the other hand, during traction, the battery will provide the required positive power to the driveline, resulting in charge decreasing. In the presented work, neither cabin conditioning nor external charging have been taken into account in the context of control strategies development. Hence, considering Eq. (3.14), this leads to $I_{PTC} = I_{OBC} = 0$.

With regards to the low-voltage bus, the DCDC converts the DC input of the HV bus to a DC low-voltage power output. Hence, this component manages the power distribution between the two buses in order to maintain the state of charge of the LV battery (12V, in this case) around a certain constant value. The latter supplies all the components requiring auxiliary loads, such as water pumps, cooling fans, sensors, infotainment, and electronic control units.

3.4 High-voltage battery

The high-voltage battery is a key component in hybrid electric vehicles. To this aim, a control-oriented model of the battery including electrical and thermal behaviors has been developed, calibrated and validated over experimental data. The output parameters of the battery model are its voltage, current, state of charge, and temperature. Compressor power request is calculated, as well, by a simplified cooling circuit model.

3.4.1 Electrical model

3.4.1.1 Modeling

The electrical behavior of the cell has been represented by a single-polarization equivalent circuit model, also known as first-order RC equivalent circuit model. Although several approaches can be adopted for modeling batteries, in equivalent circuit modeling, electrical circuits made of equivalent components are used for the evaluation of battery voltage and power losses. Thus, model complexity and computational time are reduced [108]. For the same reason, the approach followed in this research project is based on the identification of a single resistor-capacitor

(RC) network to reproduce the electrical behavior of the battery pack with enough accuracy for control-oriented modeling of the component [109, 110].

As depicted in Fig. 3.9, the single polarization equivalent circuit model comprehends an open-circuit voltage (OCV), V_{OC}, a resistor, R_0, representing the ohmic resistance caused by the accumulation and dissipation of charge in the electrical layer, while R_1 and C_1 are the activation polarization resistance and capacitance respectively, which characterize the fast transient response of the cell to a current pulse. All the mentioned parameters usually depend on cell SoC, ξ, and temperature, ϑ.

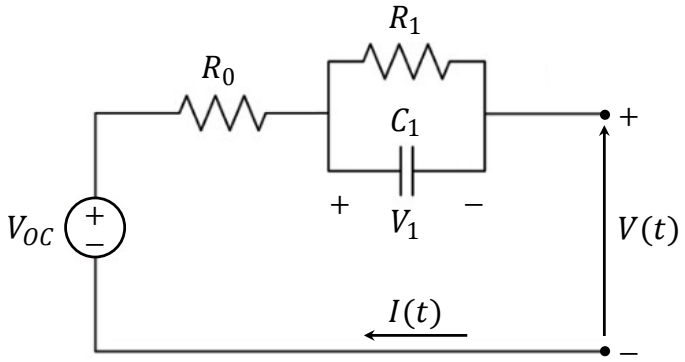

Figure 3.9: Single-polarization equivalent circuit model for cell electrical characterization.

When considering a battery pack consisting of n_p strings made of n_s cells, the battery voltage V_b and current I_b can be calculated from the following system of equations:

$$\begin{cases} V_b(t) = \left(V_{OC} - R_0 \cdot I_b(t)/n_p - V_1\right) n_s \\ P_b(t) = V_b(t) \cdot I_b(t) \end{cases} \tag{3.15}$$

where:

$$I_b(t) = I_c(t) \cdot n_p \tag{3.16}$$

$$V_b(t) = V_c(t) \cdot n_s \tag{3.17}$$

$$P_b(t) = P_{EM1}(t) + P_{EM2}(t) + P_{ISG}(t) + P_{ACC}(t) + \frac{P_{aux}}{\eta_{DCDC}} \tag{3.18}$$

and being:

V_c, I_c : cell voltage and current, respectively;
V_1 : voltage drop related to the RC circuit;
P_b : battery power request, which can be evaluated from Eq. (3.14) considering $P_{DCDC} = P_{aux}/\eta_{DCDC}$ and assuming constant both the auxiliary load P_{aux} and the DCDC efficiency η_{DCDC}.

It is then possible to calculate the power losses $P_{b,loss}$ of the battery due to resistive heating as follows:

$$P_{b,loss}(t) = V_{b,int}(t) \cdot I_b(t) = \frac{n_s}{n_p} R_0 \cdot I_b^2(t) + n_s V_1 \cdot I_b(t) \tag{3.19}$$

in which $V_{b,int} = (n_s V_{OC} - V_b(t))$, from Eq. (3.15), is the internal voltage drop of the battery due to the presence of the internal resistance that causes the power dissipation $P_{b,loss}$ when the current I_b is flowing in the circuit.

Then, the battery state of charge is estimated with an Ampere-hour (Ah) integral method (also known as *Coulomb counting*) [111]. In formula:

$$\xi(t) = \xi_i - \frac{\eta_c}{C_n} \int I_b(t) dt \tag{3.20}$$

being C_n the nominal battery capacity [Ah], η_c the coulombic efficiency, and ξ_i the initial value of the state of charge.

3.4.1.2 Calibration and validation

The parametrization of the cell electrical model is the first step to be accomplished. In particular, the single-polarization equivalent circuit model of the cell is identified by three parameters, depending on state of charge and temperature, i.e. R_0,R_1,$C_1 = f(\xi,\vartheta)$. The RC network is an efficient yet simple approach to characterize the typical transient behavior of cell voltage when currents are applied. This phenomenon can be accurately observed in pulse tests, which consist in applying to the cell a constant current (pulse) for a given period of time, at given temperature and state of charge. That is why such test cycles are usually involved in the cell electrical parametrization.

Applying the Kirchhoff's nodal rule to the closed RC loop of the equivalent circuit model depicted in Fig. 3.9, the following first-order linear differential equation applies:

$$\frac{d}{dt}V_1(t) + \frac{1}{\tau_1}V_1(t) = \frac{1}{C_1}I(t) \tag{3.21}$$

where $\tau_1 = R_1C_1$ represents the time constant of the related circuit, whose meaning will be clarified later in this section.

The solution is provided by the following equation:

$$V_1(t) = I_p R_1 \left(1 - e^{-t/\tau_1}\right) \tag{3.22}$$

where the assumption $I(t) = I_p = const.$ can be made, since pulse tests are used to characterize the cell. Moreover, the exponential decay of the network voltage V_1 can be then noticed, where the time constant τ defines the decay rate.

Thus, the voltage V_c of the cell subjected to the constant current flow I_p of the pulse test can be expressed as:

$$\begin{aligned} V_c(t) &= V_{oc} - \Delta V_c(t) \\ &= V_{oc} - (V_0 + V_1(t)) \\ &= V_{oc} - I_p \left[R_0 + R_1 \left(1 - e^{-t/(R_1C_1)}\right)\right] \end{aligned} \tag{3.23}$$

where the term in brackets can be referred to as *equivalent series resistance*, R_{es}, depending on the series resistance R_0 and the characteristic of the RC branch, R_1 and C_1.

At this point, since the open-circuit voltage $V_{oc} = f(\xi,\vartheta)$ is provided by the cell manufacturer, the calibration of the model can be conducted by finding the optimal set of $(R_0,R_1,C_1) = f(\xi,\vartheta)$ that minimizes the error of the analytical cell voltage (Eq. (3.23)) against the experimental one provided by the pulse tests. With this aim, the MATLAB `fminsearchbnd` function [112] has been used, which performs a bound constrained optimization using the native `fminsearch`. In particular, the function to be minimized is represented by the *root mean square error*, RMSE,

between the simulated V_c and the experimental voltage. In formula:

$$RMSE_V = \sqrt{\frac{1}{t_{exp}} \int_0^{t_{exp}} \left(V_{sim}(t) - V_{exp}(t)\right)^2 dt} \tag{3.24}$$

with $V_{sim} = V_c$, and t_{exp} the data acquisition time.

As an example, the parameter R_0 mapped as a function of battery SoC and temperature, in charge and discharge conditions, resulting from the model parametrization procedure, is depicted in Fig. 3.10.

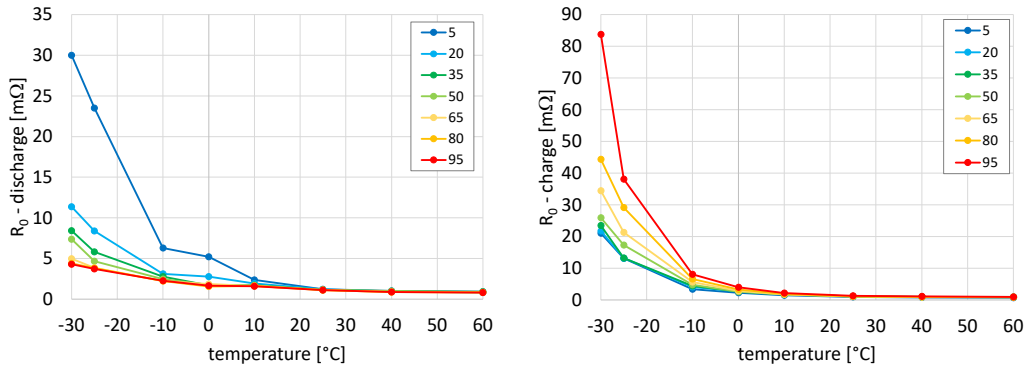

(a) Discharge.

(b) Charge.

Figure 3.10: Cell internal resistance R_0 as a function of state of charge and temperature.

The results of the calibration of the electric circuit model of the cell are represented in Fig. 3.12, where different pulse tests at $\vartheta = 20°C$ are shown. These tests have been conducted by the industrial partner in order to asses an electrical characterization of the given cell. In this case, as shown in Fig. 3.11, a curve fitting of the experimental data of the open-circuit voltage was necessary. Voltage is referred to the battery level according to Eq. (3.17).

Then, the electrical model has been validated using two different test cycles, as shown in Fig. 3.13. With regards to the second one (Fig. 3.13b), it consists in a current cycle defined by the industrial partner in order to test the battery in very demanding working conditions. As a result, the accuracy of the model can be considered acceptable for the control-oriented modeling since the maximum voltage error is below 10V in the SoC operating range of the battery.

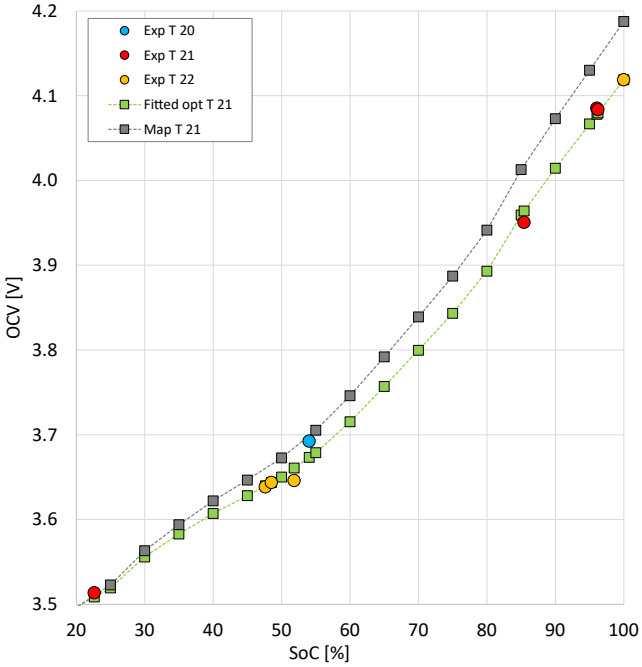

Figure 3.11: Fitting of the OCV map to experimental measures.

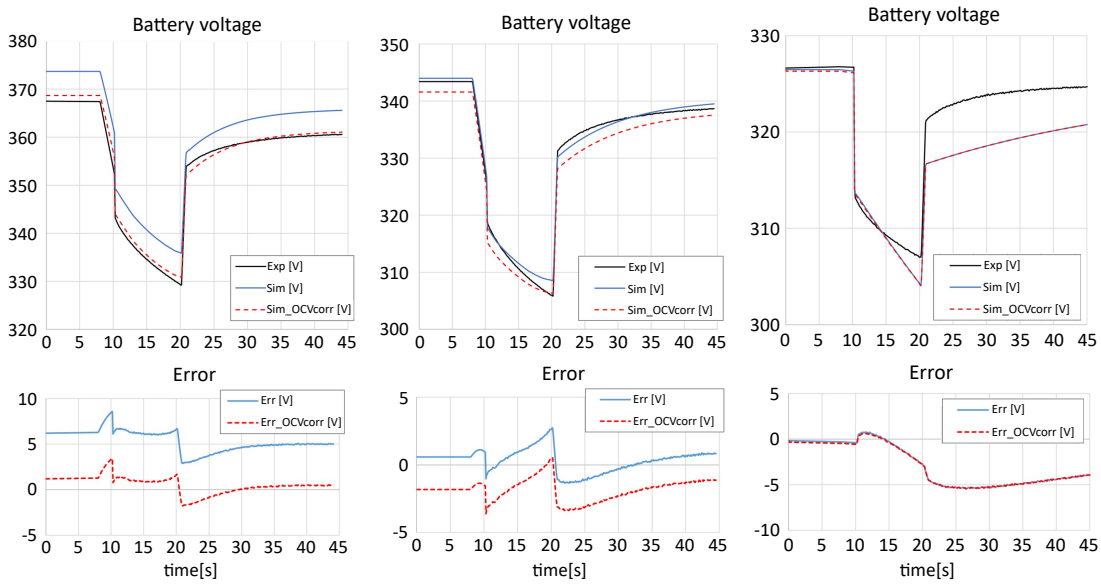

(a) Test 1: 400A, 85% SoC. **(b)** Test 2: 400A, 55% SoC. **(c)** Test 3: 200A, 25% SoC.

Figure 3.12: Calibration of the battery electrical model. Pulse tests at 20°C.

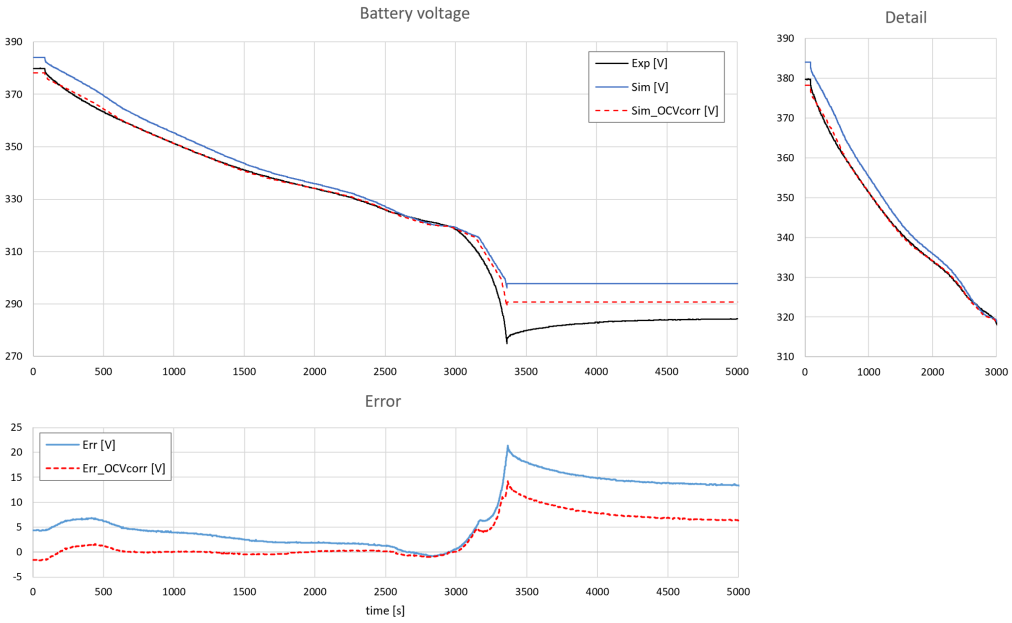

(a) Capacity test.

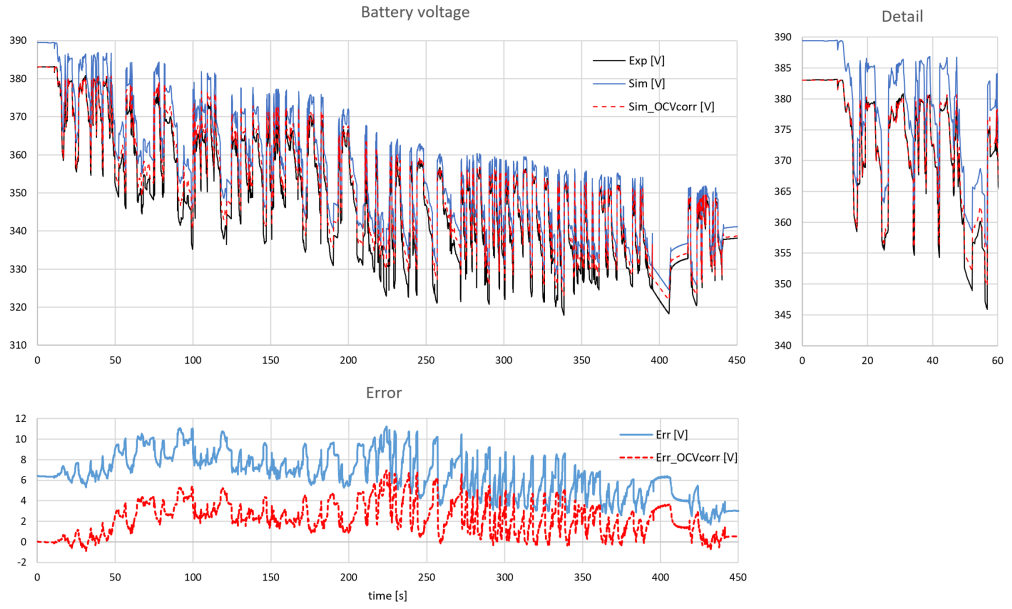

(b) Worst case test.

Figure 3.13: Validation of the battery electrical model.

3.4.2 Thermal and cooling circuit models

3.4.2.1 Modeling

Although several processes are involved in heat transfer for Li-ion batteries [113], a simplified approach for battery thermal modeling has been adopted, as well, being a control-oriented approach one of the main objectives of this work. In particular, contributions to heat losses by radiation and conduction have been neglected. Therefore, only the convective heat exchanges occurring at environment and coolant side have been considered. Therefore, the equation for energy balance applied to the whole battery pack can be written as:

$$m\ c_p\ \frac{d}{dt}\vartheta(t) = P_{b,loss}(t) - \left(\dot{Q}_{air}(t) - \dot{Q}_{cool}(t)\right) \tag{3.25}$$

which solved for the battery temperature ϑ gives:

$$\vartheta(t) = \vartheta_i + \frac{1}{m\ c_p}\int \left(P_{b,loss}(t) - \dot{Q}_{air}(t) - \dot{Q}_{cool}(t)\right) dt \tag{3.26}$$

where:

m, c_p : mass and specific heat capacity [J/(kg·K)], respectively, of the battery pack;

ϑ_i : initial battery temperature, assumed to be equal to the environmental one;

$P_{b,loss}$: battery power loss due to Joule heating effect, from Eq. (3.19);

$\dot{Q}_{cool}$: cooling heat rate due to battery-coolant convective heat exchange;

$\dot{Q}_{air}$: thermal power related to the air-battery convective heat exchange.

The latter can be expressed as:

$$\dot{Q}_{air}(t) = h_a(v(t)) \cdot S_a \cdot (\vartheta(t) - \vartheta_{amb}) \tag{3.27}$$

where $h_a(v(t))$ is the convective heat transfer coefficient [W/(K·m^2)] of the surrounding air, ϑ_{amb} is the ambient temperature, which is considered constant, and S_a is the surface where the heat exchange takes place, i.e. the external surface of the battery pack.

Moreover, the cooling heat rate $\dot{Q}_{cool}$ due to battery-coolant convective heat exchange can be formulated as:

$$\dot{Q}_{cool}(t) = h_c \cdot S_c \cdot \Delta\vartheta_{ml,c} \tag{3.28}$$

where h_c [W/(K·m^2)] is the convective heat transfer coefficient of the coolant, and S_c is the surface where the heat exchange takes place, i.e. the internal surface of the pipelines of the cooling plate.

The term $\Delta\vartheta_{ml,c}$, used to characterize the convective heat exchange, is referred to as *logarithmic mean temperature difference*. Let $\vartheta_1 = \vartheta - \vartheta_{c,out}$, $\vartheta_2 = \vartheta - \vartheta_{c,in}$, where $\vartheta_{c,in}$ and $\vartheta_{c,out}$ are the coolant temperatures at cooling plate inlet and outlet, respectively. The logarithmic mean temperature difference is as follows:

$$\Delta\vartheta_{ml,c}(t) = \frac{\vartheta_2 - \vartheta_1}{\ln\left(\frac{\vartheta_2}{\vartheta_1}\right)} = \frac{\vartheta_{c,out} - \vartheta_{c,in}}{\ln\left(\frac{\vartheta - \vartheta_{c,in}}{\vartheta - \vartheta_{c,out}}\right)} \tag{3.29}$$

For the sake of simplicity, since the complexity of the integrated cooling circuit (Fig. 3.2) requires a high number of parameters for the mathematical description of the thermodynamics of the two cooling loops, resulting also in very demanding calibration and validation phases, the refrigerant loop has not been modeled. To this aim, the assumption $\vartheta_{c,out} = const.$ has been made. Although experimental data confirm the weakness of this approach, the control-oriented objective of the model justifies this choice, as shown by the validation of the model (Section 3.4.2.2).

Thus, in order to evaluate the outlet coolant temperature, the thermal balance can be applied:

$$\dot{Q}_{cool}(t) = \dot{m}_c \cdot c_c \cdot \Delta\vartheta_c(t) \tag{3.30}$$

which gives:

$$\vartheta_{c,out}(t) = \vartheta_{c,in} + \frac{\dot{Q}_{cool}(t)}{\rho_c \, \dot{V}_c \cdot c_c} \tag{3.31}$$

where c_c is the coolant heat specific capacity, $\dot{m}_c = \rho_c \, \dot{V}_c$ is the coolant mass flow rate, ρ_c the density, and $\dot{V}_c$ is the pump volume flow, which can be considered

constant with good approximation while operating.

Finally, the electrical power absorption due to the high-voltage compressor can be calculated as:

$$P_{ACC}(t) = \dot{Q}_{cool}(t)\frac{COP}{\eta_{ch}} \tag{3.32}$$

where η_{ch} is the efficiency of the chiller, and COP is the coefficient of performance of the refrigerant cycle, defined as the ratio between the cooling power output and the electrical power input of the system. The latter was assumed to be constant, and thus not varying as a function of compressor speed.

The electrical power request related to the ePump is assumed to be constant while operating and equal to $P_{eP} = 50$ W, as reported in Tab. 3.2. In this case, this contribution is added to the auxiliaries power P_{aux} appearing in Eq. (3.18).

3.4.2.2 Calibration and validation

As discussed in the previous section, since the cooling circuit and battery thermal models are inherently connected, they have been calibrated and validated simultaneously. With this aim, the used experimental data have been recorded during tests run at the Nardò Technical Center, where the vehicle cooling systems were validated and the performance was measured [106].

The following parameters have been chosen as calibration variables:

- the specific heat capacity c_p [J/(kg·K)] of the battery pack (see: Eq. (3.25));
- the convection heat transfer coefficient h_c [W/(K·m^2)] of the coolant (see: Eq. (3.28)).

The set of experimental data shown in Fig. 3.15 has been used for model calibration. For each test and for each value of the calibration set, $(c_p,h_c)_i$, the RMSE between experimental and simulated average battery temperature has been calculated as key performance index of the model.

For an overall comparison of the obtained results, the mean RMSEs for each $(c_p,h_c)_i$ have been evaluated considering all the test cycles and collected together in the map depicted in Fig. 3.14. The optimal values are those showing the minimum overall mean RMSE, while in Fig. 3.16 simulated battery temperatures for those values are shown.

In Fig. 3.17 the set of experimental data used for model validation is shown. In Fig. 3.18 simulated battery temperatures for the optimal calibration values are finally shown.

As it can be noticed from both Fig. 3.16 and Fig. 3.18, the segmented behavior of the experimental battery temperature is due to the integer data type used for numerical representation. As a matter of fact, this approach is usually adopted for parameters involved in thermodynamics effects, which exhibit slow transients, then justifying the integer representation. Therefore, a certain confidence interval of width $\Delta T = \pm 0.5$°C has to be considered for the given experimental temperatures.

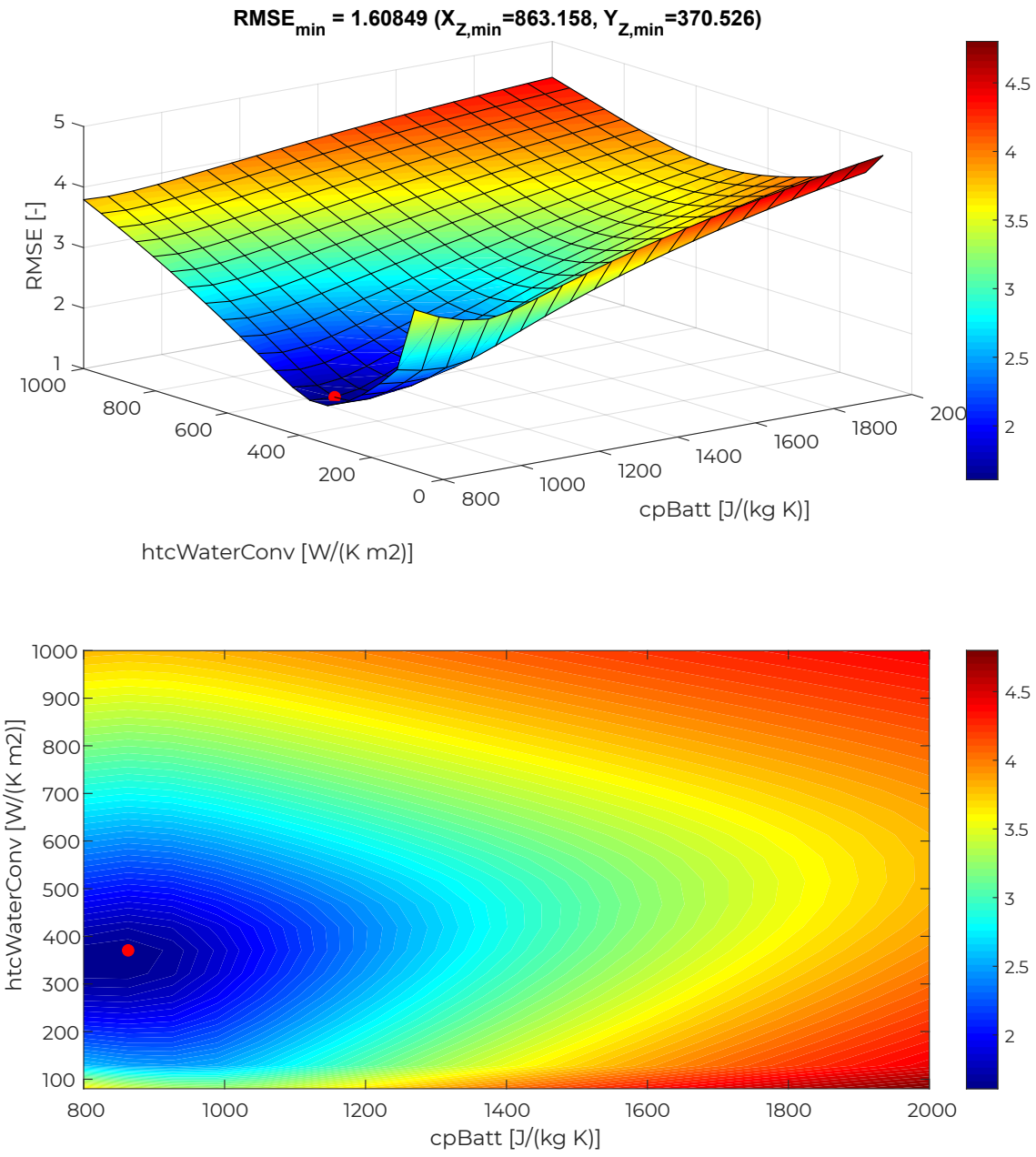

Figure 3.14: Overall temperature mean RMSE as a function of the calibration parameters.

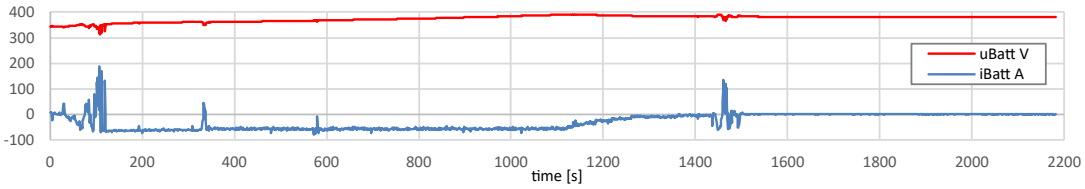

(a) Test 1.

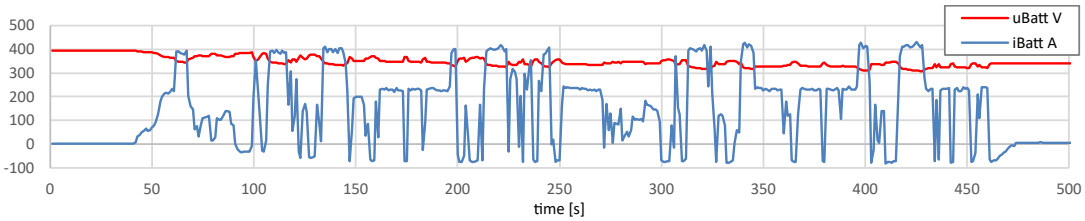

(b) Test 2

Figure 3.15: Experimental data used for battery thermal model calibration.

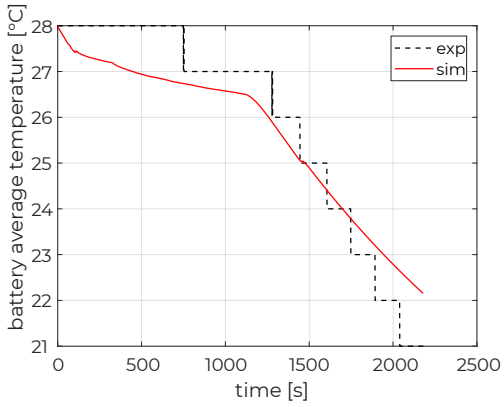

(a) Test 1.

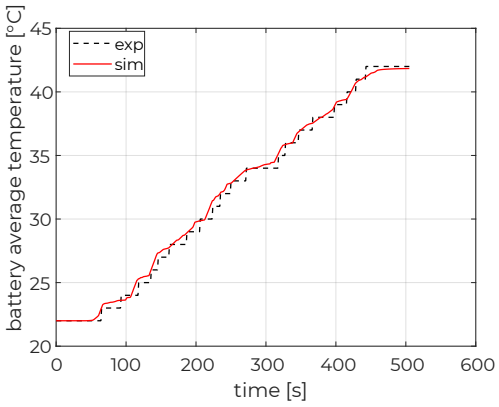

(b) Test 2.

Figure 3.16: Simulated battery temperature with optimal values of the calibration parameters. Calibration.

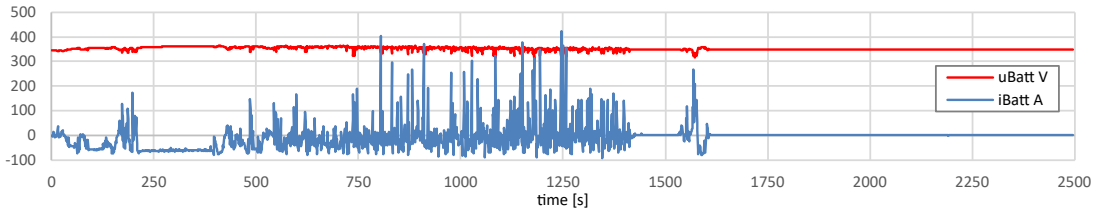

(a) TEST 1.

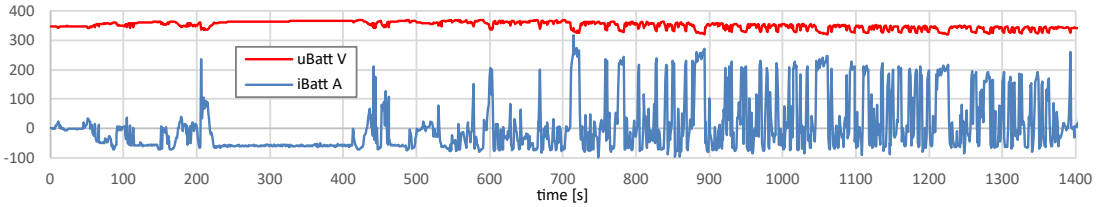

(b) TEST 2.

Figure 3.17: Experimental data used for battery thermal model validation.

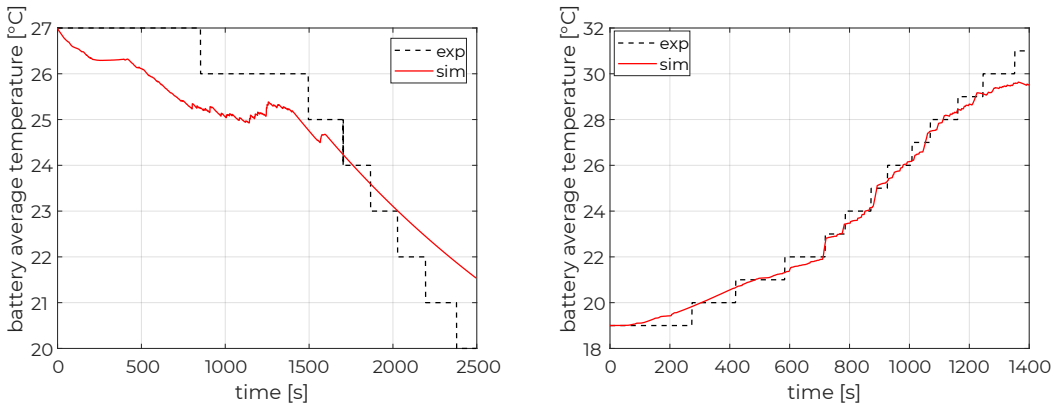

(a) Test 1.

(b) Test 2.

Figure 3.18: Simulated battery temperature with optimal values of the calibration parameters. Validation.

Chapter 4

Simulation environments

Different simulation environments have been developed in this work. in particular, a Software-in-the-Loop and a Hardware-in-the-Loop simulator have been set up and validated for control strategies development and testing.

4.1 Simulation and testing methodology

Nowadays, vehicle development processes follow the well-known *V-Model* or *V-Cycle* approach, which is a consolidated methodology in the automotive industry [114, 115].

As it can be seen from Fig. 4.1a, the V-model represents a special case of a waterfall model that describes the sequential steps of product development. In such an approach the defined targets are divided in sub-sequential levels: from system to components in the design phase (left branch), and backward during testing and validation (right branch). The cyclic nature of the V-Model consists in the data feedback from one branch to the other, resulting in a more accurate control of the whole development process. In particular, one of the main benefits of this methodology is the shortening of the time-to-market of the product, as shown in Fig. 4.1b.

From a vehicle control point of view, Software-in-the-Loop (SiL) and Hardware-in-the-Loop (HiL) simulation environments play an important role because they can speed up and improve the efficiency of the development, the testing and the

integration of the powertrain control strategies, while reducing the product global costs. In general, the advantage of a *Road-to-Rig-to-Desktop* approach, which relies on representative simulation platforms, is represented by higher reproducibility and reliability of the involved processes with respect to conventional methodologies.

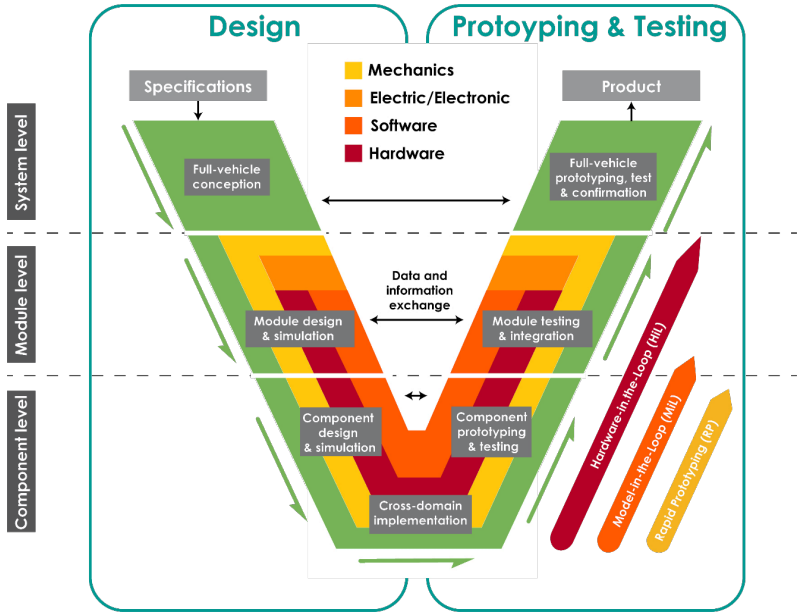

(a) Diagram.

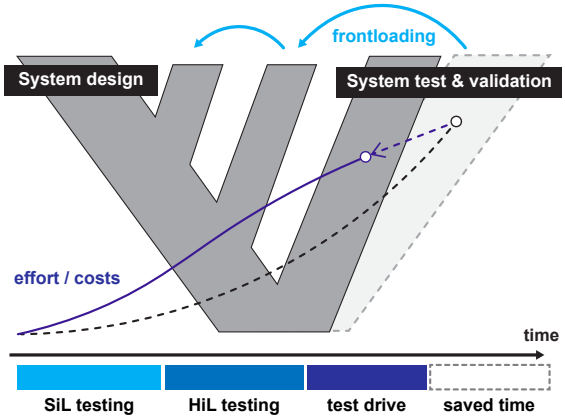

(b) Effort/costs impact.

Figure 4.1: V-model approach.

4.2 Software-in-the-Loop

The SiL environment is here presented and described, with particular attention to the high-level software implemented in the vehicle model. An overview of the used simulation tools is given, as well.

4.2.1 Simulation tools

In order to reproduce all the dynamics of a vehicle, and especially the complexity of a hybrid powertrain, numerous engineering simulation tools have been developed over the years. Although they can be very different, a common classification can be furnished on the basis of the model representation. In particular, either an *analytical* or a *physical* approach can be used.

The former requires the user to manually insert differential equations describing the given phenomena. Like every formula, dependent and independent variables shall be set. As an example, considering a certain rotating element with its own inertia, the rotating balance allows to determine the speed of the component, which is the output, from the knowledge of the motoring and resistant torques acting on it, that are inputs to the system. Once variables are evaluated, they can be used in other analytical sub-models.

On the other hand, physical models rely on libraries, i.e. models describing single components by using equations systems already implemented. Thus, the major benefit of such an approach is the possibility to build up high-complexity models with a relative low effort for the user. In other words, these models are characterized by *a-causality*, meaning that neither inputs nor outputs have to be explicitly defined. In fact, the models interfaces are connected by means of physical signals, which can be intended as a gathering of all the analytical variables describing a given component.

In the automotive field, widely used tools for powertrain modeling and vehicle simulation are represented by The MathWorks® products, namely MATLAB® and *Simulink*®.

Simulink is a MATLAB suite for the design and the simulation of model-based design engineering systems which relies on graphic or visual programming. It

is an interactive way of programming that enables the user to manipulate visual objects, like symbols and blocks, to write a program, i.e. equations. To this aim, a graphical user interface is implemented. In this environment, with regards to the tools available in this environment, a particular mention is reserved to *Simscape*™. This utility enables the user to create multi-domain physical systems for modeling electric (*SimPowerSystems*™ and *SimElectronics*®) and mechanical components (*SimMechanics*™), powertrain dynamics (*SimDriveline*™), and many other aspects of the vehicle. Moreover, *Stateflow*® allows to implement decision logic using state machines and flow charts, being particularly suitable for the development of supervisory controllers.

Concerning the present work, the entire vehicle model, including powertrain components and all the controllers introduced in Chapter 3, has been developed in Simulink environment. In particular, SimDriveline and SimMechanics have been chosen to model the vehicle longitudinal dynamics, the transmission, the internal combustion engine and the electric machines, since the last two components are considered as simple torque generators. In this way, the physical modeling of these components allows also to properly capture and describe the involved inertial dyanmics. The high-level software of the Hybrid Control Unit (HCU), in which all the energy management strategies are implemented, has been developed in Simulink, as well.

4.2.2 Vehicle model

As stated in Section 3.2.1, the SiL model follows a forward-backward approach, which means there is a driver model capable of reproducing realistic acceleration and brake pedals signals. According to that, the model follows the conventional control chain present in a real vehicle. The driver request (pedals signals) is converted in wheels torque request (*drive-by-wire*), then vehicle and components control units manage the actuators in order to provide the necessary power demand to satisfy the driver request.

This modeling approach allows a more realistic simulation of the powertrain behavior, calculating not only the energy consumption, but also all the physical parameters representing the states evolution of the vehicle over time, such as

the actual vehicle speed and the machines behavior in terms of torque, speed, temperature.

The SiL vehicle simulator is divided in different parts:

- *Components*
  gathering all together the powertrain components, intended as actuators, such as engine, motors, battery, transmission;
- *Controllers*
  in which all the control unit installed on-board a real vehicle are modeled, following the operation they would have in real-time application;
- *Communication*
  reproducing the vehicle communication network.

All the data needed to implement the such detailed SiL derives from the existing vehicle prototype described in Section 3.1.

4.2.3 Software

The application layer of the in-vehicle Hybrid Control Unit (HCU) software has been implemented in the vehicle model. A detailed representation of the on-board Battery Management System (BMS) has been developed and implemented, as well.

4.2.3.1 Hybrid Control Unit

The Hybrid Control Unit manages all other ECUs. The HCU coordinates the requests to the powertrain's subsystems, in order to guarantee the vehicle's performance and all the safety requirements as:

- electric traction (without the need to add gearbox or clutch controls);
- front axle torque vectoring (without any electronic differential system);
- 4WD control;

- torque fill during shifting (shift assist system);
- boosting function.

In particular, regarding the 4WD control, the HCU calculates the driver torque request which is mapped as a function of the vehicle speed and the throttle pedal. When the latter is less than 5% and the vehicle is moving, the supervisor controller interprets this condition as a negative torque request, which is actuated by electric motors operating as generators (and thus regenerative braking is performed). If the whole negative torque cannot be supplied by the motors, then even mechanical braking takes place (and thus blended braking is performed).

4.2.3.2 Battery Management System

A highly detailed model of the application software of the on-board Battery Management System (BMS) has been implemented in the Real-Time PC in the present configuration.

It comprehends most of the functionalities of the real software, such as

- contactors control (for battery pre-charging);
- isolation monitoring;
- power limitation;
- system diagnostics.

Particular attention has been paid to the latter because error monitoring plays a vital role in preserving the safety of the vehicle's components and the passengers. Moreover, the implementation of the real HCU in the HiL facility has enabled the testing of this functionality before implementing on-board any control function. Therefore, the BMS is able to recognize if threshold values for monitoring are exceeded for several important parameters, such as battery voltage, current, power, and temperature. High-voltage interlock lines and battery isolation status are monitored, as well.

In case of errors and failure detection (overheating, overvoltage, overcurrent, etc.), the BMS sends this information to the HCU which takes remedial action

depending on the type and severity of the error. If such an action is not applied within a certain time, the BMS itself takes over control and opens the high-voltage relays. With this aim, the battery pre-charge circuit comprehending the contactors has been implemented in the battery model.

4.2.4 Validation

4.2.4.1 Vehicle model

The whole SiL model has been validated with experimental data acquired:

- during an All-Electric Range test [116], that consists of consecutive NEDC (New European Driving Cycle), repeated as long as the engine is not switched on by the default control strategy, namely the rule-based EMS. This test has been conducted on behalf of the industrial partner as a final step of the validation of the prototype vehicle [106]. As it can be deduced form the typology of the test, it is then focused on the validation of the electric propulsion only;

- on a rural road drive that consists of driving the prototype vehicle in conventional mode keeping the battery switched off for the validation of the conventional powertrain. This test has been conducted in the context of the presented research project and the acquired data have been recorder by means of commercial software which allowed to read messages of the CAN buses available on board.

The results of the validation are shown in Fig. 4.2 and Fig. 4.3, respectively. The ability to correctly match experimental data is demonstrated by the graphs, and it proves to be accurate enough for a control-oriented modeling approach.

4.2.4.2 Fuel consumption

The fuel consumption of the SiL-based vehicle model has been compared with experimental data acquired during a NEDC (New European Driving Cycle) performed in the context of the vehicle testing under the R101 EU Regulation, as well.

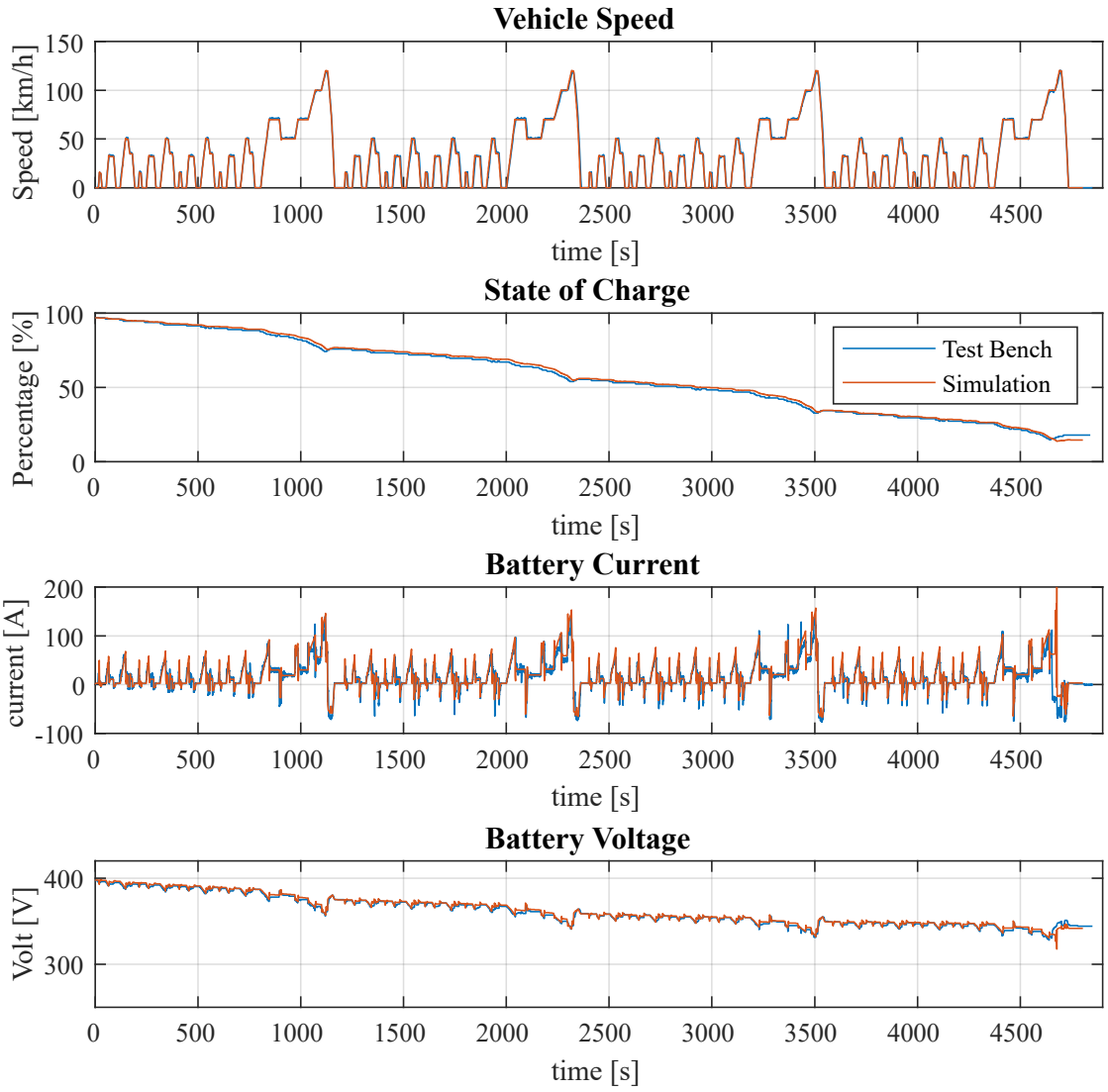

Figure 4.2: Vehicle model validation [100]. All-electric driving mode (AER test).

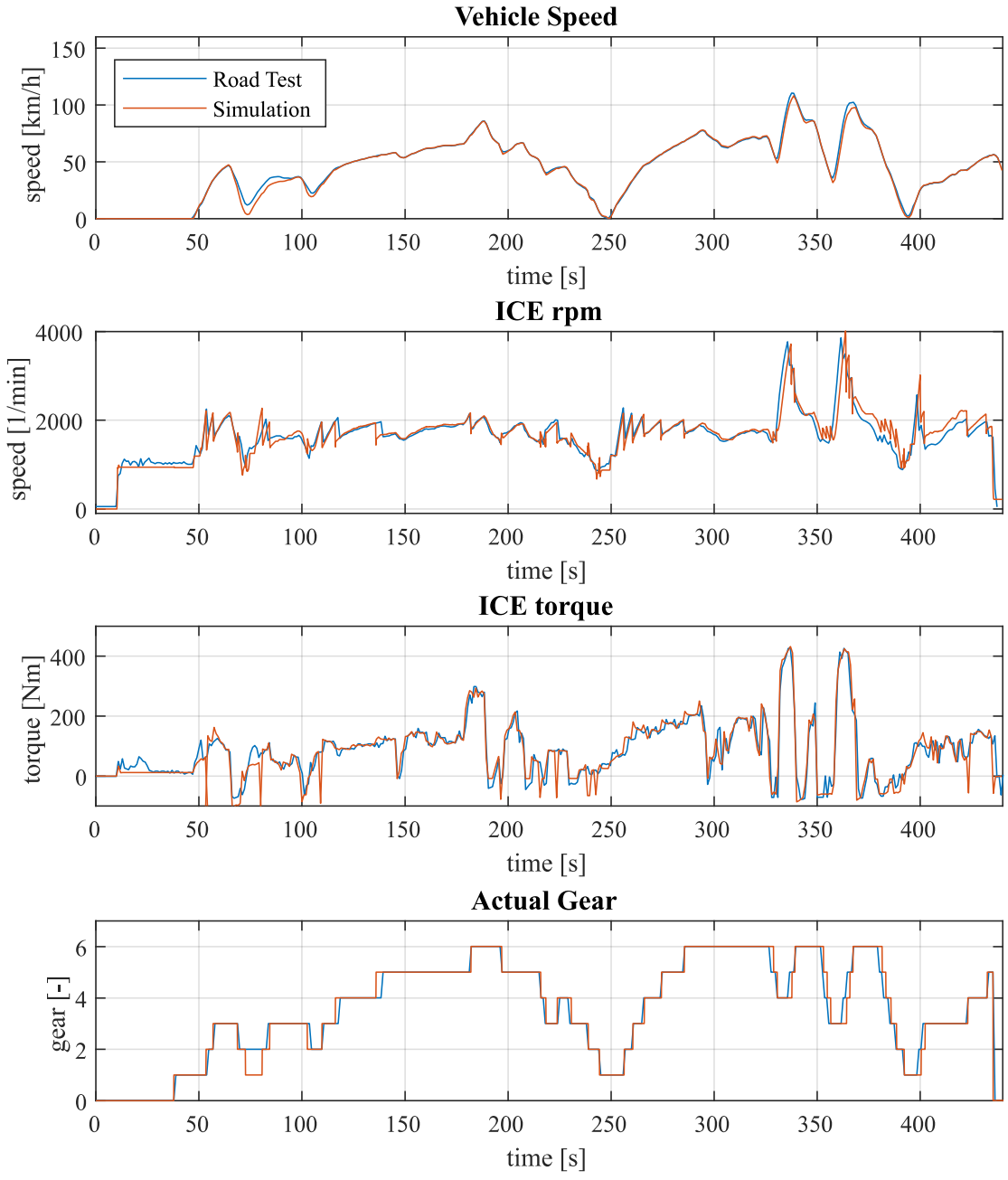

Figure 4.3: Vehicle model validation [100]. Conventional driving mode..

As it can be seen in Fig. 4.4, except for the slight difference on the gear-shifting strategy, it can be assumed that the SiL simulator is able to represent the real vehicle behavior with an acceptable accuracy since the overall difference in the fuel consumption is less than 3% between the simulated and measured data.

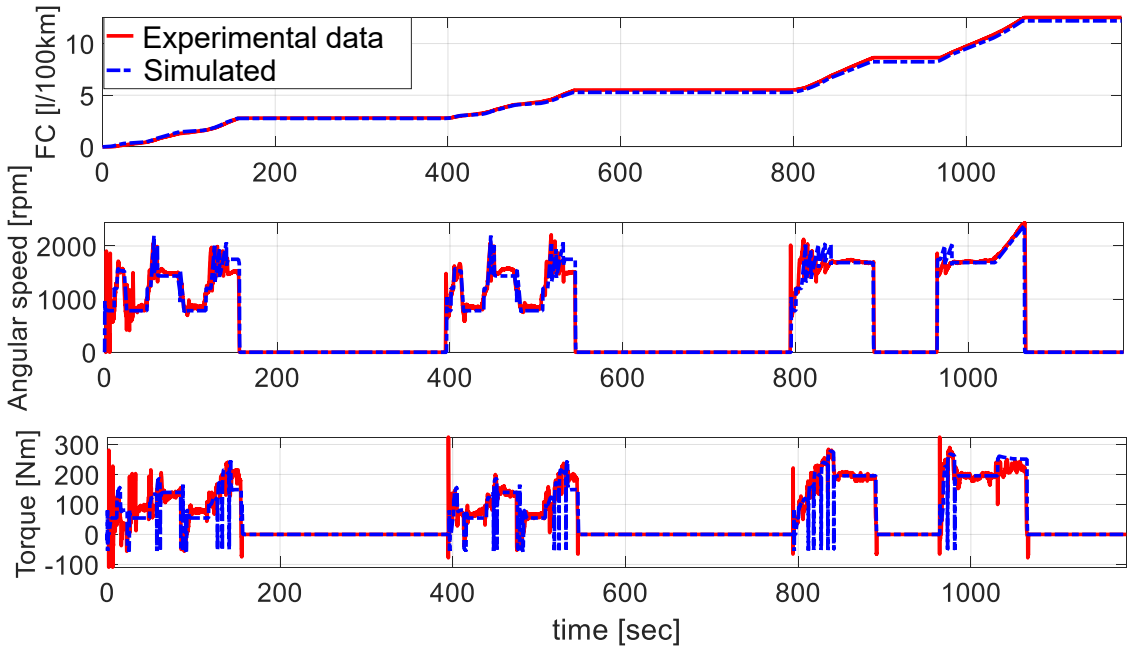

Figure 4.4: Fuel consumption validation [102].

4.3 Connected Hardware-in-the-Loop

4.3.1 Architecture

As further explained in [100], the architecture of the connected HiL (cHiL) developed during the research project is briefly described in the following paragraphs and its schematic representation is provided in Fig. 4.5.

In particular, the detailed vehicle model described in Section 4.2 is implemented on a Real-Time PC, which is connected to the rapid-prototyping HCU. The software of the supervisor controller has been deployed into a dedicated rapid prototyping control unit (dSPACE *MicroAutoBox II* [117]). Even in this case, the software is fully open to modifications and functions implementation. The

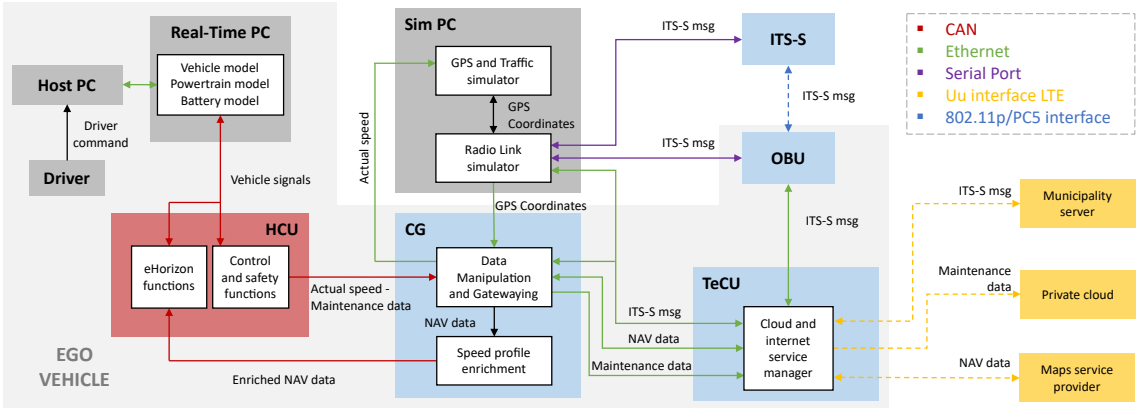

Figure 4.5: Connected HiL system representation [100].

software and the hardware are the exact replica of those mounted on the prototype, so the developed predictive functions can be seamlessly implemented on-board once validated at the HiL. Since it represents the hardware within the testing loop and so where the functions will be implemented, it is marked with the red block in Fig. 4.5.

Then, the HCU is connected to another rapid prototyping control unit that works as a Central Gateway (CG). Its main objective is preparing and forwarding all the eHorizon-related data to the HCU.

The V2X communication is handled by a Telecommunication Control Unit (TeCU) using the Multi Radio Access Technology (MultiRAT). The latter enables the data exchange with external real servers via Long Term Evolution (LTE) and with RoadSide Unit (RSU) using a commercial OBU (implementing ITS-G5 protocol stack). All the hardware within the light-grey box in Fig. 4.5, namely the HCU, the CG, the TeCU, and the OBU, will be installed in the vehicle.

Thus, it is possible to feed the HCU control functions with realistic data sent through a real communication protocol laying the ground for predictive strategies test and validation, with a focus on eHorizon predictive control strategies. In fact, they require an accurate representation of the surrounding environment for short- and long-term eHorizon reconstruction.

In the following sections, the main components of the connected-HiL system are briefly described.

4.3.2 Central Gateway

The Central Gateway (CG) collects, elaborates, and exchanges the data between each control unit, ensuring proper and effective communication. The selected hardware is MIRACLE^2 from AlmaAutomotive, which is a compact and fully programmable control unit suitable for rapid control prototyping and smart data acquisition [118].

Regarding the eHorizon functions validation, the CG has to provide the HCU with the prediction of the navigation data, listed in Tab. 4.1. To this aim, firstly the CG has to simulate the onboard navigator by forwarding the vehicle's actual position and the desired destination to the TeCU. The latter communicates with the map provider and sends back the navigation data to the CG as an XML file (the communication is described in Section 4.3.3).

Table 4.1: Navigation data.

No	Parameter	Unit	Size	Type
1	Route latitudes	deg	n+1	single
2	Route longitudes	deg	n+1	single
3	Route altitudes	m	n+1	uint16
4	Legal speed limits	m/s	n	uint8
5	Legal speed limits segments	m	n	uint16
6	ZEZ entrance/exit positions	m		uint16
7	Stop events classification	-	p	uint8
8	Traffic code classification	-	m	uint8
9	Stop events positions	m	p	uint16
10	Traffic codes segments	m	m	uint16

Then, the navigation data has to be enriched and forwarded to the HCU. To do so, the CG receives from the OBUs, through the TeCU:

- Cooperative Awareness Messages (CAM);
- Signal Phase and Timing (SPaT) messages;
- Decentralized Environmental Notification Messages (DENM);

that are standardized messages for the cooperative vehicular communication systems, as described in [119]. In this work, the CAM, SPaT, and DENM messages will include short horizon data such as the next traffic lights phases and timing or the presence of a moving vehicle approaching the same intersection of the ego vehicle.

Then, the CG performs the enrichment of the speed profile, that is mainly composed of two parts. In the first part, the static speed limits coming from the map provider is integrated with the stop events. In the second part, the updated speed profile is modified with the introduction of acceleration and deceleration phases. In parallel, accelerations that are not feasible for the ego vehicle are filtered. Finally, the CG sends such information to the HCU via CAN at the beginning of each trip and every time there is a request for a new or updated speed profile, using the existing communication layout of the prototype vehicle.

4.3.3 Telecommunication Control Unit

In the considered architecture, the role of handling the diverse Radio Access Technologies is taken over by a single board computer. The latter is capable of exchanging data using the different protocols enabling the typical V2X connections.

The update frequency depends on the type of application. In the considered case, the shorter the eHorizon the smaller the update frequency in terms of time intervals. In some cases, it is not possible to determine this parameter because it can be very high or very low depending on unpredictable situations like in the case the driver takes the wrong direction and the navigation data must be updated.

The estimation of the payload size for the long horizon has been obtained considering the size of files typically used for navigation data, such as KML, XML, JSON files. The short horizon data have a payload size in the same range of CAM, DENM, SPaT messages which can be about 200-400 bytes. The required throughput has been estimated exploiting update frequency and payload size. Thanks to such estimation, each message, and therefore each link, is associated with a V2X connection. Each server is interrogated to retrieve the information needed for enabling the eHorizon functionalities. In particular, communication is

established with:

- Map Service Provider
  it provides the route to follow, the speed limits, and the slope profile along that route. Other information given by the map provider is the ZEZ topological limits;

- Private Server
  it is specific for in-cloud functions implementation.

Then, the relative protocol stack has been defined for each message type. For this analysis, only technologies available on the market have been considered (e.g., 5G-NR is not considered yet). The LTE is a long-range radio access technology with relatively low latency, useful, for in-vehicle implementation, to communicate with diverse internet services. LTE-V2X refers to the device-to-device version of the LTE (Mode 4) used for vehicular communication. It uses the PC5 air interface, while LTE indicates the use of the Uu air interface (Mode 3).

The system known as ETSI ITS-G5 was developed by the ITS technical committee referring to the previous US project, the Wireless Access in Vehicular Environments (WAVE). The WAVE project defined the changes to the IEEE 802.11 standard (the one behind the Wi-Fi products) to support the requirements of vehicle transport systems, producing the so-called IEEE 802.11p version.

Therefore, a single-board computer has been selected to implement the TeCU. This control unit constitutes a multi-RAT technology: it works as a router for the In-Vehicle Network (IVN) and it also provides some grade of automation at the application layer. The hardware used is *APU3C4* from PC Engines™ [120], which mounts a Linux-based operating system and its functionalities have been implemented with Python. At the IVN side, it is connected via ethernet to the CG, it uses TCP/IP and UDP/IP at the transport layer, and SFTP for file exchange. On the external network side, it exploits an LTE UE for internet access, it uses Message Queue Telemetry Transport (MQTT), and a custom TCP/IP based protocols for data exchange with internet services. For short-range communications, it is connected via serial port to an OBU equipped with ITS-G5 stack, so that all the ITS information is passed to the IVN through the TeCU.

4.3.4 Long-term eHorizon data flow testing

In order to test the end-to-end communication between the aforementioned components, the communication to the HCU of the enriched navigation data is taken into account since these data are necessary for the validation of predictive control strategies.

The eHorizon control functions require the prediction of the navigation data to be as accurate as possible. So, as shown in Fig. 4.6, the CG performs the enrichment of the static navigation data (legal speed limits, slope, stop events and ZEZ topological information). Then, the CG receives short-range eHorizon data, as well. Finally, the CG forwards the prediction to the HCU where the eHorizon control strategies will receive it as if the vehicle were on the real road.

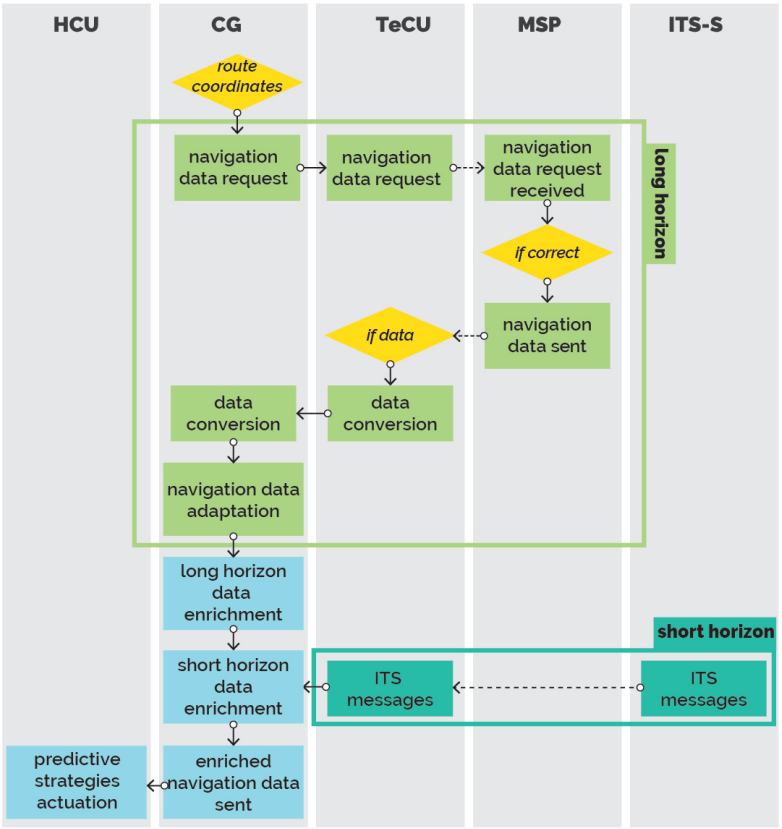

Figure 4.6: Short and long eHorizon data flowchart [100].

Following the light green boxes in Fig. 4.6, the driver sets the desired destination (point B in Fig. 4.7) into the CG that has an integrated Human-Machine Interface (HMI). Then, the CG combines it with the actual vehicle position, shown as point A in Fig. 4.7, and it sends them via the internal vehicle network to the TeCU along with the request of the navigation data prediction. The TeCU elaborates the request and publishes it on the remote server (Map Service Provider) using the MQTT protocol. The MSP checks if the received coordinates represent a plausible vehicle's position, e.g., if the vehicle position is within a building or outside the road. Again via MQTT, the MSP sends the prediction of the navigation data back to the TeCU (the orange line in Fig. 4.8, named "raw data").

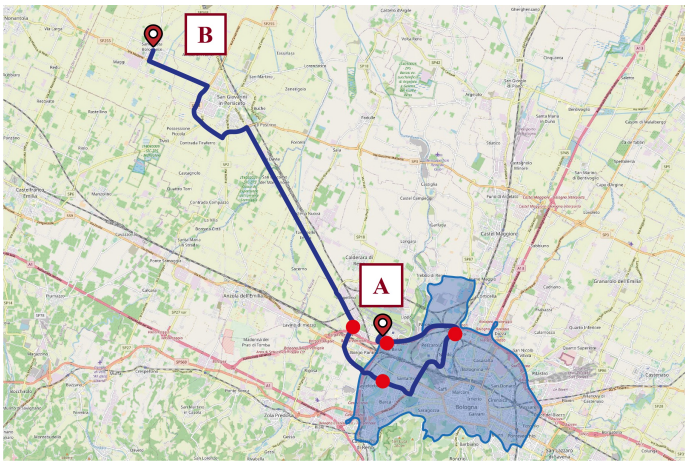

Figure 4.7: Route representation with stop events (red dots) [100].

Finally, the prediction is forwarded to the CG that performs the enrichment, using the information about stop events, decelerations, and accelerations. In particular, the CG:

1. searches for and erases unplausible discontinuities in the speed limits, (the orange spikes depicted in the bottom right chart in Fig. 4.8) from the prediction. These discontinuities are due to driving through roads with different speed limits, but where it would be either impossible or illogical to accelerate the vehicle to reach the limit and then immediately decelerate;

2. enriches the speed profile with the information about the static stop events (red points in Fig. 4.7, Fig. 4.8). The stop events include traffic lights, rights of

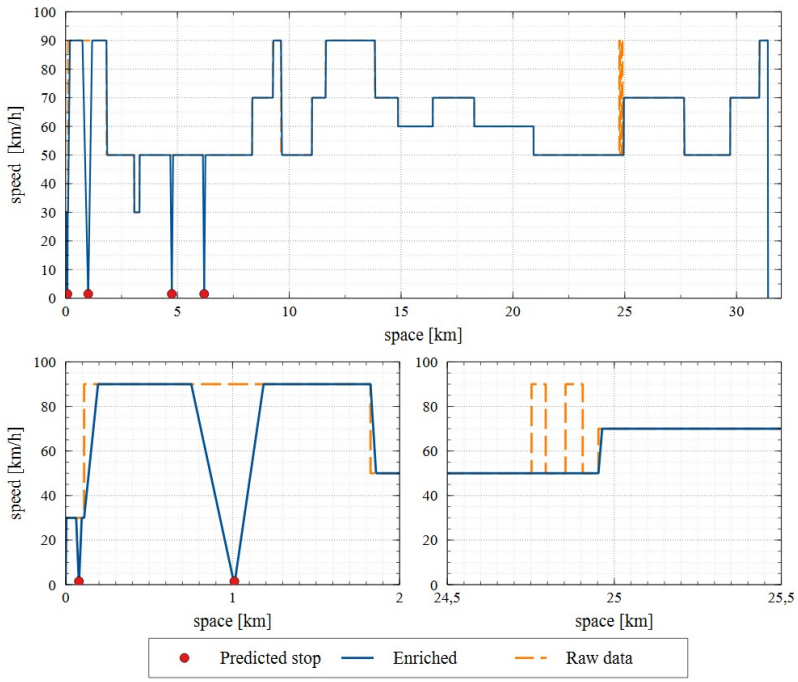

Figure 4.8: Speed profile received and enriched [100].

way, and roundabouts. For the sake of clarity, the stop events here presented have been added manually with the aim of explaining the workflow of the system ;

3. modifies the speed profile with realistic constant values of accelerations and decelerations, as shown in the bottom left chart of Fig. 4.8, in order to handle the stop events and the discontinuities between different legal speed limits. The developed speed profile simulator, described in Section 5.2, will take as input the enriched speed profile in order to predict an energy-equivalent speed trace over the given route.

Then, the navigation data received in the HCU from the map service provider through V2N connectivity are used to reconstruct the electronic horizon of the vehicle in order to apply the predictive strategies for the estimation of future working conditions of the powertrain, as discussed in the next chapter. Moreover, in Chapter 6 the implementation of one of the developed control strategies is discussed, and the introduced workflow for long-term eHorizon function testing

will be shown, as well, with real-time up-to-date navigation data.

Chapter 5

Predictive control strategies for hybrid electric vehicles

In this chapter the developed control strategies during the research project are presented. In particular, a Discrete Dynamic Programming algorithm and an Adpative-ECMS are discussed. The former takes into account both energy and battery thermal management for the optimization, while the latter relies on the prediction of the powertrain working conditions to handle zero-emission zones in pure-electric driving mode.

5.1 Standard on-board strategies

The baseline, default strategies for energy and battery thermal management are presented in this section. They have been calibrated, tested and implemented in the HCU by the industrial partner, which then represents the software developer of the entire supervisory controller. Then, the modified energy management RBS for zero-emission zones handling is introduced, as well.

5.1.1 Rule-Based Strategy for energy management

As previously explained, this heuristic energy management strategy is aimed at evaluating the torque split factor between the conventional and the electric powertrain. It is defined by rules relying on fixed thresholds for different vehicular

parameters, such as wheel torque request, battery state of charge and vehicle speed.

In particular, if a negative torque is requested by the driver, a regenerative braking occurs and the battery is recharged by the electric motors (i.e., P4), acting as generators.

On the other hand, during traction, that is when the driver torque request is positive, the energy management of the powertrain is performed by a rule-based strategy (RBS) for energy management, which evaluates the torque split between the ICE and the EMs. This strategy is based on rules depending on fixed thresholds (which have been previously calibrated). In addition to the driver torque request, parameters such as the vehicle speed and the state of charge of the battery are involved in the torque split factor evaluation. Thus, the controller firstly discharges the battery and then keeps the state of charge around the chosen threshold. Such an approach is commonly referred to as the charge-depleting/charge-sustaining approach and is typically used for PHEVs, like the one used for this activity.

Since this kind of control logic is reliable and easily real-time implementable due to the low computational burden required [33, 46, 56], it is currently the on-board standard strategy. It has been calibrated in previous activities by the industrial partner. Although there are no data available regarding these processes, the reliability and the robustness of the rule-based energy management strategy are proven by the numerous HiL and on-road tests performed on the HCU as well as on the whole vehicle. Further details can be found in [106].

5.1.2 Modified Rule-Based Strategy for Zero-Emission Zones

As further discussed in [98], the standard rule-based strategy has been modified in the context of the research project to guarantee the target value of SoC at ZEZ entrance, allowing the all-electric driving in the urban area even with the conventional control policy. To this end, the thresholds of the rule regarding the SoC have been modified according to the Eq. (5.1):

$$\xi_{\min} = \begin{cases} \xi_{\min,el}, & \text{no ZEZ} \\ \xi_t, & \text{ZEZ} \end{cases}$$
$$\xi_{\max} = \begin{cases} \xi_{\max,el}, & \text{no ZEZ} \\ \xi_t + \Delta\xi_{el}, & \text{ZEZ} \end{cases} \tag{5.1}$$

where $\xi_{\min,el}, \xi_{\max,el}$ are the minimum and maximum values of SoC thresholds for charge-sustaining (CS) mode and whose difference is $\Delta\xi_{el} = \xi_{max,el} - \xi_{min,el} = 5\%$, and ξ_t is the target SoC at ZEZ entrance (whose calculation is one of the topics of this paper, as explained in the following paragraphs).

The working principle is the same for both the operating modes, as shown in Fig. 5.1, that is achieving charge sustaining in the SoC range defined by the values of Eq. (5.1). Thus, if $\xi(t) < \xi_{\min}$, then electric driving is no more allowed and the battery is recharged by means of the ISG absorbing an additional amount of torque provided by the ICE (load-point shifting strategy). During recharging, if $\xi(t) \geq \xi_{\max}$, then the battery is considered charged enough for eDrive mode (which will be applied only if all the other conditions imposed by the RBS are analogously satisfied). Therefore, except for the SoC thresholds, the main difference is that the conventional RBS will always perform a Charge Depleting - Charge Sustaining (CD-CS) mode, while the modified one will perform a Charge Increasing - Charge Sustaining (CI/CS) mode if $\xi(0) < \xi_t$, being $\xi(0)$ the SoC value at the beginning of the driving mission.

5.1.3 Rule-Based Strategy for battery thermal management

The heuristic thermal management control strategy, developed by the industrial partner, as well, is based on intuitive rules and correlations involving various parameters, mainly temperatures. One guiding principle of such a strategy is to preserve the temperature of thermal-stressed components within a restricted range of fixed values. Therefore, upper and lower temperature thresholds are set after a calibration phase, which can turn out to be an expensive and time-consuming task because the choice of the optimal values is influenced by the

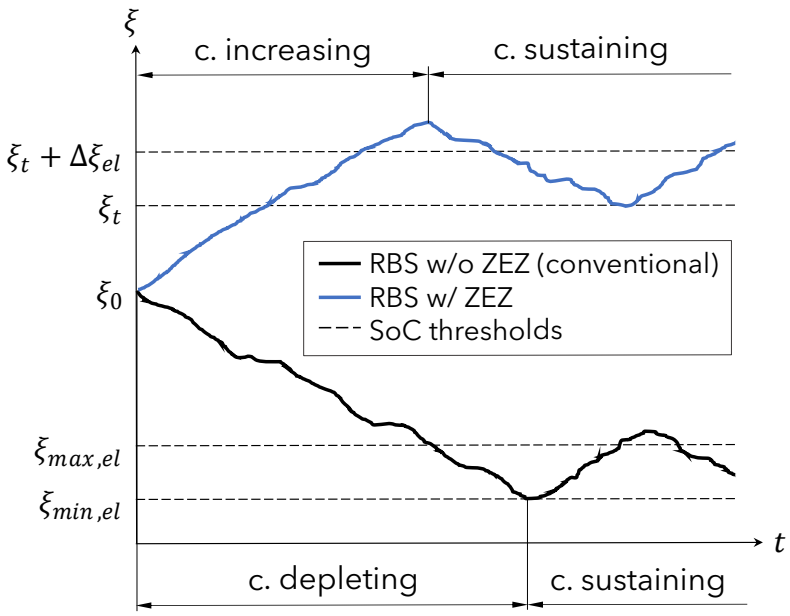

Figure 5.1: Working modes of the Rule-Based Strategy [98].

architecture of the examined cooling system.

Moreover, in order to avoid performance de-rating and especially premature aging of the component, the physical constraint represented by the upper limit of the battery operating temperature range has been considered, as well. In this case, the thermal characterization of the battery under study led to set the upper thermal limit $\vartheta_{b,lim} = 40°C$, as suggested by the battery manufacturer. As a consequence, because of the standard strategy relies on fixed threshold values, the latter are usually lower than the one related to the aforementioned thermal constraint because highly demanding future working conditions have to be taken into account in advance by setting a high safety margin.

In Fig. 5.2 the working principle of the rule-based control strategy applied to the electrical pump of the battery cooling circuit is shown.

As it can be seen, battery cooling is either requested or not when the battery temperature is either higher or lower than the threshold values, which are respectively $T_{cool,ON} = 30°C$, $T_{cool,OFF} = 28°C$.

Analogous considerations previously made for the calibration and the validation of the rule-based energy management strategy can be applied even in this

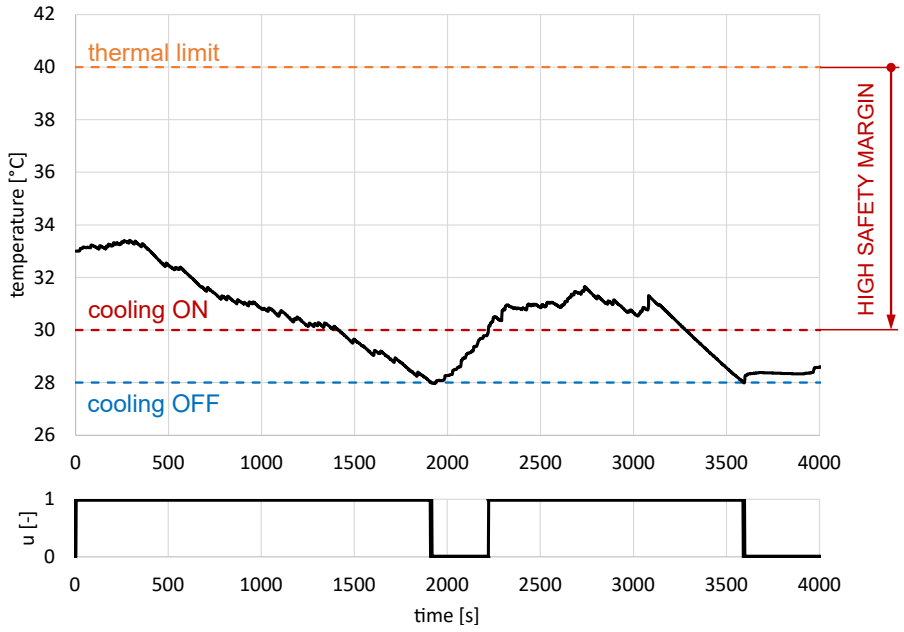

Figure 5.2: Working mode of the Rule-Based Strategy for battery thermal management.

case, as well.

5.2 Architecture of the predictive functions

The developed Predictive Functions (PF) have been implemented within the HCU according to the high-level architecture depicted in Fig. 5.3. The used nomenclatures are: speed profile predictor (SPP), driver model (DRV), space-to-time (S2T) conversion, backward vehicle model (BVM), wheels (W), motors (M), battery (B), limits (L), energy management strategies (EMS), reference SoC (REF) evaluation, equivalence factor (EF) evaluation, charge-sustaining (CS) SoC thresholds evaluation. The activation of the A-ECMS can be triggered by the b_{ECMS} signal.

In order to predict the behavior of the battery SoC over a given urban electronic horizon, the so-called eHorizon, which is a reconstruction of the future conditions of the vehicle on the road ahead, the ZEZ algorithm relies on a backward-facing vehicle model (BVM), which consequently considers only the electric powertrain (P4 and battery). Both these functions, the BVM and the ZEZ, together with the SPP, represent the part of the HCU software in charge of the predictive tasks. It

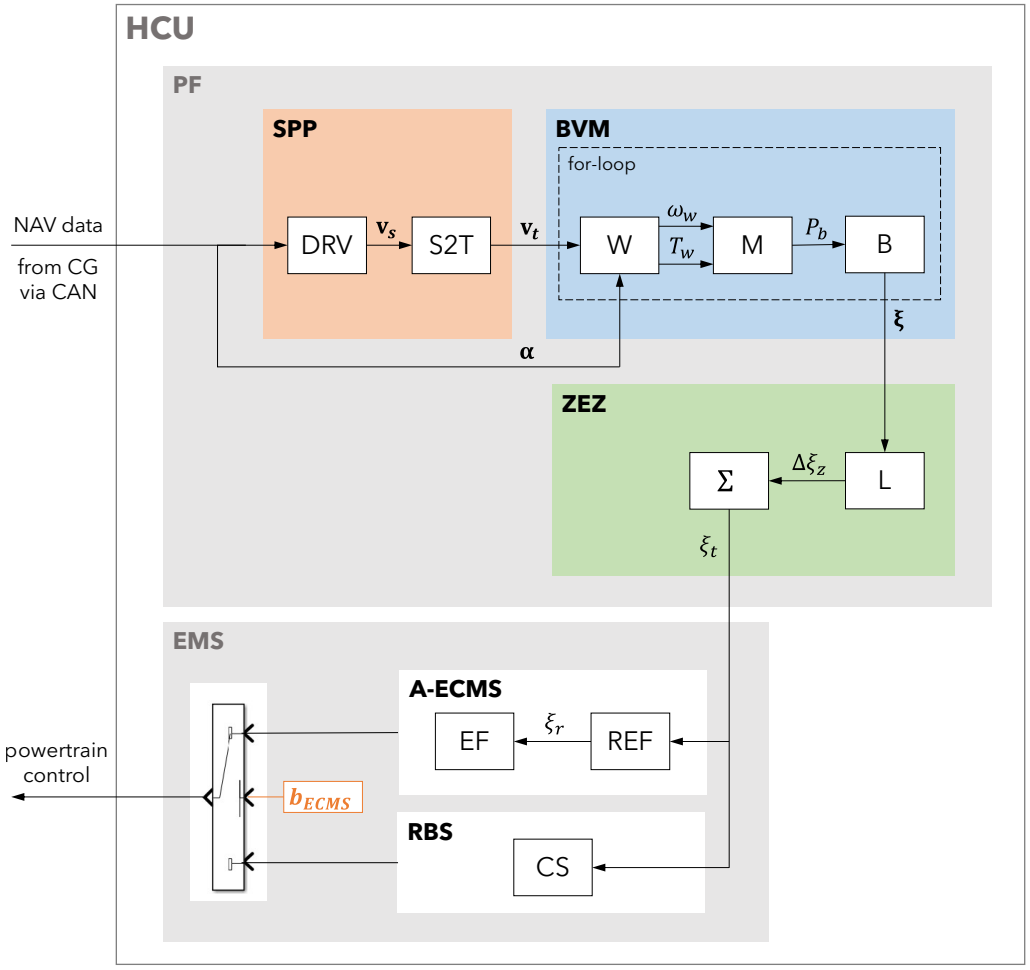

Figure 5.3: Working flow of the predictive functions for target SoC evaluation as implemented in the supervisory controller software.

then takes into account the following parameters:

- *input parameter(s)*
  navigation data from for the evaluation of vectors representing the vehicle speed profile, $\mathbf{v}$, predicted as in Section 5.3, the road slope profile, $\boldsymbol{\alpha}$, and topological information regarding the zero-emission zone (distances from city entrance and exit);

- *output parameter(s)*
  target state of charge at ZEZ entrance, ξ_t, evaluated by the ZEZ function (Section 5.5);

- *state variable(s)*
  state of charge, ξ, and temperature, ϑ, of the battery, predicted over the given urban horizon by the BVM (Section 5.4).

5.3 Speed profile prediction

A speed profile prediction (SPP) algorithm has been developed in Simulink environment by means of Stateflow with the main objective of generating a realistic speed trace on the basis of navigation data. It has been calibrated and validated over experimental data acquired on board.

A detailed explanation of the work conducted for the development of the algorithm is given in [121].

5.3.1 Architecture

After reconstructing the electronic horizon by gathering all the messages sent to the HCU via CAN regarding the navigation data, the eHorizon is enriched with a prediction of a space-based speed profile on the basis of routing information.

In particular, the algorithm relies on the following input data:

- legal speed limits
  they are assumed to be boundary thresholds for the maximum allowable speed (MAS) of the vehicle. A legal speed limit can be considered as an *extensive* property of a route because its validity extends over space for a certain road segment, whose length is provided within navigation data by the maps service provider;

- traffic density
  it affects the MAS, as well, and also how it is followed by the driver. The traffic density along a certain road segment can be quantified using either colors or labels, or codes. The former is the case of MPSs, which treat a no traffic road segment as "green" or "empty", while the latter is the convention adopted in this work, as shown in Tab. 5.1;

- stop events
  they inherently represent a *local* property of a route, meaning that they are located in a specific position. Speed profiles are characterized by subsequent deceleration-acceleration phases in correspondence of stop events, thus affecting the vehicle power distribution and the energy management. Since not all the stop events require always such maneuvers, like traffic lights or roundabouts (intended as right-of-way), a *stop-over probability* for each of these *dynamic* stops has been defined and correlated to the traffic density on the given road segment at the end of which the stop event is located (Tab. 5.1);

- driver behavior
  energy consumption related to a given route can be largely influenced by driver's behavior because it can affect the intensity of acceleration and deceleration phases and the maximum allowable speed.

Table 5.1: Traffic density convention and stop-over probability.

Traffic color	Traffic label	Traffic code	Green light probability [%]
●	Free	1	80
●	Slow	2	60
●	Heavy/queueing	3	35
●	Stationary	4	20

5.3.2 Algorithm

The main objective of the algorithm is to generate a space-based speed vector, with the assumption of traveling time minimization. This means that the driver will always try to reach the MAS, if possible.

1. space discretization
   A space vector is created by intersection of all the segment and position vectors of the input navigation data. In this way, the vector is represented by N segments whose endpoints are called *nodes*. Nodes are points where

boundary conditions are imposed, since they represent coordinates where changes in traffic code and/or speed limit take place, or where the stop events are located. Then, another subdivision is made for each segment, and the resulting N points are used to evaluate the speed of the ego-vehicle;

2. legal speed limit and traffic code assignment
   The starting values of speed limit and traffic code are allocated within the new space vector, i.e. for every sub-segment $i = 1,...,N$ of each segment $j = 1,...,N_s$;

3. next-point MAS evaluation
   prior to speed evaluation, the MAS needs to be calculated. If a node coincides with a stop event location, then the MAS at that node, MAS_i, is imposed to be null (in case of a full stop) or equal to a constant value (bump, right of way). Otherwise, for the remaining nodes, the MAS is evaluated as a function of the traffic density. The latter affects the MAS in two different ways. The first effect is the reduction of the maximum speed which results lower than the legal speed limit due to the presence of other cars, limiting the ego-vehicle speed. The second effect is the oscillation around that constant speed due to variable traffic flow. As proposed by [34], with regards to the next point $i + 1$, the MAS can be calculated as:

$$MAS = MAS_r + MAS_n \tag{5.2}$$

   where the reference MAS, accounting for the reduction effect due to traffic density, and the noise-related MAS, accounting for the oscillatory effect due to traffic density around MAS_r, are, respectively:

$$MAS_r = V_{lim,i+1} \cdot CW_{i+1} \tag{5.3}$$

$$MAS_n = \sum_{h=1}^{H} A_h \cdot \cos(2\pi f_h x) \tag{5.4}$$

   being:

CW_{i+1} : code weight, depending on the traffic code;
$V_{lim,i+1}$: legal speed limit;
A_h, f_h : amplitude and frequency of the oscillation;
$H = 4$ is the number of the considered harmonics to properly describe the oscillatory phenomenon.

The parameters CW_{i+1} and A_h, f_h will be explained in Section 5.3.3;

4. next-point speed evaluation
   At this point, the next-point speed V_{i+1} can be evaluated according to the following conditions:

   - $V_i = MAS$
     The driver decides whether to keep the speed constant or to start braking in order to match a lower speed imposed by the closest stop event or speed limit change;
   - $V_i < MAS$
     The driver considers to accelerate to reach MAS. With this aim, two parameters are evaluated regarding the next point $i + 1$: the speed V due to vehicle acceleration and the the maximum speed Q that still allows the driver to brake in time to match the speed imposed by the next stop event or speed limit change. For this reason, an exponential acceleration and a linear deceleration law are adopted:

$$a_a(x) = k_a \; a_{a,\max} \cdot (1 - e^{-\tau x}) \tag{5.5}$$

$$a_d(x) = -k_d \; a_{d,\max} \cdot x \tag{5.6}$$

     with:

$a_{a,\max}$, $a_{d,\max}$: maximum acceleration and deceleration, respectively, depending on vehicle performance;
k_a, k_d : reductive factors of the maximum acceleration and deceleration, respectively, depending on driver behavior;
τ : time constant defining the acceleration transient.

Thus, as shown in Fig. 5.4, the next-point speed V_{i+1} is calculated as the result of the following conditions:

(a) $(V \leq Q)$ & $(V \leq MAS) \Rightarrow V_{i+1} = V$

(b) $(V \leq Q)$ & $(V \geq MAS) \Rightarrow V_{i+1} = MAS$

(c) $(V \geq Q)$ & $(V \leq MAS) \Rightarrow V_{i+1} = Q$

5. for-loop repetition for each point of the i-th sub-segment
   Repeat steps (3) to (4), for $i = 1,\ldots,N$

6. speed and space assignment for vector generation
   At the end of each nested loop involving sub-segments, the calculated vehicle speed and space are assigned to the related vectors

7. for-loop repetition for each point of the j-th segment
   Repeat steps (3) to (6), for $j = 1,\ldots,N_s$

8. space-to-time conversion
   In order to feed the backward vehicle model with proper input signals, the speed profile is converted from space to time domain by following a linear interpolation of the values. in other words, in addition to a speed and a space vector, a time vector is generated, as well. In particular, a stop time is assigned every time the vehicle speed is null.

5.3.3 Calibration methodology and procedure

In this section, the parameters listed in Tab. 5.2 are calibrated in different scenarios. As it can be noticed, they are mainly influenced by the driver behavior and the traffic density, which strongly affect the speed trace and the related vehicle energy consumption.

5.3.3.1 Key performance indicators

In order to evaluate the overall goodness of predictions as well as the way they are affected by single parameters, several key performance indicators (KPI) have been defined.

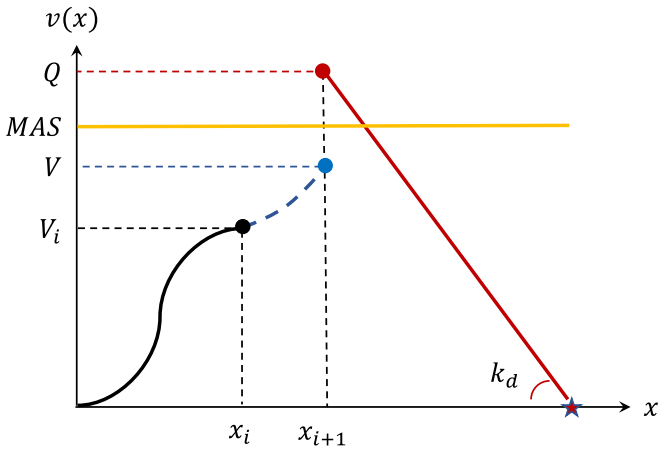

(a) $V_{i+1} = V$.

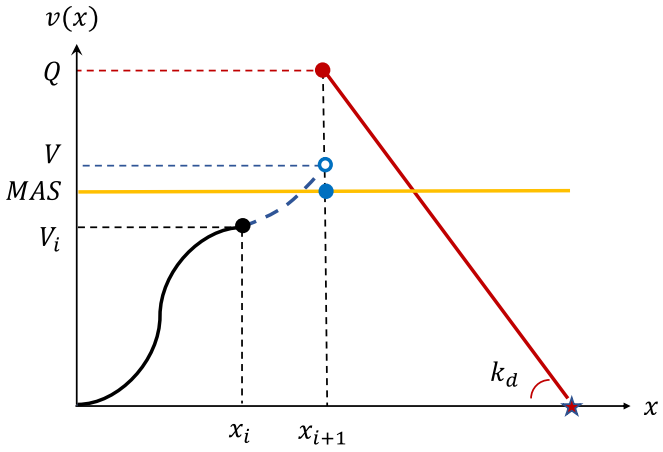

(b) $V_{i+1} = MAS$.

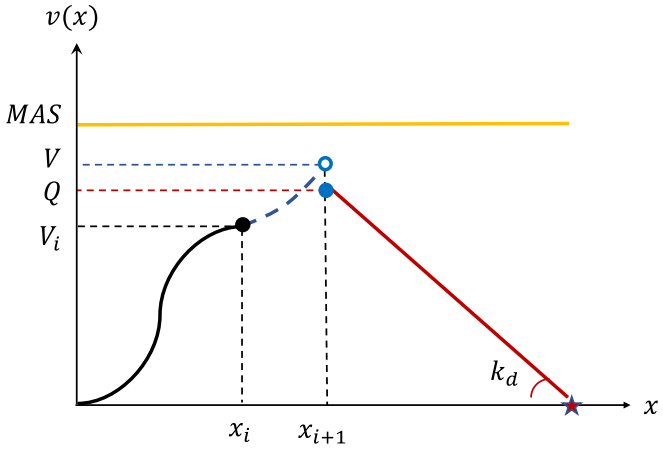

(c) $V_{i+1} = Q$.

Figure 5.4: Next-point speed evaluation [121].

Table 5.2: Calibration parameters of the speed profile predictor.

Parameters	Related to	Affected by
k_a, τ	acceleration law, $a_a(x)$	driver behavior
k_d	deceleration law, $a_d(x)$	driver behavior
CW	reference MAS, MAS_r	traffic density
A_h, f_h	oscillating MAS, $MAS_n(x)$	traffic density

To this aim, two classes of indicators have been introduced: *speed-based* and *energy-based* KPIs. The latter are important because the main objective of the predictive algorithm is to generate speed traces as close as possible to real ones from an energy consumption point of view. This is crucial for achieving high accuracy in battery state of charge prediction, as will be discussed in Section 5.4. Nevertheless, since the output of the predictive algorithm is a speed profile, an evaluation of the error in terms of speed is necessary.

Regarding speed-based KPIs, reliable parameters for speed traces comparison are provided by [122, 123] and they can be represented by the *mean absolute error* (MAE) and the *BIAS* , both expressed in [km/h] and defined as:

$$MAE = \frac{1}{n}\sum_{i=1}^{n}\left|S_{p,i} - S_{r,i}\right| \tag{5.7}$$

$$BIAS = \frac{1}{n}\sum_{i=1}^{n}\left(S_{p,i} - S_{r,i}\right) \tag{5.8}$$

where $S_{p,i}$ and $S_{r,i}$ are respectively the predicted and the measured speed at point i and n is the total amount of points where the differences are calculated. The MAE provides a measure of the average magnitude of the errors, while the BIAS, considering the sign of the difference, is useful to identify eventual issues related to a systematic under/overestimation of the predicted speed.

Energy-based KPIs suggested by SAE [124] have been assumed as reference. In this document, these metrics are defined to evaluate the goodness of tests where a reference cycle must be followed by a human operator acting manually on pedals. First of all, three force components are calculated for both the predicted and the

measured cycle:

- Road load
  analogously to Eq. (3.3), it represents the force required to win rolling resistance and drag force:
  $$F_{RL} = f_0 + f_1 \cdot v + f_2 \cdot v^2 \tag{5.9}$$

- Positive inertial force
  it is associated only to positive values of acceleration (a^+) and represents the force required by the vehicle of mass m to be accelerated:
  $$F_{I^+} = m_v \cdot a^+ \tag{5.10}$$

- Negative inertial force
  it is associated only to negative values of acceleration (a^-) and represents the force required to decelerate the vehicle:
  $$F_{I^-} = m_v \cdot a^- \tag{5.11}$$

Once the three forces have been defined, the relative energies can be retrieved by integrating the forces along the path length L, obtaining:

$$E_{RL} = \int_0^L F_{RL} dl \tag{5.12}$$

$$E_{I^+} = \int_0^L F_{I^+} dl \tag{5.13}$$

$$E_{I^-} = \int_0^L F_{I^-} dl \tag{5.14}$$

Now, three energy KPI can be introduced in form of energy rate, where subscripts p and r are respectively referred to the predicted and real (measured) speed profile:

$$\Delta E_{RL} = \frac{E_{RL_p} - E_{RL_r}}{E_{RL_r}} \cdot 100 \tag{5.15}$$

$$\Delta E_{I^+} = \frac{E_{I_p^+} - E_{I_r^+}}{E_{I_r^+}} \cdot 100 \tag{5.16}$$

$$\Delta E_{I^-} = \frac{E_{I_p^-} - E_{I_r^-}}{E_{I_r^-}} \cdot 100 \tag{5.17}$$

While differences in the negative inertial energy could be neglected in case of a conventional vehicle, they have a huge impact in case of HEVs since they represent the amount of energy that can be potentially restored while braking.

5.3.3.2 Driver-related parameters

The parameters depending on the driver behavior are here calibrated.

Since they affect the acceleration and deceleration phases, described by Eq. (5.5) and Eq. (5.6), respectively, the conceived scenario is represented by a ramp-up ramp-down cycle with a nominal speed of 50 km/h and performed on a straight road. The speed set-point has been chosen considering that the predicted speed profile will be used for battery SoC prediction over a urban area.

The optimal values of τ, k_a, k_d, led to the minimum value $MAE = 2.4$ km/h. In Fig. 5.5 the comparison between the measured and the predicted speed trace for the optimal values of the calibration parameters is shown.

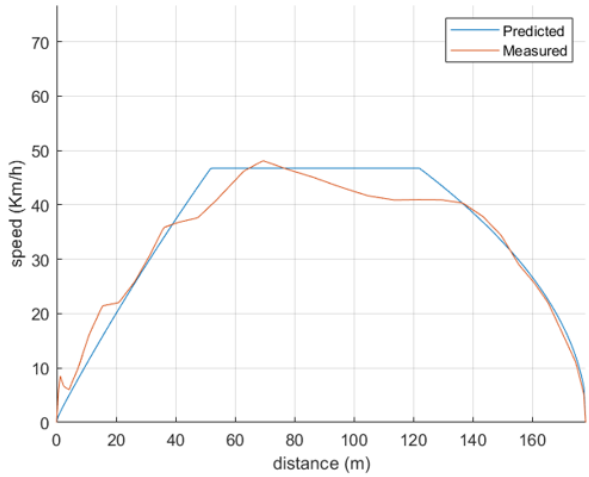

Figure 5.5: Driver-related parameters calibration [121]. Ramp test.

5.3.3.3 Traffic-related parameters

In order to calibrate traffic-related parameters, a scenario characterized by different speed limits and traffic densities has been conceived. In particular, a urban route within the Bologna city center has been defined to include as many different speed limits as possible for an effective calibration of the oscillating MAS.

With this aim, the speed trace measured during the road test has been sectioned by traffic codes, and the resulting portions have been gathered together. Then, four traffic-based clusters of measured speed sections are obtained. At this point, the Fast Fourier Transform (FFT) has been applied to every speed signal of each cluster. A magnitude-frequency diagram is then obtained, as shown in Fig. 5.6 for the cluster characterized by the orange traffic color (i.e. traffic code equal to $c = 2$).

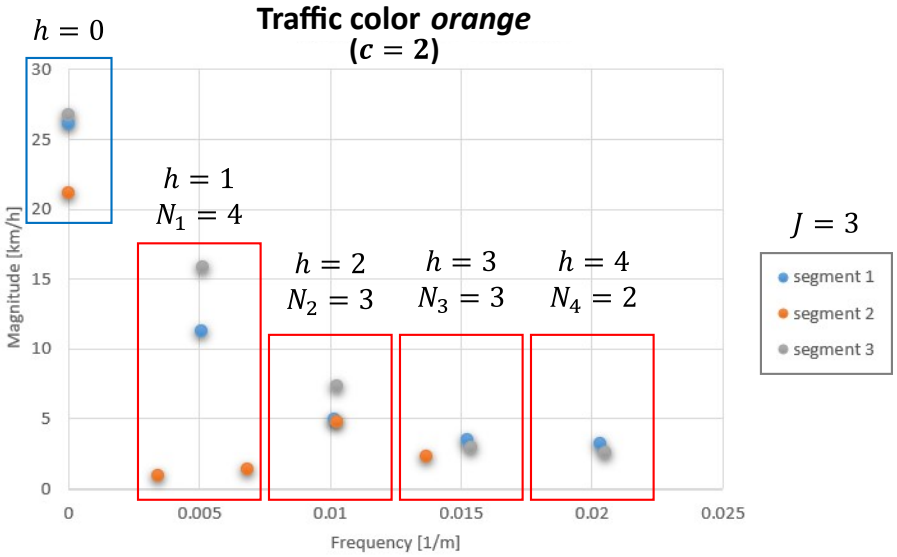

Figure 5.6: Measured speed frequency analysis with FFT for a given traffic code [121].

In this case, $J = 3$ speed signals have been collected, being each of them related to a certain space segmentation of length l_j. Moreover, as previously introduced, it can be noticed that only the first $H = 4$ dominant harmonics (red boxes) have been taken into account to describe the oscillatory phenomenon with an acceptable accuracy. Considering the h-th harmonic, different numbers N_h of magnitudes can be observed, although one magnitude for each speed signal would be expected ($N_h = J = 3$, $\forall h = 1,\ldots,4$). For the first one ($h = 1$), the speed trace (segment) $j = 2$

presents two different magnitudes (orange dots) because the need to determine dominant frequencies f_h led to group them together. As a result, this yields to $N_1 = 4 > 3 = J$. On the other hand, for the fourth harmonic and frequency ($h = 4$), no appreciable magnitude has been individuated for the same speed signal, and hence $N_4 = 2 < 3 = J$.

At this point, with regards to the dynamic term of the MAS (Eq. (5.4)), amplitudes and frequencies can be determined for a given traffic code in order to define the harmonic behavior of the oscillation. These parameters can be both expressed as arithmetic means of the relative measured values, weighted for the segment length l_j, as well. In formulas:

$$A_{c,h} = \frac{\sum_{j=1}^{J} \left(1/N_h \cdot \sum_{n=1}^{N_h} A_{n,h,j}\right) \cdot l_j}{\sum_{j=1}^{J} l_j} \tag{5.18}$$

$$f_{c,h} = \frac{\sum_{j=1}^{J} \left(1/N_h \cdot \sum_{n=1}^{N_h} f_{n,h,j}\right) \cdot l_j}{\sum_{j=1}^{J} l_j} \tag{5.19}$$

where N_h is the number of magnitudes $A_{n,h,j}$ and $f_{n,h,j}$ frequencies corresponding to the h-th harmonic of the j-th signal.

Moreover, since the amplitude A_0 of the oscillation at $f = 0\,\mathrm{m}^{-1}$ (space domain) represents the average speed along the given segments, it can be used to determine the parameter CW for each traffic code. In particular, since it is aimed to reduce the maximum speed, namely the legal speed limit, due to traffic density, it may be calculated as the ratio between the base oscillation amplitude A_0 and the speed limit V_{lim}, weighted for the length l of each segment (spatial dependency). In formula, the reduction factor CW for the traffic code c can be calculated as:

$$CW_c = \frac{\sum_{j=1}^{J} A_{0,j}/V_{lim,j} \cdot l_j}{\sum_{j=1}^{J} l_j} \tag{5.20}$$

being $V_{lim,j}$ the legal speed limit for the j-th segment. In this way, according to Eq. (5.3), it is possible to evaluate the static contribution to the MAS.

5.3.4 Validation

In order to validate and analyze the energetic performance of the speed profile predictor, several test cases have been conceived in a way that the algorithm could be tested with different traffic densities and legal speed limits. With this aim, similarly to the calibration procedure, the test cases are represented by different trips within the urban area of Bologna, with different travel distances and performed at different times of the day. In Fig. 5.7 the trip chosen for one of the test cases is depicted.

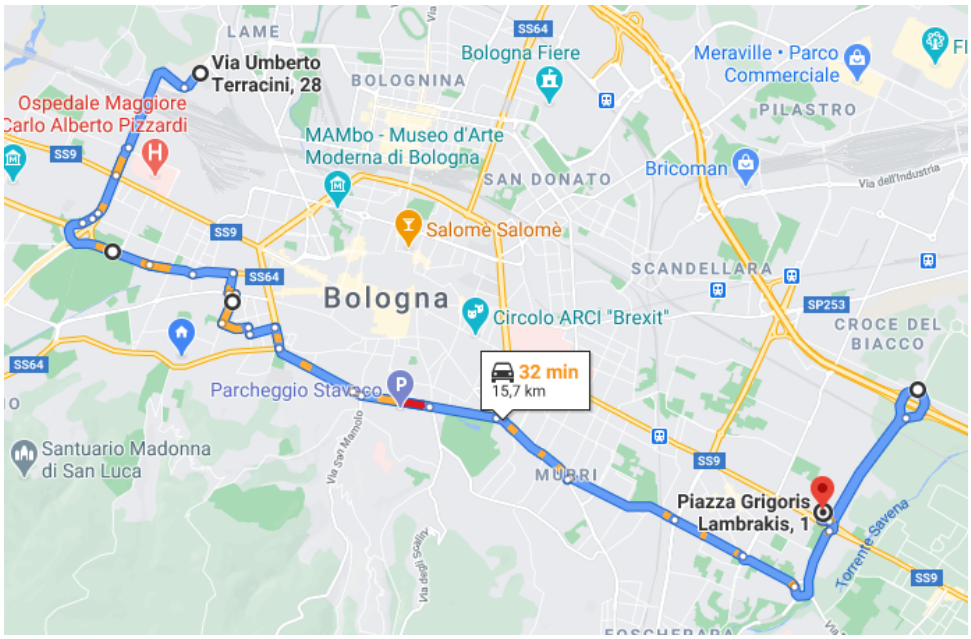

Figure 5.7: Scenario for speed profile predictor validation [121].

For the sake of simplicity, in this section the results of the validation procedure will be briefly presented and discussed. For more details, the work described in [121] can be examined.

As an example, in the bottom graph of Fig. 5.8a the comparison between measured and predicted speed traces is presented for the test cases mentioned above. Since stop-over probabilities have been considered to properly handle stop events, it can be noticed that dynamic stops do not imply the vehicle always stops. Moreover, in the top graph it can be noticed how the reference MAS is lowered due to the traffic codes, represented in color in the middle graph. In particular, the

higher is the traffic density, the lower is the code weight CW and then the higher is the intensity of the maximum speed reduction.

Speed- and energy-based KPIs are shown in Tab. 5.3. Although the speed limits have been exceeded two times (at 805 m and 1243 m) by the driver during the road test, it can be noticed that the predicted speed is centered (very low $BIAS$). Moreover, energy-based KPIs show that high accuracy on the energetic performance of the speed profile predictor have been achieved.

Table 5.3: Speed profile predictor validation [121]. KPIs.

MAE [km/h]	$BIAS$ [km/h]	$\lvert E_{RL} \rvert$ [Wh]	ΔE_{RL} [%]	$\lvert E_{I^+} \rvert$ [Wh]	ΔE_{I^+} [%]	$\lvert E_{I^-} \rvert$ [Wh]	ΔE_{I^-} [%]
12.4	-0.1	5	-0.4	32	-2	32	-2

5.4 Backward vehicle model

5.4.1 Architecture

In order to reconstruct the behavior of battery temperature and SoC over a given electronic horizon, the predictive functions rely on a backward vehicle model (BVM) which takes in to account the following parameters:

- *input parameter*
  they are provided by the speed prediction block and they are represented by the vectors of vehicle speed profile, $\mathbf{v}$, and the road slope profile, $\boldsymbol{\alpha}_{\%}$, and topological information regarding the zero-emission zone (distance and time from city entrance and exit) over the predicted eHorizon;

- *state variables*
  battery state of charge, ξ, and temperature, ϑ;

- *output parameters*
  vectors representing the predicted state of charge, $\boldsymbol{\xi}$, and temperature, $\boldsymbol{\vartheta}$, of the battery.

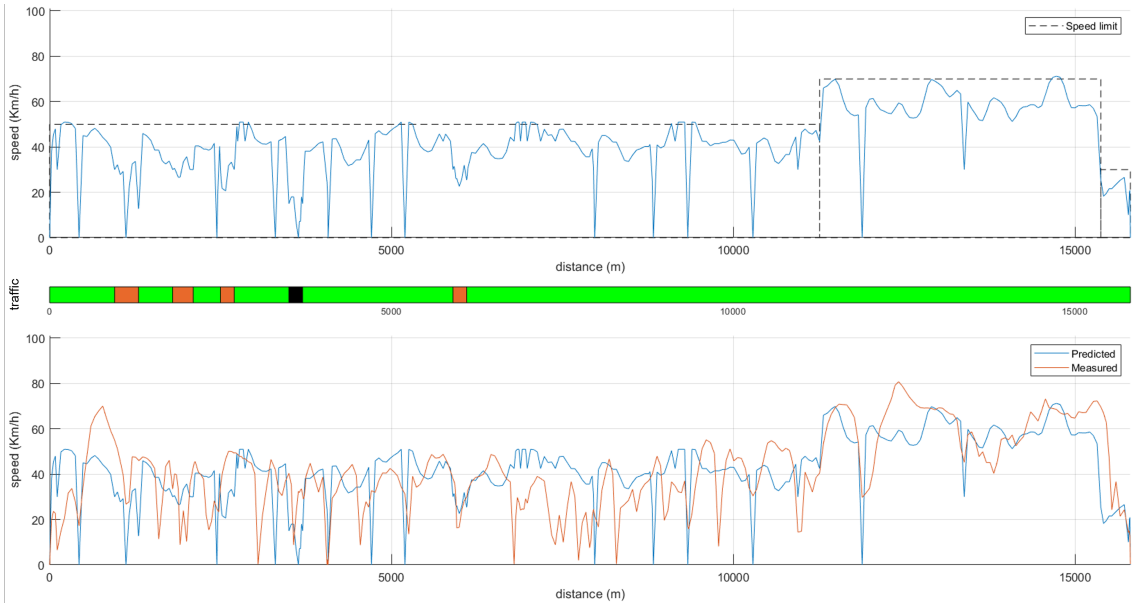

(a) Comparison between measured and predicted speed.

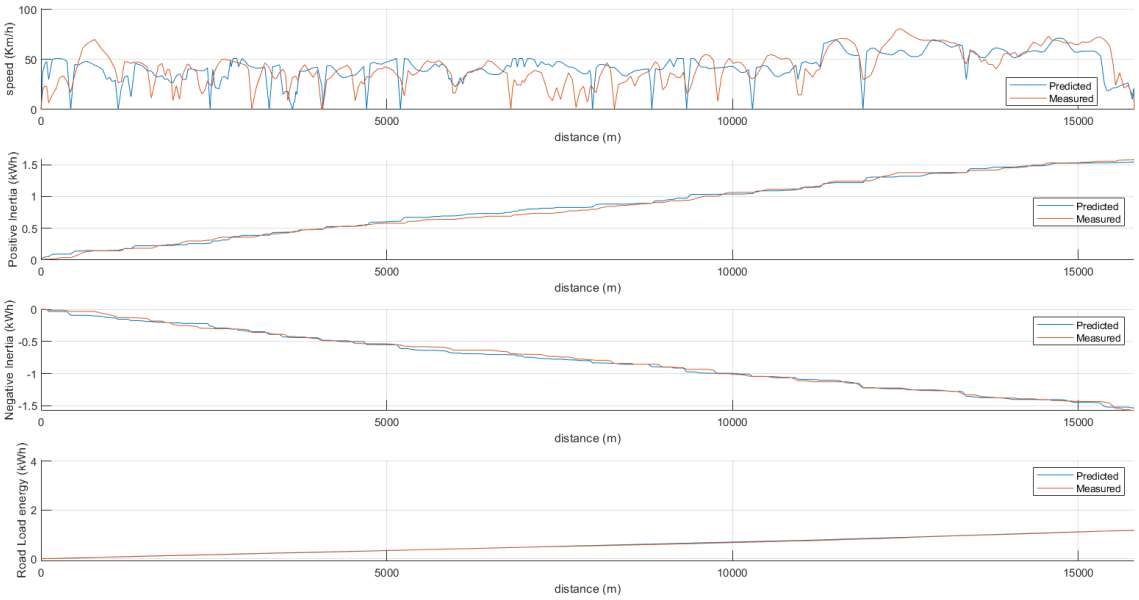

(b) Comparison between measured and predicted energy-related parameters.

Figure 5.8: Speed profile predictor validation [121].

The backward vehicle model is implemented in a *for-loop* block, where the number of iterations, N, is equal to the period of time required for crossing the urban area. In other words, $N = \Delta t_Z = t_{Z,out} - t_{Z,in}$. This results in a function time step equal to t_s = 1s. Higher time step values would lead to higher accuracy and, at the same time, to higher computational load. The energy management strategies take as input a certain value of SoC (the target one, ξ_t) to handle the zero-emission zone event. This means that there is no control based on a local, instantaneous comparison of the measured SoC with the predicted one. For this reason, a loss in the prediction accuracy of the SoC trend over the given horizon due to high time steps can be accepted.

The function containing the backward vehicle model is called every time a zero-emission zone is detected. It could happen:

1. at vehicle key-on
   assuming that the driver has set the destination of the trip and an urban area will be crossed;

2. in case of multiple urban events
   after an urban area has been crossed and another one is planned on the trip;

3. in case of navigation data update
   if the driver changes the route (because of road works or human mistakes), another one is usually planned which could include a passage in an urban area.

Although this piece of software has been developed in order to handle all the realistic test cases just mentioned, only the first one is taken into account. In fact, the behavior of the BVM is the same in all three cases. The main differences are that the last one needs V2N connectivity in order to be properly tested (which clearly is not available at SiL development level) and the second one can be considered just as a repetition of a single ZEZ event (which is handled as in test first test case).

5.4.2 Modeling

As introduced in Section 3.2.1, a backward-facing approach is used to make the prediction of the battery SoC over the given eHorizon. In this case, the source is

represented by the wheels and the sinks are the energy storage devices. Here, the battery power request is evaluated on the basis of the vehicle speed and road slope, which can be considered as external disturbances acting on the dynamic system represented by the vehicle. Moreover, dynamic effects such as torque control are not inherently included. Therefore, this results in a less complex model with benefits regarding computational load, which is a relevant aspect to be considered for algorithm implementation in a hardware.

The main equations of the backward vehicle model are reported in the following paragraphs.

The vehicle dynamics analytical model only takes into account the longitudinal forces acting on the car, as discussed in Section 3.3.1. Thus, the fundamental equation for vehicle longitudinal dynamics (Eq. (3.1)) in discrete domain, i.e. for the k-th iteration of the for-loop, for $k = 1,\ldots,N$, can be rewritten as:

$$m_v \cdot \frac{\Delta v(k)}{\Delta t(k)} = m_v \cdot \frac{v(k) - v(k-1)}{t_s} = F_{mot}(k) - F_{res}(k) \tag{5.21}$$

where $v(k) = [\mathbf{v}]_k$ is the predicted vehicle speed, and being $\Delta t(k) = t(k) - t(k-1) = t_s$. The resistance force F_{res} can be expressed as follows:

$$F_{res}(k) = f_0 + f_1 \cdot v(k) + f_2 \cdot v(k)^2 + m_v g \sin \alpha(k) \tag{5.22}$$

where $\alpha(k)$ is the slope angle of the road, which can be derived from the input percentage slope $\alpha_{\%}(k) = [\boldsymbol{\alpha}_{\%}]_k$ by the relationship:

$$\alpha(k) = \arctan \frac{\alpha_{\%}(k)}{100} \tag{5.23}$$

Hence, the total force requested at the wheels is:

$$F_r(k) = F_{res}(k) + \left(m_v + m_{eq,rot}\right) \cdot \frac{v(k) - v(k-1)}{t_s} \tag{5.24}$$

with obvious meaning of the symbols, already used in Section 3.3.1.

Then, the torque request at the wheels is:

$$T_r(k) = F_r(k) \cdot r_w \tag{5.25}$$

with r_w being the wheel radius.

From the knowledge of the total torque request at the wheels, it is possible to calculate the torque request to the electrical machines on the front axle by following the transmission chain from the wheels to the motors:

$$T_{w,f}(k) = T_r(k) \cdot u_s(k) \tag{5.26}$$

where $T_{w,f}$ is the torque to be provided on the front axle according to the torque split factor, u_s, between the electrical and hybrid paths. When it is equal to 1, the total amount of torque requested at the wheels is provided by the two electric motors on the front axle and the engine is switched off. Otherwise, if $u_s = 0$, the engine provides the whole torque requested at the wheels and the electrical machines on the front axle are used only for regenerative braking. Since the considered eHorizon is related to a zero-emission zone, the traction torque will be provided only by the P4 motors, and thus $u_s = 1$.

At the front differential gear, the motor speed is:

$$n_{EM}(k) = n_w(k) \cdot \tau_{dif,f} \tag{5.27}$$

where $\tau_{dif,f}$ is the fixed transmission ratio. Still, at the motors side, the requested torque is:

$$\begin{aligned} T_{dif,f}(k) &= \frac{T_{w,f}(k)}{\tau_{dif,f}} \cdot {\eta_{dif,f}}^a \\ a &= \begin{cases} -1, & T_{w,f}(k) > 0 \\ 1, & T_{w,f}(k) \leq 0 \end{cases} \end{aligned} \tag{5.28}$$

Reaching the motors, the speed is the same as the motors shaft of the differential

gear, while the torque requested is:

$$T_{EM}(k) = T_{dif,f}(k) \cdot {\eta_{EM}}^{a}$$
$$a = \begin{cases} -1, & T_{dif,f}(k) > 0 \\ 1, & T_{dif,f}(k) \leq 0 \end{cases} \tag{5.29}$$

being η_{EM} the mapped motors' efficiency as a function of the requested torque, T_{EM}, and the motor speed, n_{EM}, as shown in Fig. 3.6.

The vehicle analytic model is completed by the battery model. It starts with the calculation of the global electrical power request:

$$P_b(k) = P_{EM}(k) + \frac{P_{aux}}{\eta_{DCDC}} \tag{5.30}$$

in which $P_{EM}(i) = n_{EM}(k) \cdot T_{EM}(k)$ is the power requested from the motors on the front axle either for traction or regenerative braking, P_{aux} is the constant power to be supplied to the LV battery and the other auxiliaries, η_{DCDC} is the efficiency of the DCDC converter. Differently from Eq. (3.18), in this case the terms P_{ISG}, P_{ACC} are considered null because the former is related to the load-point shifting (not applied in pure-electric mode), and the latter is neglected due to the fact that no control strategy is implemented in such a model. This assumption is even more robust considering that the battery cooling power request is two order of magnitudes less than the power requested for vehicle propulsion, i.e. $P_{EM}(i)$. To this aim, the initial value of the predicted battery temperature has been set accordingly to a nominal value of $\vartheta_1 = \vartheta(k = 1) = 20°C$, ensuring no battery cooling within urban area during the prediction, as will be shown in Section 5.4.3.

At this point, analogously to the BMS, the battery power request is modified according to power limitation maps. They take into account charge-discharge and peak-nominal working conditions of the battery in order to establish the maximum power as a function of its actual SoC and temperature. These parameters are calculated by the battery electrical and thermal models, respectively, which are the same used in the vehicle's SiL model, as previously explained in Section 3.4.

Therefore, the battery state of charge can be estimated as:

$$\xi(k) = \xi_1 - \frac{\eta_c}{C_n} \sum_k I_b(k) t_s \tag{5.31}$$

being $\xi_1 = \xi(k = 1) = 95\%$.

With regards to to the thermal model, considering the previous assumption on the battery cooling power, it can be stated as $\dot{Q}_{cool}(k) = 0 \Rightarrow P_{ACC}(k) = 0$, $\forall k = 1,...,N$. Therefore, only the convective heat exchange between the battery and the surrounding air has been considered. Thus, the temperature of the battery can be calculated as:

$$\vartheta(k) = \vartheta_1 + \frac{1}{m\ c_p} \sum_k \left(P_{b,loss}(k) - \dot{Q}_{air}(k) \right) t_s \tag{5.32}$$

Then, at the end of each iteration k, the predicted SoC value, $\xi(k)$, is assigned to the relative vector:

$$[\xi]_k = \xi(k), \quad \forall k = 1,...,N \tag{5.33}$$

that, at the end of the iterative process, will be as follows:

$$[\xi] = \left[\xi_p \mid \mathbf{0} \right] = [\xi_1 \ \dots \ \xi_N \mid 0 \ \dots \ 0] \tag{5.34}$$

being $\dim(\xi) = M \geq N = \dim(\xi_p)$ in order to prevent issues related to memory dynamic allocation during software deployment.

In conclusion, as explained in this section, the ZEZ eHorizon reconstruction made by the BVM from the navigation data, namely the vehicle speed profile, $\mathbf{v}$, and the road slope profile, $\boldsymbol{\alpha}_{\%}$, led to the prediction of the SoC trajectory, ξ, among the given horizon. The latter is then fed into the ZEZ function.

5.4.3 Validation

The backward vehicle model used for battery SoC prediction has been validated over simulated data obtained by SiL vehicle model, already validated in Section 4.2.4. The vehicle speed and the road slope profiles, necessary for the prediction, have been assumed to be known a priori.

Predicted state of charge and temperature are compared to the relative simulated signals, as shown in Fig. 5.9. In particular, since the eHorizon is always represented by a ZEZ event, only the urban sectors of the considered RDE cycles have been considered (Fig. 5.9b, Fig. 5.9c).

Numerical results presented in Tab. 5.4 show an acceptable accuracy for the prediction of both the state of charge and the temperature. In fact, it is $\epsilon_{\xi,\max} = \max\left|\xi_{sim} - \xi_{pred}\right| < 4\%$ and $\epsilon_{\vartheta,\max} = \max\left|\vartheta_{sim} - \vartheta_{pred}\right| < 1°\text{C}$.

Table 5.4: Numerical results of the backward vehicle model validation.

Test	Data	ξ_0 [%]	ξ_f [%]	$\varepsilon_{\xi,max}$ [%]	θ_0 [°C]	θ_f [°C]	$\varepsilon_{\theta,max}$ [°C]
1	SiL	95	62.3	-	20	24.1	-
	Predicted	95	61.5	1.2	20	23.9	0.3
2	SiL	95	42.3	-	20	27.3	-
	Predicted	95	38.6	3.8	20	28.1	0.8
3	SiL	95	27.6	-	20	26.4	-
	Predicted	95	28.2	2.5	20	26.9	0.5

5.5 Zero-Emission Zone function

Because of the assumption that urban areas shall be zero-emission zone, there is the necessity to enter these areas with a specific SoC, ξ_t, so as to drive the vehicle in pure electric mode.

Therefore, the baseline strategy (RBS), without the modifications introduced and previously explained, would not be capable to make the battery have enough energy available, causing the driver not to enter the ZEZ or to pay a fee for using the internal combustion engine. On the other hand, if an urban area is detected (by means of connectivity, which relies on the information sent by the map service provider), the backward vehicle model predicts the state of charge, ξ, of the battery along the city route, as explained in the previous section.

Then, the target SoC value can be derived from the SoC prediction, as schematically represented in Fig. 5.10. In formula:

$$\xi_t = \Delta\xi_Z + \xi_{\min} + \xi_s \tag{5.35}$$

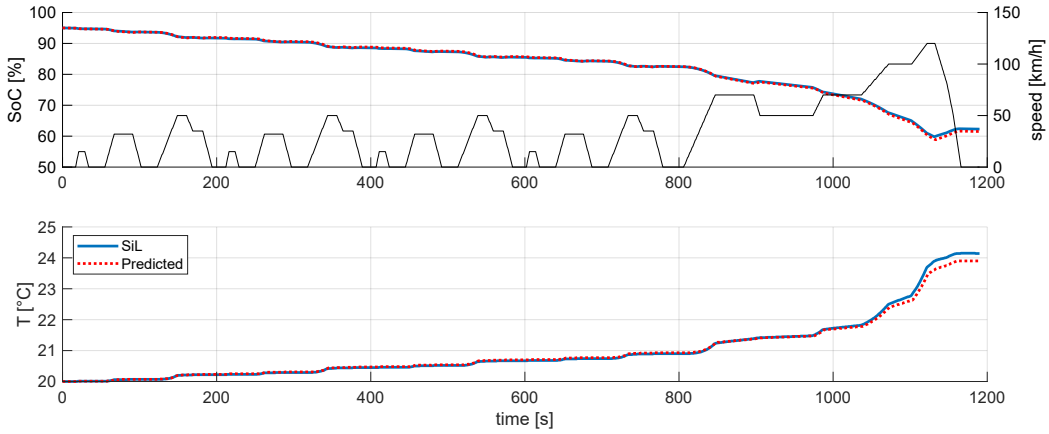

(a) TEST 1 - NEDC

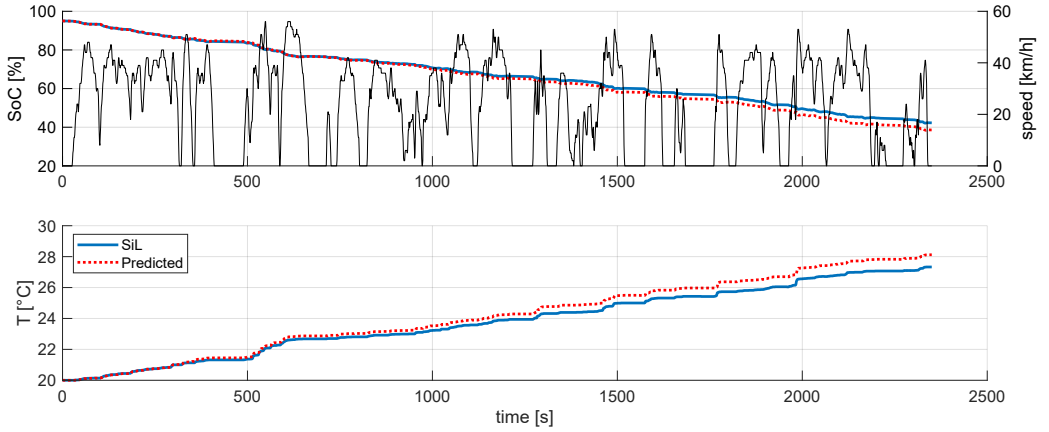

(b) TEST 2 - RDE Bologna (urban)

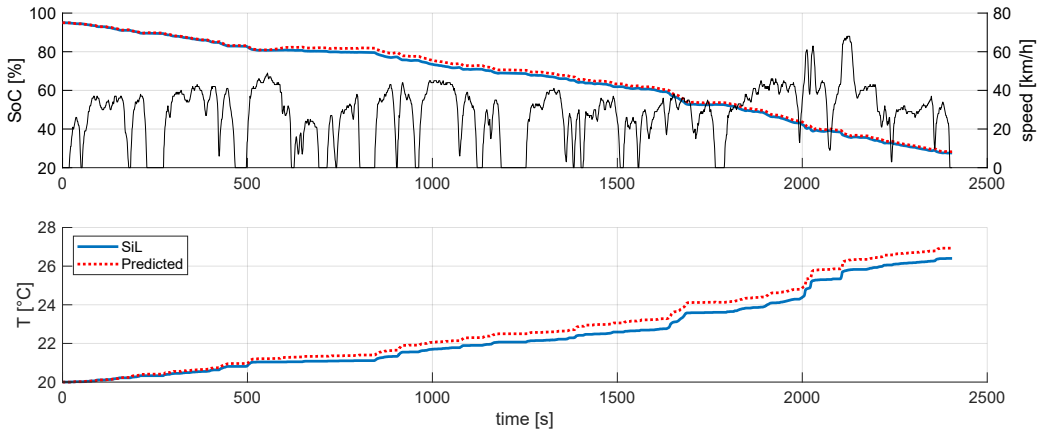

(c) TEST 3 - RDE Aachen (urban)

Figure 5.9: Backward vehicle model validation.

where:

$\xi_{\min} = \xi_{\min,el}$ is the minimum admissible SoC imposed by the battery manufacturer, which is equal to the lower SoC threshold to drive the vehicle in pure electric mode (see: Eq. (5.1));

$\Delta\xi_Z = \max(\xi) - \min(\xi)$ is the net amount of SoC to drive the zero-emission zone in pure electric drive;

ξ_s : positive offset value to ensure pure electric driving mode during the whole city passage. It then takes into account the variability of a real driver behavior and the traffic density.

At this point, the target SoC, ξ_t, is then fed to the energy management control strategies represented by the modified RBS (Section 5.1.2) and the Adaptive-ECMS, as discussed in the next section.

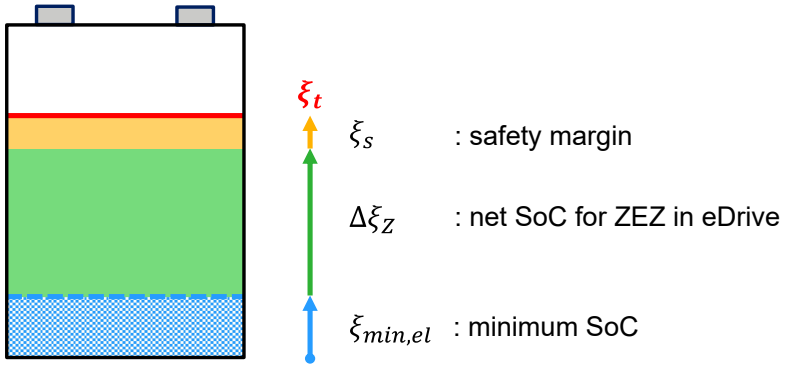

Figure 5.10: Schematic representation of target SoC evaluation.

5.6 Adaptive-ECMS

5.6.1 Working principle of the ECMS

It is well known that the approach proposed by the ECMS allows reducing the global energy minimization problem of HEVs to a local one which can be solved instantaneously, leading to a sub-optimal control strategy. In particular, the formulation of this control policy is based on the physical equivalence between the electric energy usage of the battery and the virtual fuel consumption associated

with it. Thus, the instantaneous equivalent fuel consumption to be minimized results in:

$$\dot{m}_{f,eq}(t) = \dot{m}_f(t) + \dot{m}_{f,b}(t) \tag{5.36}$$

where $\dot{m}_f$ is the effective fuel consumption referred to the engine, and $\dot{m}_{f,b}$ is the virtual fuel consumption associated with battery usage. By analogy with the engine, the latter can be expressed introducing a virtual specific fuel consumption, sfc_{eq}, giving:

$$\dot{m}_{f,b}(t) = sfc_{eq}(t) \cdot P_b(t) = \frac{s(\xi(t),t)}{Q_{lhv}} P_b(t) \tag{5.37}$$

where Q_{lhv} is the lower heating value of the fuel, $P_b(t)$ is the global electrical power request to the battery, and sfc_{eq} is considered proportional to a dimensionless equivalence factor, s.

5.6.2 Adaptive-ECMS

In [125] and more recently in [126] remarkable improvements have been obtained to make the ECMS a real-time control strategy. In particular, in the latter work, an adaption of the equivalence factor based on a feedback from SoC has been proposed. An attempt to apply this adaptive formulation of the ECMS to PHEVs is proposed in [102, 103]. As a result, the equivalence factor is expressed as:

$$s\left(\xi(t),t\right) = p\left(\xi(t),t\right) \cdot a\left(\xi(t),t\right) \tag{5.38}$$

where:

$$p\left(\xi(t),t\right) = 1 - k_p \left[\frac{\xi(t) - \left(\xi_{\max} + \xi_{\min}\right)/2}{\left(\xi_{\max} - \xi_{\min}\right)/2}\right]^n \tag{5.39}$$

$$a\left(\xi(t),t\right) = k_a \left(\xi_r(t) - \xi(t)\right) + \tfrac{1}{2}\left(s_{k-1} + s_{k-2}\right) \tag{5.40}$$

From Eq. (5.38) it can be noticed that there are two main contributions to the adaptive formulation of the equivalence factor, s.

The first one is expressed in Eq. (5.39) and it represents a penalty function with the aim of maintaining the state of charge of the battery within the range

$[\xi_{\min}, \xi_{\max}]$. This condition represents a local control constraint for HEV applications (where only a CS mode could be applied), while it can be considered a physical constraint in the case of a PHEV, like the considered vehicle. The definition of the penalty function is completed by the gain factor, k_p, also known as penalty factor, and the polynomial coefficient, n, which can be considered as tunable parameters.

The second contribution is represented in Eq. (5.40) by an adaptive function that plays a vital role in the real-time implementation of the ECMS. In fact, the drawback of the off-line tuning of the equivalence factor for a given drive cycle is solved by an online adaption based on the feedback from the SoC, represented by the term $\xi_r(t) - \xi(t)$. This results in a proportional correction of s by considering an adaptive factor, k_a, and the difference between the reference value of the SoC, ξ_r, and the actual one. The introduced gain factor can be used for algorithm tuning, as well as the proportional factor. In case of availability of navigation data regarding the planned route, for a PHEV the reference SoC to be followed by the control policy can be expressed as a linear function of the total distance of the trip in order to gradually discharge the battery among the driving mission. Thus, neither a battery discharging nor sustaining behavior is favored, and then the resulting working mode could be referred to as a charge-blended (CB). Since the adaption is performed periodically every $t = k \cdot t_u$, $k = 1,2,\ldots$, the terms s_{k-1} ands_{k-2} are the values of the equivalence factor used in two previous time intervals, namely adaptation steps. Therefore, they introduce an integral correction on the equivalence factor.

5.6.3 Adaptive-ECMS for ZEZ handling

With respect to the works described in [102, 103], the following modifications have been introduced to the previous formulation of the A-ECMS algorithm.

Regarding the reference SoC, the general formulation previously proposed for a generic drive cycle has been modified as:

$$\xi_r(d(t)) = \xi_i + \frac{\xi_f - \xi_i}{d_f - d_i}(d(t) - d_i) \tag{5.41}$$

with the following assumptions related to the zero-emission zone:

$$\begin{cases} t_f = t_{i,z} \\ d(t_f) = d_f = d_{i,z} \\ \xi(t_f) = \xi_f = \xi_{i,z} \end{cases} \tag{5.42}$$

In order to clarify the concept behind the reference SoC for ZEZ and all the introduced parameters, the diagram shown in Fig. 5.11 is presented. The parameters with the i and f subscripts refer to the initial t_i and final t_f time instants delimiting the CB mode, while d indicates the distance.

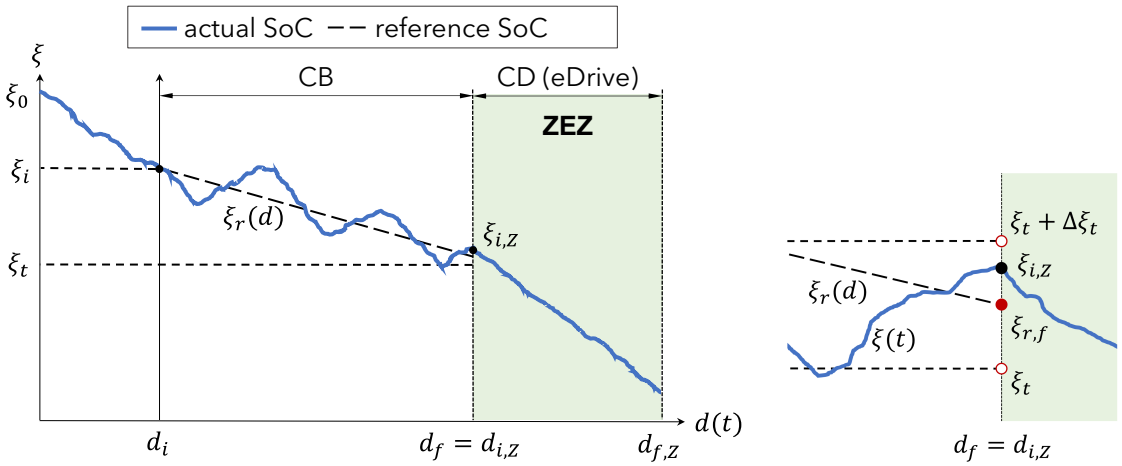

(a) Actual and reference SoC trends. **(b)** Beginning of the ZEZ.

Figure 5.11: Charge-Blended (CB) A-ECMS for ZEZ handling [98].

As shown in Fig. 5.11a, the key-on is performed at the beginning of the drive cycle, at $t = t_0 = 0$, while the predictive functions for SoC trajectory estimation (BVM and ZEZ) are called at $t = t_i$. Although, as previously explained, it is considered that the prediction is only performed at key-on ($t_i = t_0$). For sake of comprehension, the generic case ($t_i \neq t_0$) is shown in the diagram of Fig. 5.11a. In fact, this happens in all the other cases, such as for multiple ZEZ events and when the navigation data are updated. Then, CB mode is applied by the A-ECMS following the reference SoC expressed by Eq. (5.41) until the urban area is accessed at$t = t_f$ after the distance $d_f = d_{i,Z}$ has been traveled on the planned

route, thus representing the ZEZ entrance information (received from the map service provider via V2N).

Moreover, it is important to mention that in contrast to other formulations of the reference SoC, the global constraint $\xi_r\left(t_f\right) = \xi_{r,f} = \xi_t$ has been softened, as shown in Fig. 5.11b. The unused electrical energy associated with the SoC difference $\xi_{i,Z} - \xi_t$ is justified by the more important aim of pursuing a reliable and robust energy management control strategy for handling all the ZEZ in pure-electric driving mode. Therefore, the final reference SoC value becomes the reference SoC range $[\xi_t, \xi_t + \Delta\xi_t]$, centered in $\xi_{r,f}$, with $\xi_{r,f} > \xi_t$ and $\Delta\xi_t = 5\%$.

As a consequence, Eq. (5.41) can be rewritten as:

$$\xi_r(d(t)) = \xi_i + \frac{\xi_{r,f} - \xi_i}{d_{i,Z} - d_i}(d(t) - d_i) \tag{5.43}$$

with the global constraint on the SoC value at the beginning of the ZEZ:

$$\xi_{i,Z} \in [\xi_t, \xi_t + \Delta\xi_t[\tag{5.44}$$

Once the reference SoC trend has been defined, the modality with which the A-ECMS follows it must be established.

With this aim, the adaptive factor k_a, which is the proportional gain of the adaptive term $a\,(\xi, t)$ defined in Eq. (5.40), has been used as a tuning parameter.

Therefore, several considerations on reference SoC-following control can be carried out. A mild following control has to be preferred in order to limit as little as possible the instantaneous optimization performed by the A-ECMS. In particular, this applies when the vehicle is far away from the city. Thus, when the actual distance $\Delta d_Z(t) = d_{i,Z} - d(t)$ between the vehicle and the beginning of the urban area is very high, the values of the adaptive factor k_a are very low. On the other hand, when the vehicle is about to enter the ZEZ, in order to satisfy the global constraint of Eq. (5.44), the controller has to strictly maintain the SoC $\xi_(t)$ around the reference value $\xi_r(t)$. Thus, a logarithmic behavior of the adaptive factor has been chosen to have high increments of the tuning parameter for small variations of the ZEZ distance only when approaching the urban area.

Moreover, in this situation, it can be noticed that it could not be useful applying

such an aggressive SoC-following control even if the global constraint is satisfied. In other words, if the vehicle is near the beginning of the ZEZ (low Δd_Z) and the difference $\Delta\xi_{r,f}(t) = |\xi_t - \xi_{r,f}|$ between the actual SoC and the final value of the reference one is low, as well, there is no need to further increase the adaptive factor. Therefore, if the parameter $\Delta\xi_{r,f}(t)$ is also taken into account, then a map of the adaptive factor as the one shown in Fig. 5.12 can be obtained.

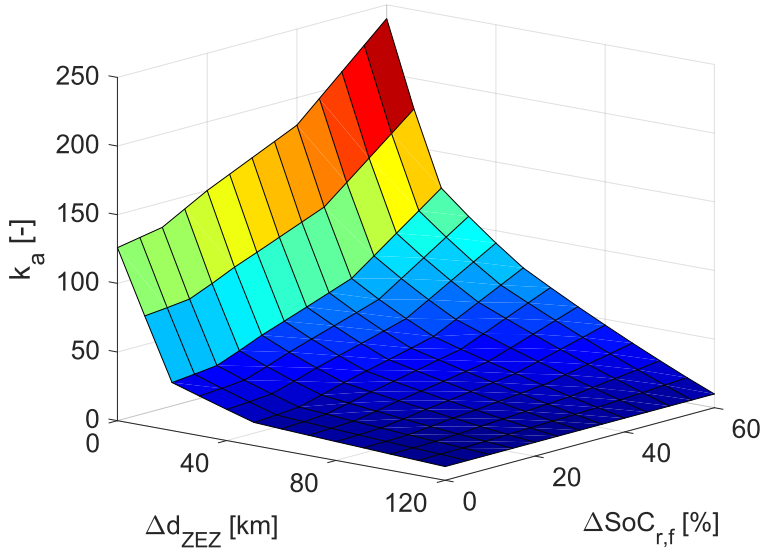

Figure 5.12: Map of the adaptive factor [98].

It must be said that such an approach could lead to very high values of the adaptive factor near the beginning of the urban area. This could result in much more aggressive behavior of the SoC-following policy. In order to soften this constraint, and thus to avoid overcoming the local optimization performed by the ECMS, the update time t_u of the adaptive term $a\left(\xi\left(t\right),t\right)$ has been decreased with the decreasing of the distance to the ZEZ entrance, as shown in Fig. 5.13. In this way, the SoC-following policy is made more accurate without the penalization introduced by high values of k_a in terms of optimization performance.

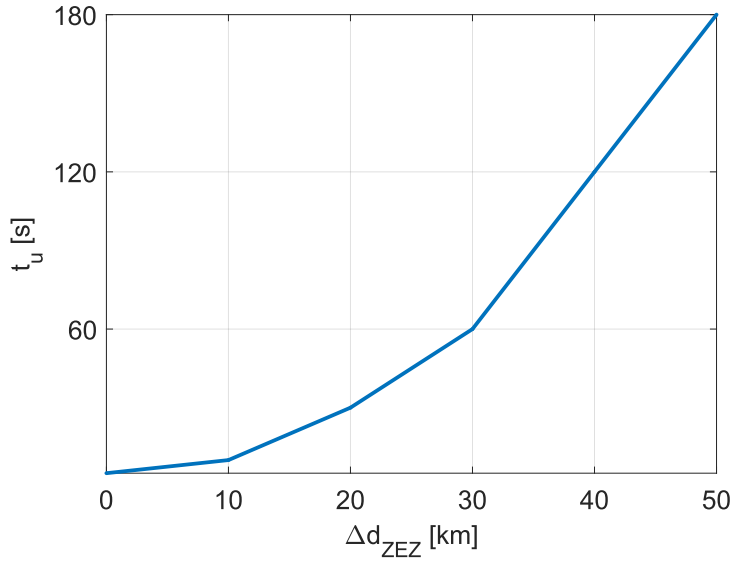

Figure 5.13: Map of the update time [98].

5.7 Dynamic Programming

Before introducing the results obtained by implementing in the SiL and HiL simulators the proposed control strategies for predictive ZEZ handling, this section describes the other contribution that was developed during this PhD research activity making use of the connected simulation environment, and specifically the development of a DP-based control strategy for handling energy and thermal management simultaneously.

5.7.1 Backward optimization algorithm

The main objective of an optimization-based algorithm such as Dynamic Programming (DP) is to evaluate the optimal control policy that minimizes a given cost function. To this aim, the optimization is achieved by induction, i.e. with a backward-facing approach, in order to reduce the number of iterations needed to retrieve the solution of the optimization problem. The validity of this procedure, ensured by Bellman's Principle of Optimality (Section 2.1.4.1), has been analytically proved in [127].

In formula, let u be an *admissible policy* for the optimal problem, defined as:

$$u = \{u_0, \ldots, u_k, \ldots, u_{N-1}\} \tag{5.45}$$

for each stage, or time index, $k = 0,1,\ldots,N-1$, being N the length of the considered horizon.

Thus, the cost function expressed for the admissible policy u, called *admissible cost*, can be formulated as:

$$J(x_0,u) = L_N(x_N) + \sum_{k=0}^{N-1} L_k(x_k,u_k,w_k) \tag{5.46}$$

where x_k, u_k, w_k, are, respectively, the system states, the control variables, and the disturbances acting on the dynamic system at the stage k. In other words, $J(x_0,u)$ represents the total cost required for the system to evolve from state x_0 at the initial stage $k = 0$ to the final state x_N at the last stage $k = N$, by applying the control policy u. The cost L_k associated to the transition from the state x_k to x_{k+1} is called *arc* or *instantaneous cost*.

Let U be the set of all admissible policies. Then, the *optimal control policy* $u^* \in U$ is the one minimizing the cost function of Eq. (5.46):

$$\min_{u \in U} J(x_0,u) = J^*(x_0) = J(x_0,u^*) \leq J(x_0,u)\,, \forall u \in U \tag{5.47}$$

As stated before, the minimum cost $J^*(x_0)$ can be obtained recursively, i.e. starting from the stage, N, where the terminal cost $J(x_N)$ is a constraint to ensure the desired state of the system at the final stage. Then, at each stage k, the *cost-to-go* is evaluated, which is the intermediate cost from state k to $N-1$. In formula:

$$J(x_k,u_k) = \left[L_N(x_N) + \sum_{k+1}^{N-1} L_k(x_k,u_k,w_k) \right] + L_k(x_k,u_k,w_k) \tag{5.48}$$

Thus, the cost-to-go $J(x_k,u_k)$ from stage k can be obtained by summing the actual arc cost L_k to the remaining cost to the final stage N. At this point, the

intermediate optimal control policy u_k is the one minimizing the cost-to-go:

$$J^*(x_k) = \min_{u_k^*} J(x_k, u_k) \tag{5.49}$$

At the end of the recursive optimization process, namely at stage $k = 0$, the cost-to-go will be equal to the total cost $J(x_0, u)$ Eq. (5.46) and the intermediate optimal control policy will coincide with the global one u^*, then representing the global optimal solution (Eq. (5.47)) of the energy management problem.

5.7.2 Combined energy-thermal management problem

The application of the described generic algorithm to the considered complex dynamic system, i.e. the plug-in hybrid electric powertrain, needs an association between algorithm variables and specific problem variables. In this sense, two different optimization algorithms are considered. The first one can be referred to as standard, which means that it only considers the energy management control problem (*energy-DP*). The second one (*combined-DP*), which is the novel approach proposed in this work, also takes into account the battery temperature as a state variable and the battery thermal management control as a control variable.

For the optimization problem in question, the disturbances, which are the variables that are independent of the vehicle state, are the vehicle speed v and the road slope α profiles. Thus, the disturbance vector can be expressed as follows:

$$\mathbf{w} = [\mathbf{v}\ \boldsymbol{\alpha}]^T \tag{5.50}$$

With regards to the energy-DP, the state variables chosen for defining the system state are the battery state of charge, ξ, and the currently engaged gear, g. Moreover, the variables for the powertrain operating control are the torque split factor, u_s, and the torque T_s associated to engine load point shifting for battery recharging. The latter is used in combination with the split factor to define the total amount of torque the engine has to provide and, multiplied by -1, to calculate the torque of the ISG. Thus, the vectors representing the state and control variables

are respectively defined as:

$$\mathbf{x} = [\mathbf{x}_E] = [\mathbf{g}\ \boldsymbol{\xi}]^T \tag{5.51}$$

$$\mathbf{u} = [\mathbf{u}_E] = [\mathbf{u}_s\ \mathbf{T}_s]^T \tag{5.52}$$

Concerning the combined-DP, the battery temperature ϑ and the control signal u_c of battery cooling circuit actuators have been considered as additional state and control variables. Thus, Eq. (5.51) and Eq. (5.54) can be rewritten as follows:

$$\mathbf{x} = [\mathbf{x}_C] = [\mathbf{x}_E \mid \mathbf{x}_T]^T = [\mathbf{g}\ \boldsymbol{\xi} \mid \boldsymbol{\vartheta}]^T \tag{5.53}$$

$$\mathbf{u} = [\mathbf{u}_C] = [\mathbf{u}_E \mid \mathbf{u}_T]^T = [\mathbf{u}_s\ \mathbf{T}_s \mid \mathbf{u}_c]^T \tag{5.54}$$

In order to define the mentioned vectors, a specific discretization has been set for each variable. Thus, the generic discretized variable $\mathbf{z}$ can be represented in the form:

$$\mathbf{z} = [z_{\min} : \Delta z : z_{\max}]^T \tag{5.55}$$

being Δz the minimum step the algorithm can take to span a variable vector. In this sense, the algorithm is considering that the problem variables can only be part of the fixed domain and, moreover, assume the discrete values defined by discretization[1]. In particular:

$\xi_{\min}$,$\xi_{\max}$: define the battery operating range for a PHEV, and thus they represent a physical constraint of the component;

$\vartheta_{\max}$: is the higher threshold value for battery operating temperature range, defined by the manufacturer, in order to prevent performance de-rating and premature aging of the component;

$T_{s,\max}$: depends on the maximum torque deliverable by the ISG;

$\Delta u_s = 1$, meaning that the driver torque request is fully provided either by the engine or the electric machines;

$\Delta u_c = 1$, meaning that the battery cooling is either active or not;

$\Delta g = 1$.

[1]For this reason, this optimal control strategy can be also referred to as *discrete* dynamic programming (DDP).

For the combined-DP, since both energy and thermal management are simultaneously optimized, the final cost J_N depends not only on the required value of the battery state of charge, ξ_f, but also of the temperature, ϑ_f, and are:

$$\xi_f = 30\% \in [20,95]\% = [\xi_{\min},\xi_{\max}] \tag{5.56}$$

$$\vartheta_f = 38°\text{C} < 40°\text{C} = \vartheta_{\max} \tag{5.57}$$

The cost-to-go be minimized at each stage k is represented by the engine fuel consumption $\dot{m}_f = f(n_{ICE},T_{ICE})$, mapped as a function of engine speed and torque (Fig. 3.5a). Thus, the cost-to-go defined in Eq. (5.48) can be rewritten as:

$$J(x_k,u_k) = L_N(\xi_N,\vartheta_N) + \sum_{k}^{N-1} \dot{m}_{f_k}(x_k,u_k,w_k) \tag{5.58}$$

where x_k, u_k, w_k are the k-th elements of the vectors represented in Eq. (5.53), Eq. (5.53), Eq. (5.50), respectively.

Thus, the optimization algorithm is applied starting from the ending of the driving mission (whose length is N) and proceeding to the initial one ($k = 0$), resulting in a backward-facing approach, as previously discussed. Then, for each stage $k = N-1,\ldots,0$, the cost-to-go in Eq. (5.58) is evaluated by means of a backward vehicle model, which takes the speed and the slope signals (Eq. (5.50)) as inputs. With this aim, the optimal solution is provided by searching for all the possible control options $\mathbf{u}$ (Eq. (5.54)), i.e. all the values of the discretized control set-points are applied to the powertrain model. Then, as outputs, the state variables $\mathbf{x}_k$ (Eq. (5.53)) and the engine fuel consumption can be calculated.

The optimization algorithm, including the backward vehicle model, has been implemented as a MATLAB script by means of nested for-loops related to stage and control variables recursions. The time index k has been defined in a way that $\Delta t_k = t_{k+1} - t_k = 1$ s. Then, the control variables of the optimal control policy $\mathbf{u}_c^*$ provided by the recursive algorithm have been mapped as a function of the discretized states of the system, expressed in the form of Eq. (5.55), and time, in order to ensure the implementation of the map in the vehicle simulator.

5.7.3 Backward vehicle model

In order to clarify the recursive optimization procedure and, in particular, the cost-to-go evaluation, the powertain model of the given PHEV is here described.

As introduced in Section 3.2.1, a backward-facing approach has been used for the modeling purpose, since data related to the driving mission are the inputs and the state variables the outputs, form which the cost function is recursively calculated.

Therefore, at the generic stage k, considering the well-know equation of a vehicle in longitudinal motion (Eq. (3.1)), the torque request at the wheels, $T_r(k)$, can be easily determined.

At this point, differently from the backward vehicle model discussed previously in Section 5.4.2, which is focused only on the electric powertrain, the torque split factor u_s can be null, as well. Thus, considering now the conventional powertrain, too, the torque to be supplied to the rear wheels is:

$$T_{w,r}(k) = T_r(k) \cdot (1 - u_s(k)) \tag{5.59}$$

from which the torque request at the engine side can be evaluated as:

$$T_{t,in}(k) = \frac{T_r(k)}{\tau_t\left(g(k)\right)} \cdot \frac{1}{\eta_t} \tag{5.60}$$

where η_t is the transmission efficiency, and τ_t is the total gear ratio considering both the actual gear ratio of the automatic transmission and the rear differential. The gear ratio depends on the currently engaged gear $g(t)$ and it is defined only for the rear axle, while if the vehicle is propelled only using the electrical machines on the front axle, the automatic transmission is decoupled from the crankshaft by means of a clutch.

Therefore, the engine torque request is:

$$T_{ICE}(k) = T_{t,in}(k) + T_s(k) \tag{5.61}$$

and, consequently, the torque request to the ISG (P1) can be expressed as:

$$T_{ISG}(k) = -T_s(k) \tag{5.62}$$

Since the ISG is directly mounted on the crankshaft, its speed is equal to engine one, which is:

$$n_{ICE}(k) = n_w(k) \cdot \tau_t(k) \tag{5.63}$$

being n_w the wheels speed.

In this case, since both the conventional powertrain and the battery cooling circuit are taken into account, the battery power request defined in Eq. (3.18) can be applied. In particular, let $P_c(k)$ be the electric power absorbed by the battery cooling circuit actuators. Then, the battery power request can be rewritten as:

$$P_b(k) = P_{EM}(k) + P_{ISG}(k) + \frac{P_{aux}}{\eta_{DCDC}} + P_c(k) \tag{5.64}$$

where the contribution related to battery thermal management, $P_c(k)$, is:

$$P_c(k) = u_c(k) \cdot \left(P_{ACC}(k) + \frac{P_{eP}}{\eta_{DCDC}} \right) \tag{5.65}$$

being $P_{ACC}(k)$, P_{eP} the electrical power absorbed by the high-voltage compressor and the electric pump of the battery cooling circuit, respectively. It is assumed $P_{eP} = const.$, as well.

Then, omitting the battery electrical and thermal models, previously explained in Section 3.4.1 and widely applied in this dissertation, it is possible to evaluate the battery state of charge and temperature at the next stage $k + 1$ as:

$$\begin{aligned} \xi(k+1) &= \xi(k) - \Delta\xi(k) \\ &= \xi(k) - \frac{\eta_c}{C_n} I_b(k) \Delta t_k \end{aligned} \tag{5.66}$$

$$\begin{aligned} \vartheta(k+1) &= \vartheta(k) + \Delta\vartheta(k) \\ &= \vartheta(k) + \frac{1}{m\ c_p} \left(P_{b,loss}(k) - \dot{Q}_{air}(k) - \dot{Q}_{cool}(k) \right) \Delta t_k \end{aligned} \tag{5.67}$$

where:

$$\xi(k) \in \boldsymbol{\xi} = [\xi_{\min} : \Delta\xi : \xi_{\max}]^T \tag{5.68}$$

$$\vartheta(k) \in \boldsymbol{\vartheta} = [\vartheta_{\min} : \Delta\vartheta : \vartheta_{\max}]^T \tag{5.69}$$

due to the variables discretization.

Chapter 6

Application of the control strategies

To asses the benefits of the developed control strategies in terms of energy efficiency and fuel saving, simulations under different conditions and with different driving cycles have been conducted. Numerical results are given and commented, as well.

6.1 CO_2 correction for the tested strategies

The CO_2 production has been chosen as one of the assessment parameters for comparing the energy consumption related to the applied control strategies for the different test cases. In order to make a proper comparison, a correction of the CO_2 production related to the usage of the tested strategies has been proposed on the basis of the following approach.

The electrical energy additionally used or saved at the end of the driving mission should be converted into an equivalent amount of fuel. In other words, the more the battery is used for traction, the less the engine is used for the same purpose, and thus an additional amount of fuel has to be added to the effective fuel consumption of the engine in order to cover the fuel saving related to the battery usage.

Since the correction of the fuel mass can be either positive or negative (due to

a more or less usage of the battery, respectively), it can be represented as follows:

$$\begin{aligned} \Delta m_f \, Q_{lhv} \cdot \bar{\eta}_{ICE} &= \frac{\Delta E}{\bar{\eta}_{ISG}} \\ \Delta m_f \, Q_{lhv} \cdot \bar{\eta}_{ICE} &= \Delta E \cdot \bar{\eta}_{EM} \end{aligned} \tag{6.1}$$

which yields to the mass fuel correction:

$$\begin{aligned} \Delta m_f &= \frac{\Delta E}{Q_{lhv}} \cdot \frac{1}{\bar{\eta}_{ICE} \, \bar{\eta}_{ISG}} \\ \Delta m_f &= \frac{\Delta E}{Q_{lhv}} \cdot \frac{\bar{\eta}_{EM}}{\bar{\eta}_{ICE}} \end{aligned} \tag{6.2}$$

where $\Delta E = E_{ref} - E_{test}$ is the difference between the electric energy used by the battery whit the reference and the tested strategies, and $\bar{\eta}_{ICE}$, $\bar{\eta}_{EM}$, $\bar{\eta}_{ISG}$ are the average efficiencies of the engine, the electric motors, and the integrated-starter generator, respectively. The instantaneous engine efficiency is calculated as the ratio between the mechanical power provided by the engine and the chemical power of the injected fuel. Analogously, the instantaneous efficiencies of the electric machines are evaluated as the ratio between the power output and input, which can be either mechanical or electrical depending on the working mode of the component (EM: motor/generator, ISG: generator).

Finally, in order to evaluate the corrected CO_2 production $CO_{2,c}$, the corrected fuel consumption $m_{f,c} = m_f + \Delta m_f$ is multiplied by a conversion factor whose value is $k_{CO_2} = 2370 \; g_{CO_2}/l_{fuel}$. The latter can be calculated as suggested by [128] from the following equation:

$$FC = \left(\frac{0.1206}{\rho_f} \right) (0.829 \cdot \mathrm{HC} + 0.429 \cdot \mathrm{CO} + 0.273 \cdot \mathrm{CO_2}) \tag{6.3}$$

where $\rho_f = 0.75$ kg/l is the fuel density, and HC, CO and CO_2 are the production of the relative chemical agents [g/km]. In order to evaluate the conversion factor, the assumption HC = CO = 0 has been made.

6.2 Adaptive-ECMS for ZEZ handling

The charge-blended A-ECMS for ZEZ handling (Section 5.6.3), which is the tested strategy, is here compared to the energy management RBS, properly modified for the same purpose (Section 5.1.2).

They are implemented in the software of the supervisory controller within the SiL environment, which has been used to carry out the simulations. The results are presented in the following paragraphs.

Since the simulations are performed at SiL level, it is not possible to retrieve any navigation data from the map service provider. As a consequence, vehicle speed and road slope profile for battery SoC prediction are here assumed to be know a priori. Therefore, as shown in Section 6.4, the A-ECMS will be tested at the connected HiL with real-time routing information.

6.2.1 Test cases

A set of simulations composed of four test cases (TC), listed in Tab. 6.1, has been conceived.

Table 6.1: Test cases [98].

TC	Cycle	ξ_0 [%]	ξ_t [%]	d_Z [km]	$d_{i,Z}$ [km]	$d_{f,Z}$ [km]
1	Aachen	30	80	15.0	75.1	90.1
2	Cherasco	30	80	11.8	80.9	92.7
3	Aachen	95	50	9.0	81.1	90.1
4	Cherasco	95	50	6.5	86.2	92.7

Two different scenarios have been identified to compare the performance of the two strategies: short and long ZEZ. In fact, the higher the length d_Z of the trip within the urban area, the higher the target SoC ξ_t required at the beginning of the ZEZ.

Moreover, in order to reinforce the validity of the results, Real Driving Emissions (RDE) cycles have been chosen, as shown in Fig. 6.1. The speed and slope traces have been recorded by the industrial partner during road tests located in

Aachen, Germany (Fig. 6.1a) and Cherasco, Italy (Fig. 6.1b). They are compliant to the related R1151 European Regulation [128].

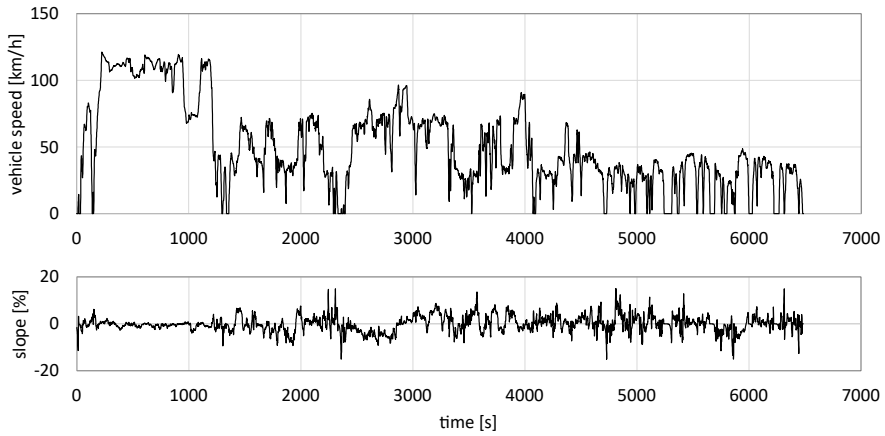

(a) Aachen.

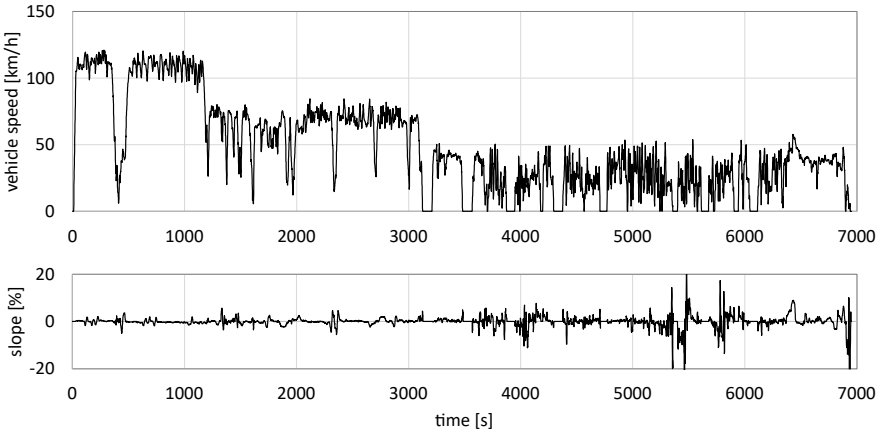

(b) Cherasco.

Figure 6.1: RDE cycles [98].

According to the legislation, they can be divided into three sections: highway, rural, and urban. In this case, the latter is the last one and for each drive cycle two different ZEZ have been individuated, with different length d_Z, so as to have the desired different values for the target SoC. For each test case, since the all-electric driving mode is always performed during the city passage, the strategies are applied only in the extra-urban areas, i.e. as long $d(t) < d_{i,Z}$. In both cases, the predictive functions calculate the value of the target SoC which is then fed to

the control strategies.

The initial SoC ξ_0 has been consequently chosen on the basis of the target SoC. It can be noticed that in this way it is possible to test the strategies in two different working conditions: overall charge depleting ($\xi_0 > \xi_t$) and increasing ($\xi_0 < \xi_t$).

6.2.2 Results

The SoC trends related to the RBS and the A-ECMS are presented in Fig. 6.3, Fig. 6.5, Fig. 6.7, Fig. 6.9. In particular, the actual $\xi(t)$, reference $\xi_r(t)$ and target ξ_t SoC behaviors are shown.

Numerical results of the simulations are listed in Tab. 6.2, as well. They include the SoC values at the beginning, $\xi_{i,Z}$, and at the end, $\xi_{f,Z}$, of the ZEZ, where the latter corresponds to the final SoC of the simulation; the raw and the corrected CO_2 productions (calculated over the entire driving cycle as explained in the previous paragraph) and the percentage relative differences evaluated as:

$$\Delta CO_2 = \frac{CO_2^{ECMS} - CO_2^{RBS}}{CO_2^{RBS}} \cdot 100 \tag{6.4}$$

In this way, a negative value of the parameter represents a fuel saving of the A-ECMS with respect to the baseline strategy properly modified. Note that if the corrected CO_2 consumption for the A-ECMS is used in Eq. (6.4), then the corrected value $\Delta CO_{2,c}$ is calculated.

In test cases 1 and 2 (Fig. 6.3 and Fig. 6.5), the control strategies have to recharge the battery to reach the target SoC, and thus a charge increasing mode has to be applied in the extra-urban areas. This objective is achieved by the RBS by means of a CI-CS mode, while the A-ECMS applies a CB mode, following the reference SoC which varies linearly over traveled distance. The SoC-following control is ensured by the adaptive factor and the update time, whose trajectories over time are depicted in Fig. 6.4, Fig. 6.6. Concerning the first parameter, it can be noticed that it behaves with a logarithmic-like trend, as previously explained. Furthermore, for each test case, the initial value of the adaptive factor is relatively low, despite the different initial conditions and target SoC values, as expected.

Table 6.2: CO_2 production [98].

TC	Strategy	$\xi_{i,Z}$ [%]	$\xi_{f,Z}$ [%]	CO_2 [g/km]	ΔCO_2 [%]	$CO_{2,c}$ [g/km]	$\Delta CO_{2,c}$ [%]
1	RBS	83.5	32.1	318	–	318	–
	A-ECMS	83.4	32.2	263	**-17.3**	259	**-18.5**
2	RBS	85.3	35.8	359	–	359	–
	A-ECMS	83.1	32.7	289	**-19.7**	292	**-18.8**
3	RBS	50.4	25.4	233	–	233	–
	A-ECMS	53.6	28.8	203	**-12.7**	199	**-14.6**
4	RBS	54.1	29.4	289	–	289	–
	A-ECMS	51.2	26.9	223	**-22.7**	224	**-22.6**

Table 6.3: Average efficiencies [98].

TC	Strategy	$\overline{\eta}_{ICE}$ [%]	$\Delta\overline{\eta}_{ICE}$ [%]	$\overline{\eta}_{EM}$ [%]	$\Delta\overline{\eta}_{EM}$ [%]	$\overline{\eta}_{ISG}$ [%]	$\Delta\overline{\eta}_{ISG}$ [%]
1	RBS	16.2	–	78.2	–	78.4	–
	A-ECMS	22.6	**+39.9**	80.3	**+2.6**	77.4	**-1.2**
2	RBS	16.1	–	77.8	–	78.1	–
	A-ECMS	22.8	**+42.2**	78.8	**+1.4**	77.5	**-0.8**
3	RBS	16.5	–	79.4	–	77.9	–
	A-ECMS	21.5	**+30.4**	79.3	**-0.2**	77.3	**-0.7**
4	RBS	15.9	–	80.5	–	77.5	–
	A-ECMS	22.0	**+38.5**	78.9	**-1.9**	76.9	**-0.8**

The RBS is strongly penalized by the charging phases of the CS mode, accomplished using the ICE and the ISG with the load point shift strategy. In fact, it can be seen that in the initial part of the RDE cycle, which corresponds to the highway section, the load point shift strategy is more efficient since the high load required by such a type of road, and a sharp increase of the SoC can be observed. Nevertheless, neglecting the regenerative brakings, every SoC increase due to battery recharging by means of the ICE is higher in the case of the A-ECMS with respect to the RBS, which leads to higher average efficiency, as shown in Tab. 6.3.

Analogous considerations can be made for test cases 3 and 4 (Fig. 6.7 and Fig. 6.9), even if a charge depleting mode is applied before the urban area. In this case, the RBS performs a CD-CS mode, while the A-ECMS is again in CB mode. As a representative example, in Fig. 6.2 the engine efficiency maps for RBS and A-ECMS for test case 3 are shown. The higher is the density of the operating points (blue dots), the higher is the operating frequency of the engine. The figures show that with the A-ECMS, the engine works at higher efficiency operating points (due to a higher load point shift) and for a shorter time (as no CS mode is applied).

In light of this analysis, the following explanation regarding the goodness of the CO_2 numerical results (Tab. 6.2) can be done. In fact, it has to be highlighted that the rule-based energy management strategy has been modified for ZEZ handling without a further calibration process, as it has been done for the base one. The reason of this approach relies on the fact that a complex control policy such as the given RBS, despite its inherent heuristic nature, would have required an intensive calibration and validation campaign. Therefore, in order to justify such a noticeable effort in this task, this activity had the main objective to produce a first study on the benefit of deploying such an adaptive-ECMS not only to optmize the vehicle energy management while applied, but even to reduce emissions in urban areas. Thus, this led the RBS to perform the load point shifting during the CS phase with the drawbacks previously discussed, resulting in the engine average efficiency penalization shown in Tab. 6.3. Aware of the limit of the proposed approach and of the encouraging results here presented, future works will be focused on reinforcing the heuristic strategy in order to improve the validity of the energetic assessment of the A-ECMS. Numerical results are expected not to be as positive as in the proposed case, because of the calibration of the RBS.

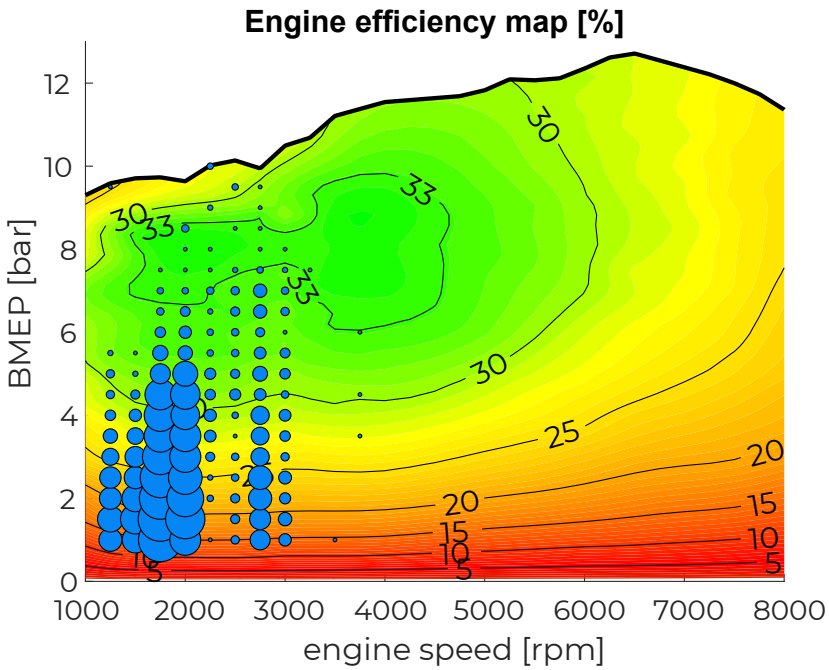

(a) RBS.

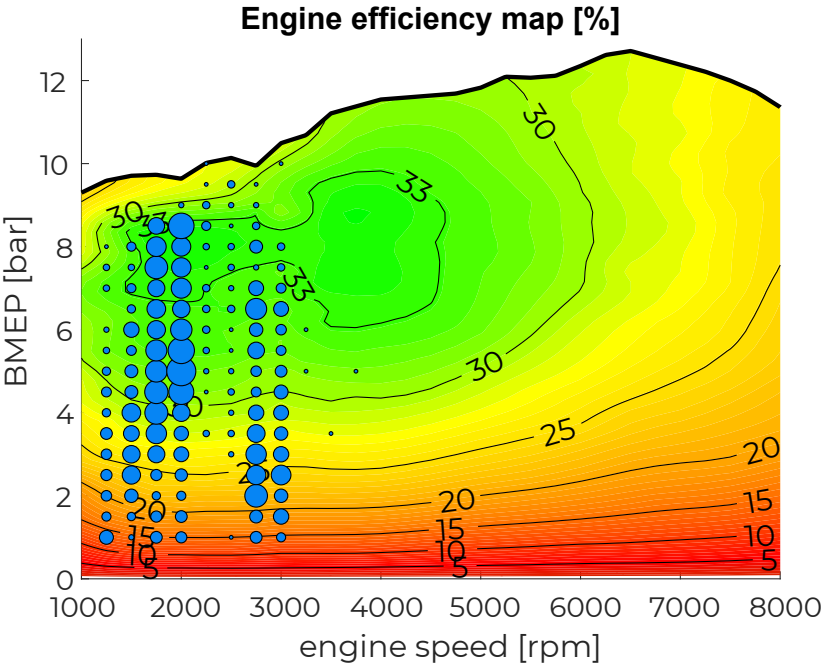

(b) A-ECMS.

Figure 6.2: Engine efficiency map with operating points for test case 3 [98].

Nevertheless, the instantaneous optimization performed by the ECMS could still provide benefits in terms of CO_2 reduction.

Moreover, as final comments, for each test case it can be noticed that:

- the value of the SoC target evaluated by the predictive functions is high enough to ensure pure electric driving for the whole length of the ZEZ.
  In formula: $\xi_{f,Z} > \xi_{\min} = 20\%$, being $\xi_{\min}$ the lower threshold of the SoC operational range of the battery, established by the manufacturer. In order to graphically represent this condition, the minimum value of the vertical axis of each figure has been set to $\xi_{\min}$;

- the value of the SoC at ZEZ entrance is higher than the required target SoC: $\xi_{i,Z} > \xi_t$.
  This is true for both the strategies and thus the vehicle is able to reach the destination of the trip in pure electric driving mode in every scenario;

- in particular, with regards to the previous condition, the A-ECMS satisfies the global constraint expressed in Eq. (5.44), which is $\xi_t \leq \xi_{i,Z} \leq \xi_t + \Delta\xi_t$, where $\Delta\xi_t = 5\%$;

- the all-electric driving mode is applied during the city passage, regardless of the strategy applied in the extra-urban sections.
  Therefore, the SoC trajectories are graphically similar and the differences between SoC values at the beginning and at the end of the ZEZ for every strategy remain quite the same;

- the A-ECMS results to be more energy-efficient than the standard RBS.
  This is true both for the raw and the corrected values of the CO_2 production;

- in particular, the maximum absolute variation between the raw and the corrected data is 1.9% (at TC3). Thus, the approach proposed for the correction does not significantly affect the results, and then it can be considered reliable;

- the average engine efficiency for the A-ECMS is higher than the one for the RBS.
  In particular, it can be noticed from Tab. 6.3 that the relative advantages for

the average engine efficiency, $\Delta\bar{\eta}_{ICE}$, are much higher than the one for the EMs, $\Delta\bar{\eta}_{EM}$, and the ISG, $\Delta\bar{\eta}_{ISG}$. This confirms that the observed benefits in terms of carbon dioxide reduction are due to a more efficient usage of the internal combustion engine.

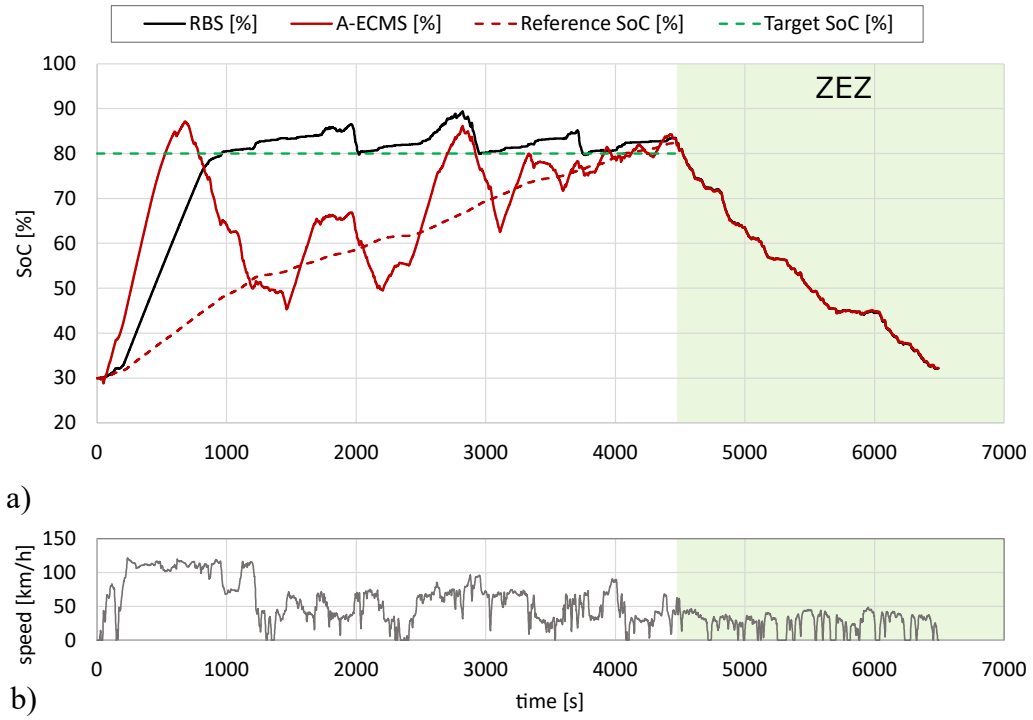

Figure 6.3: Test Case 1: a) SoC trends, b) vehicle speed [98].

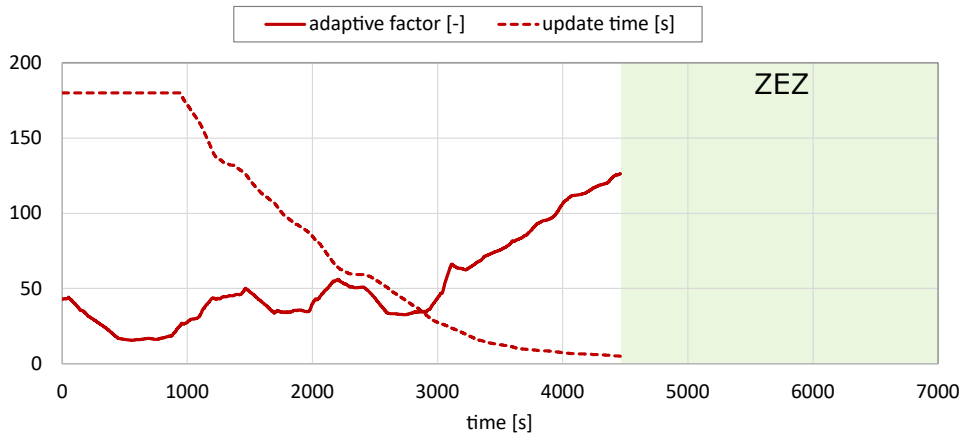

Figure 6.4: Test Case 1: trajectories for the adaptive factor and the update time [98].

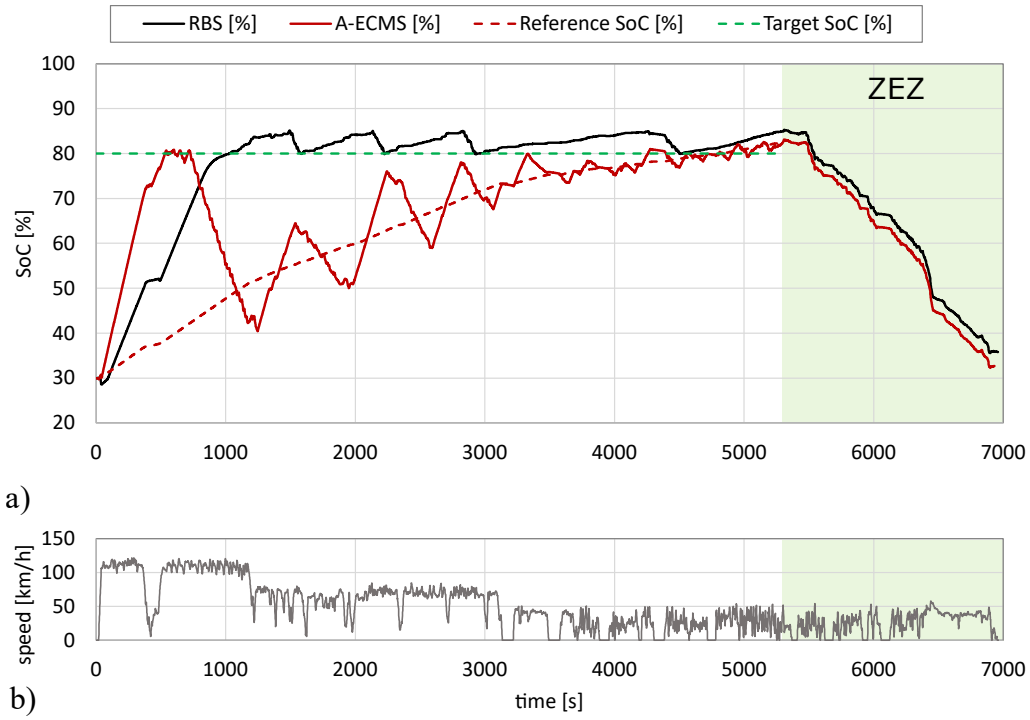

Figure 6.5: Test Case 2: a) SoC trends, b) vehicle speed [98].

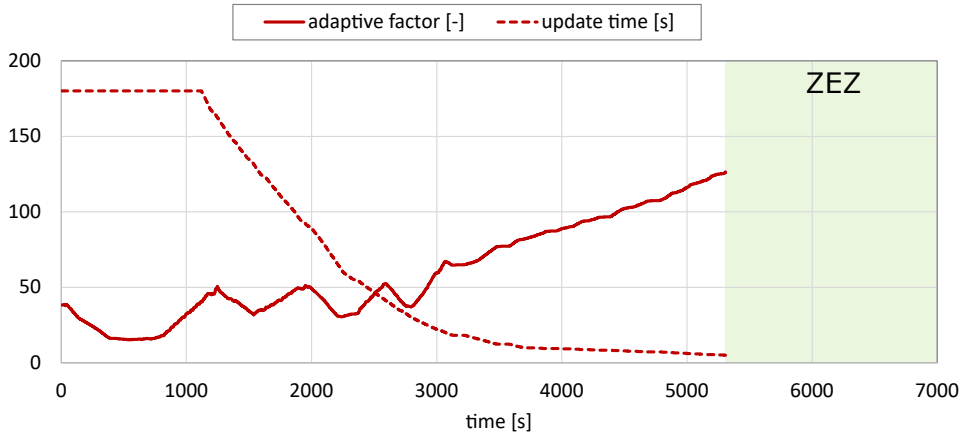

Figure 6.6: Test Case 2: trajectories for the adaptive factor and the update time [98].

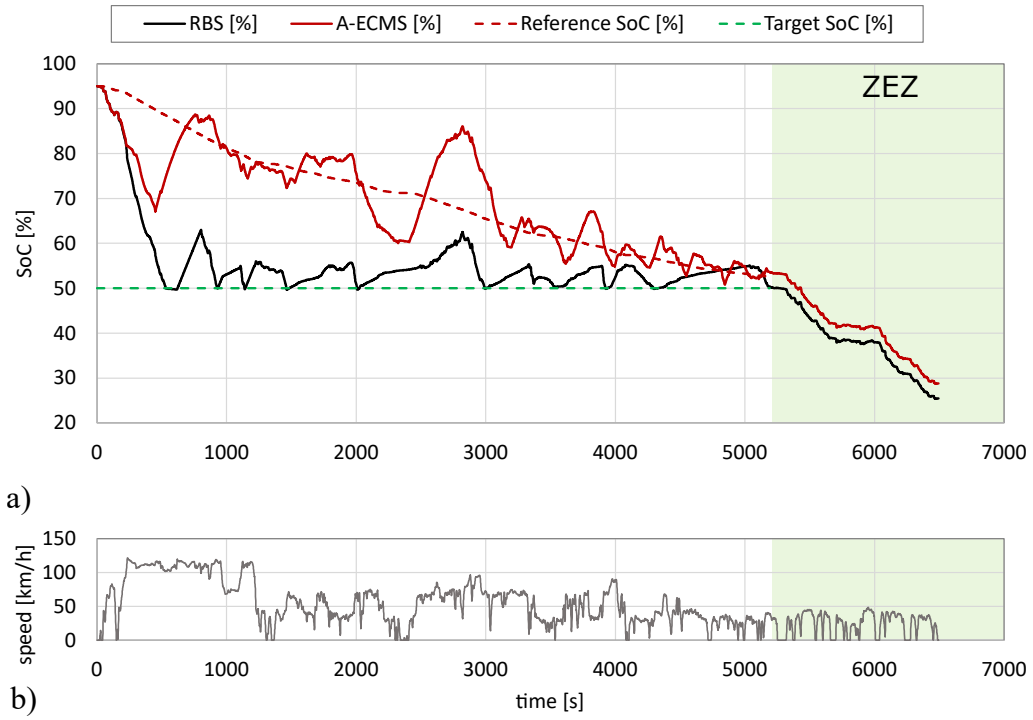

Figure 6.7: Test Case 3: a) SoC trends, b) vehicle speed [98].

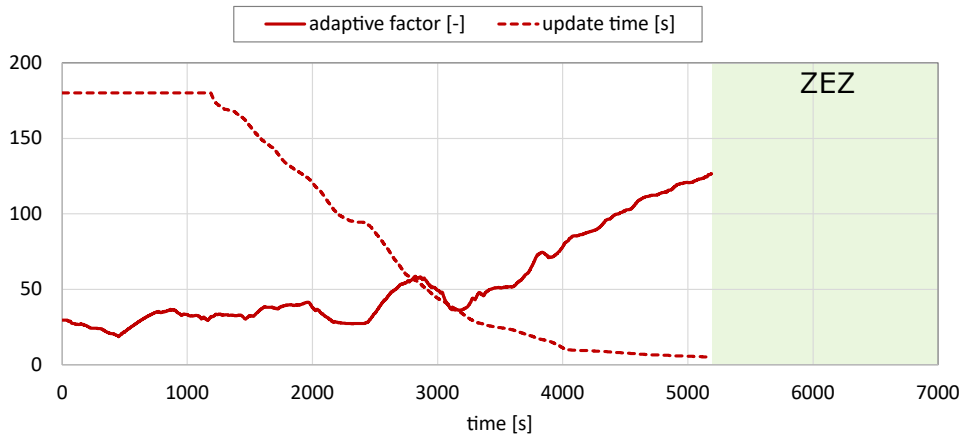

Figure 6.8: Test Case 3: trajectories for the adaptive factor and the update time [98].

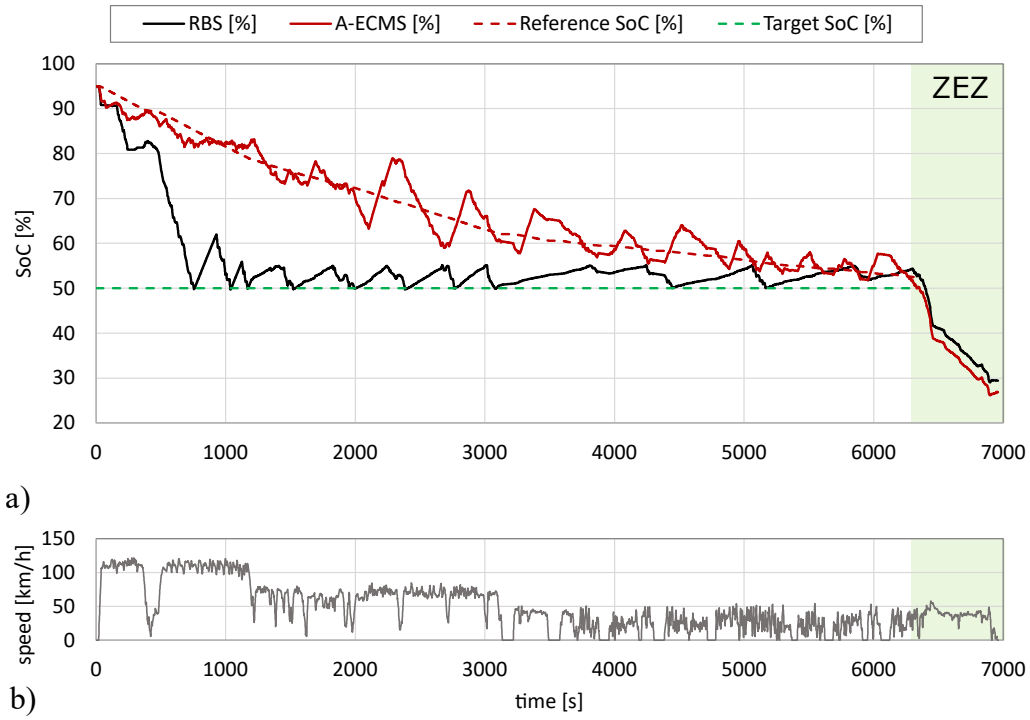

Figure 6.9: Test Case 4: a) SoC trends, b) vehicle speed [98].

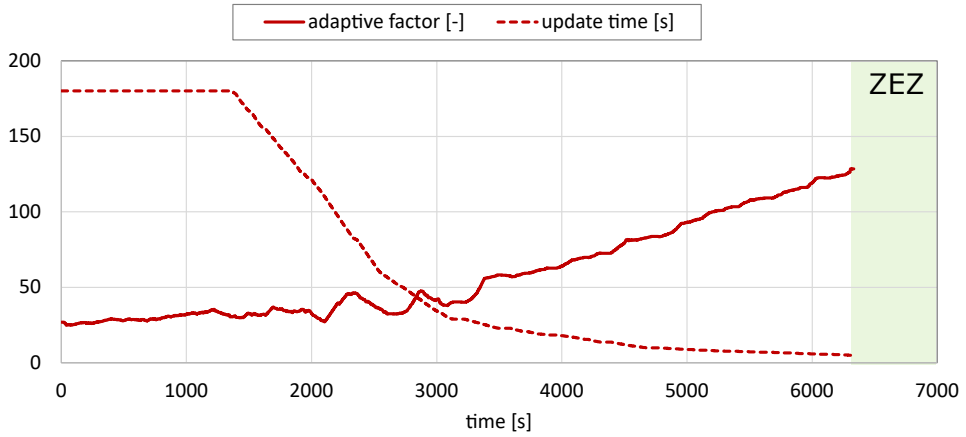

Figure 6.10: Test Case 4: trajectories for the adaptive factor and the update time [98].

6.3 Combined Dynamic Programming

The simultaneous energy-thermal management optimization performed by the developed dynamic programming algorithm (Section 5.7), which is the tested strategy, is here compared to the energy and battery thermal management RBS, as described in Section 5.1.1, Section 5.1.3, respectively.

For this purpose, the maps of the optimal control policies depending on the state variables have been implemented in a simplified model of the supervisory controller, thus resulting in a Model-in-the-Loop (MiL) simulator developed in Simulink environment, as well. Nevertheless, the powertrain modeling is unchanged with respect to the SiL one.

6.3.1 Test cases

The high-detailed MiL simulator has been used in order to investigate the effects of DP-based control strategies both for energy (Energy-DP) and energy-thermal management (Combined-DP). From here on, all the reported results derive from the MiL, where the optimal control policies calculated with the DP algorithm have been integrated into the controllers.

For the purpose, a simulations' set composed of three test cases (TC) has been conceived and collected in Tab. 6.4.

Table 6.4: Test cases [99].

TC	Applied control strategies	
	Energy mgm.	Thermal mgm.
1	RBS	RBS
2	Energy-DP	RBS
3	Combined-DP	

For each test case, different values of ambient temperature have been simulated, since such parameter has a high influence on the thermal behavior of the battery, and the same driving cycle has been performed. It is represented by the Real-Driving-Emission (RDE) located in Aachen already used and depicted in Fig. 6.1a.

However, in this case the cycle is not inverted, and thus, for the sake of clarity, speed and slope profiles of the cycle hereby adopted are shown in Fig. 6.11.

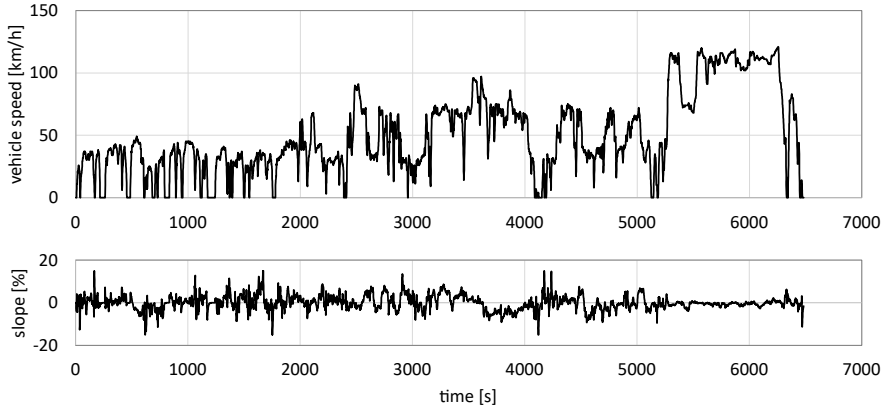

Figure 6.11: Aachen RDE cycle.

The decision of choosing such reference route is still due to the more realistic representation of a real driving mission, both for its duration and for the presence of a road slope.

6.3.2 Results

The results for the corrected CO_2 production [g/km] are listed in Tab. 6.5.

As mentioned before, the initial ambient temperature is quite an important parameter for the simulation, since it is assumed that at the beginning of the driving mission the temperature of the battery is equal to the environmental one.

A specific comment deserves the simulation at ambient temperature equal to ϑ_{amb} = 10°C, where both TC2 and TC3 have no active cooling during the whole driving mission, as confirmed by the temperature trends reported in Fig. 6.13. Anyway, even without battery cooling the results are slightly higher than the ones obtained at ϑ_{amb} = 15°C. This behavior can be explained considering Fig. 3.10, where the battery cell internal resistance is shown versus the battery temperature. Accordingly, at low temperature the battery power losses increase, resulting in a lower battery electrical efficiency.

In the tests with the highest ambient temperature, i.e. ϑ_{amb} = 40°C, there are the largest differences among the controllers. As shown in the upper portion of

Table 6.5: CO_2 production [99].

TC	ϑ_{amb} [°C]						
	10	**15**	**20**	**25**	**30**	**35**	**40**
1	235.2	237.1	238.2	239.3	243.4	242.0	254.5
2	215.0	214.1	214.9	216.4	219.2	221.7	227.4
3	214.1	213.0	212.4	212.4	213.1	217.4	220.7

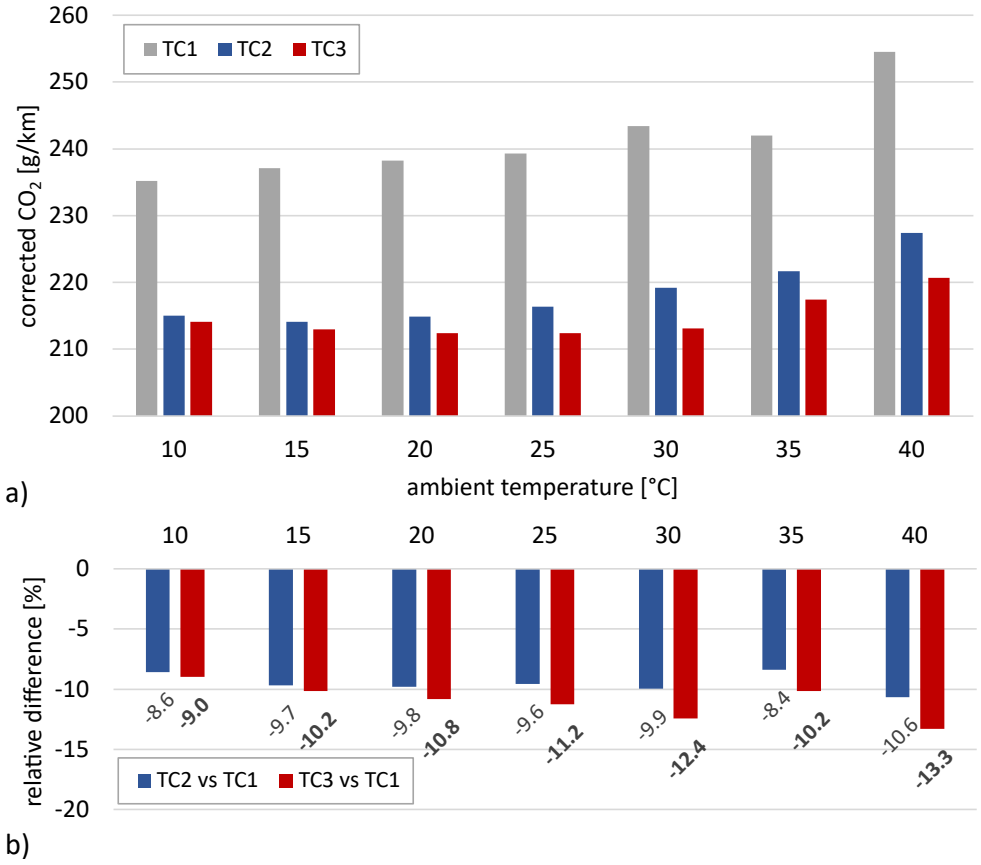

Figure 6.12: CO_2 production: a) corrected values and b)relative difference [99].

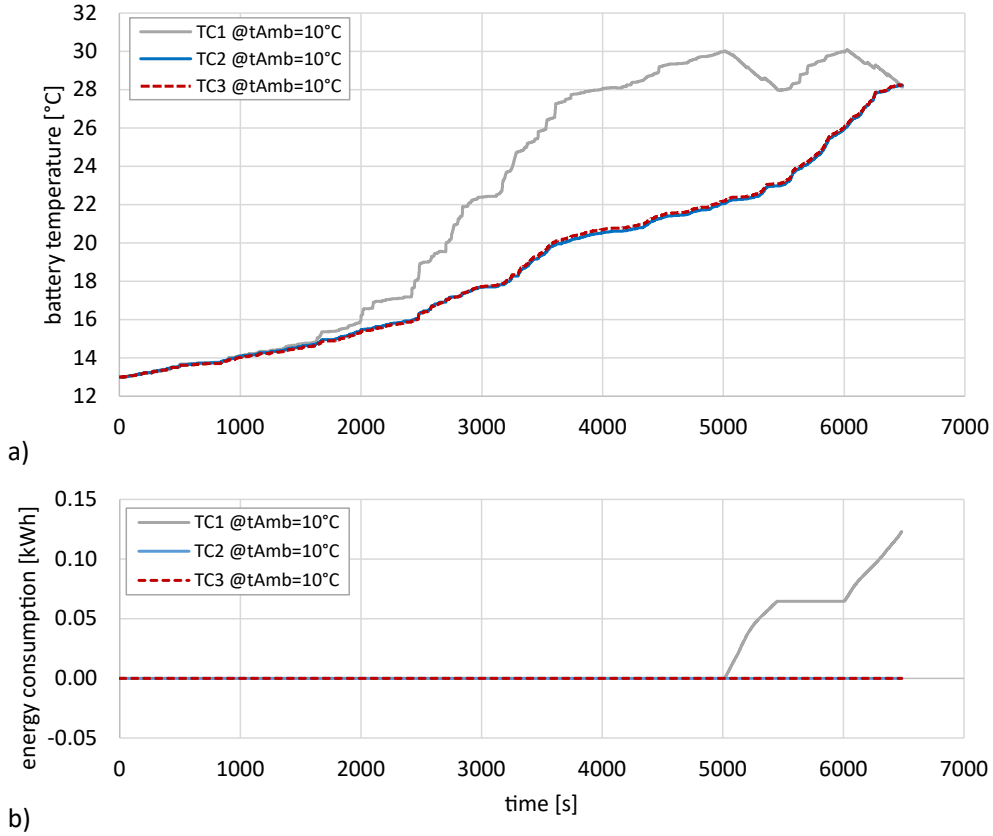

Figure 6.13: Comparison at ϑ_{amb} = 10°C: a) battery temperature and b) battery cooling energy consumption [99].

Fig. 6.14, the TC3 controller aims to keep the battery temperature always within the imposed limits ($\vartheta \in [\vartheta_{\min},\vartheta_{\max}] = [0,40]$°C), following the optimal control policy calculated with the combined DP algorithm. The other two controllers, instead, follow the rule-based approach for the thermal management. For TC1 and TC2 the main difference is the energy management implemented, that leads to a better fuel economy in TC2 with respect to TC1.

As a consequence of the different control policy, both for the thermal and the energy management, the electrical consumption for the battery cooling widely changes among the test-cases.

One may assess that the fuel economy improvement at ϑ_{amb} = 40°C of TC3 is mainly related to the fact that the battery temperature is always kept around the upper limitation, which actually minimizes the battery cooling. Even if this

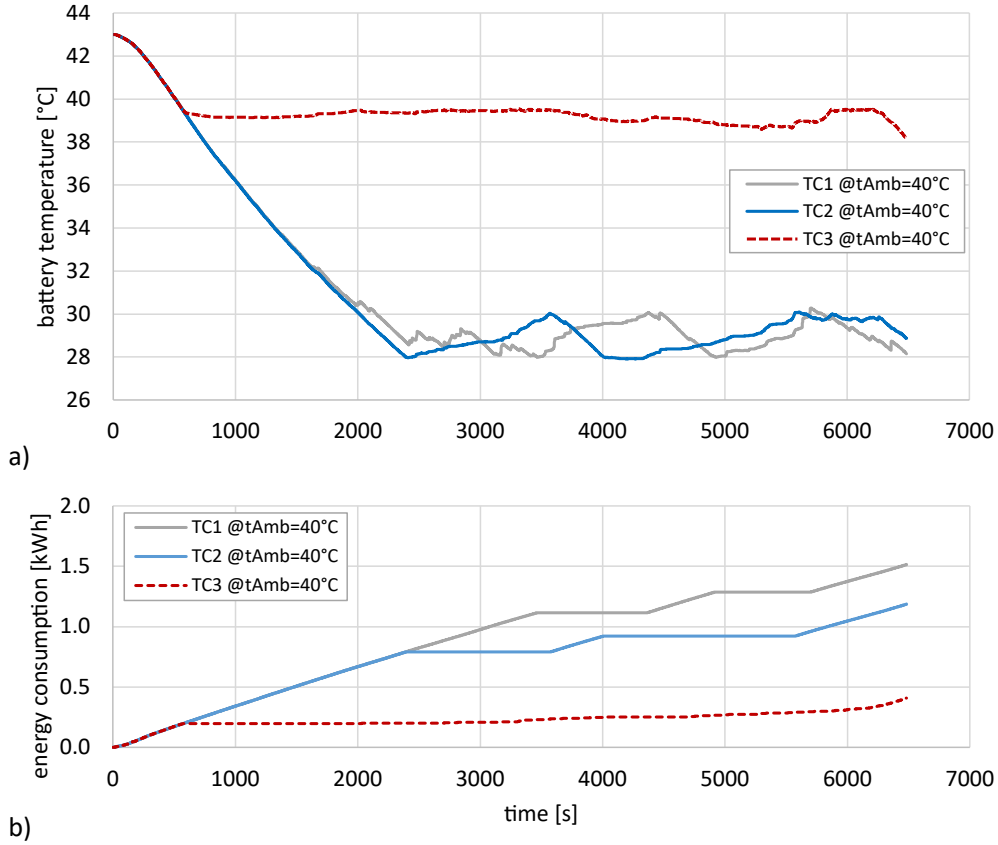

Figure 6.14: Comparison at ϑ_{amb} = 40°C: a) battery temperature and b) battery cooling energy consumption [99].

objection can be considered valid, the main reason why the optimization algorithm chooses to stay around the upper limit is again related to the characteristic of the battery. In fact, from Fig. 3.10 it can be noticed that the higher is the battery temperature, the lower is the internal resistance, which means less power losses. The minimum value is then around 40°C.

In general, referring to Tab. 6.5 and Fig. 6.12, for TC3 the fuel economy gain, with respect to the reference controller (TC1), increases with the ambient temperature.

The only exception to this trend is related to ambient temperature equal to ϑ_{amb} = 35°C. In this case, the gain is lower than the one obtained with ϑ_{amb} = 30°C and it is mainly related to the lower value of the global CO_2 production with the reference controller.

As shown in Fig. 6.15, at ϑ_{amb} = 35°C the engine is used less than at ϑ_{amb} = 30°C, respectively the 22.2% and the 23.2% of the mission total time, which is 6483 s. Instead, the global electrical energy usage is the same (same final state of charge), therefore the balance between the initial and final SOC is the same for both cases.

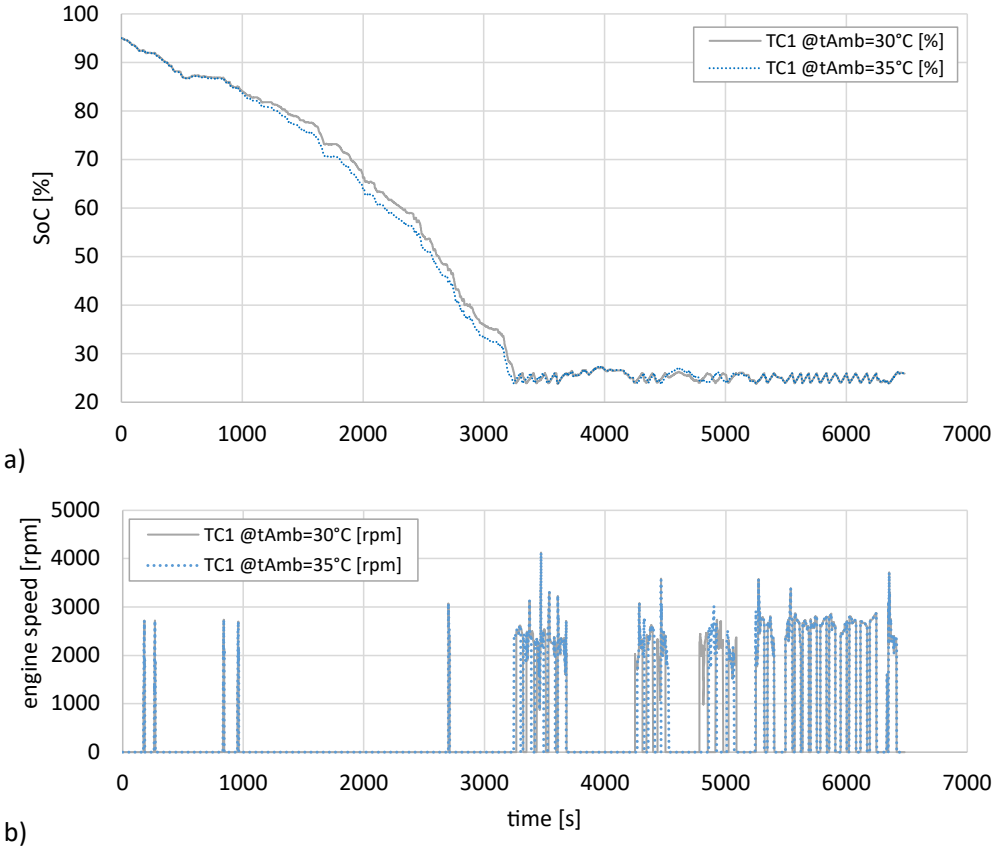

Figure 6.15: Comparison at ϑ_{amb} = [30,35]°C for Test Case 1: a) battery SoC and b) engine speed [99].

As a general comment on the obtained results, it can be said that considering the battery temperature in the energy management and, simultaneously, managing the battery cooling circuit according to the optimal control, leads to the largest fuel economy improvements.

Moreover, it seems also clear that the major contribution to the overall fuel saving is given by the energy management optimization (TC2), while the thermal management optimization contribution becomes relevant only for medium-high

ambient temperatures.

6.4 Adaptive-ECMS implementation at the c-HiL

In this section, the predictive functions and the Adaptive-ECMS discussed in Chapter 5 are tested at the connected-HiL, described in Chapter 4. In particular, in this test real-time navigation data are provided by the map service provider (MSP) via V2N connectivity and then sent to the HCU.

Since an energy assessment has been already performed in the previous section, from which the A-ECMS resulted more energy efficient than the baseline RBS strategy, no performance analysis will be here conducted. Moreover, as previously explained, the software of the supervisory controller modified at SiL level with the predictive structure of Fig. 5.3 and the sub-optimal control strategy, is seamlessly deployable in the target hardware (MicroAutoBox II) at HiL level. This ensures the same performance of the tested control policies at both simulation levels.

6.4.1 Issues related to on-line implementation

In this case, the only constraint to be satisfied is represented by the available computational power of the hardware to properly run the predictive functions. In fact, the sub-optimality of the ECMS allows this strategy to be real-time capable without further precautions. At this point, it is worth mentioning the Dynamic Programming, which requires all the driving mission to be known at the beginning of the cycle, or at least a relevant part of it in order to effectively provide a globally optimal control policy. Moreover, as discussed in Chapter 5.7, the numerical method applied for solving the optimal control problem implies a very high number of iterations to be performed by the backward algorithm, which would definitely lead to the impossibility of a real-time implementation of the developed strategy on board as it has been conceived. Thus, although the DP can be considered a valid starting point for future research activities due to the positive benefits obtained in Section 6.2, only the A-ECMS has been tested at the connected-HiL.

In general, the recursive nature of the prediction tasks makes these algorithms

to be particularly heavy from a computational point of view. In order to reduce as much as possible the required computational burden, the backward vehicle model has been properly designed with this aim. In fact, every time up-to-date navigation data are received, the for-loop in which the vehicle model has been implemented must perform N iterations within a single software time step, which is equal to $t_s = 10$ ms. Since a 1 s discretization has been chosen to avoid computational overload and, at the same time, to provide an accurate SoC prediction (as shown in the validation, Section 5.4.3), this means that the iterations number is equal to the period of time required for crossing the urban area. In other words, $N = \Delta t_Z = t_{f,Z} - t_{i,Z}$. Thus, the longer is the urban section of the trip, the higher is the required computational load. Nevertheless, during the debugging phase of the predictive functions at the HiL, it has been noticed that the limited performance of the target hardware (further detailed in [117]) led anyway to overclocking, thus exceeding the processors computational limits. To this aim, the number of iterations per time step of the BVM has been limited to $N_{\max} = 20$. Thus, if a single prediction task cannot be completed in a single time step, i.e. $N > N_{\max}$, it is then split in $\lceil N/N_{\max} \rceil$ multiple sequential sub-predictions. As a consequence, although the whole prediction takes more time to be completed (which is equal to $t_p = t_s \cdot \lceil N/N_{\max} \rceil$), with this solution the required real-time capability is guaranteed because the computational effort is preserved well below the hardware limit performance, while the accuracy of the prediction is not affected.

6.4.2 HiL testing with real-time navigation data

The trip shown in Fig. 6.16a, located in the Bologna metropolitan city, has been selected for the test. In order to properly test the developed A-ECMS, and since no zero-emission zone is currently in force in the chosen location, the one depicted in Fig. 6.16a has been reasonably generated.

As explained in Section 3.3.4, a target speed trace is required by the driver model to evaluate throttle and braking pedal signals. Since there is no traffic environment simulator at the HiL that would allow the vehicle to be driven by an independent driver, a target speed profile has been generated before the test by means of the speed profile prediction algorithm at the c-HiL. This choice is

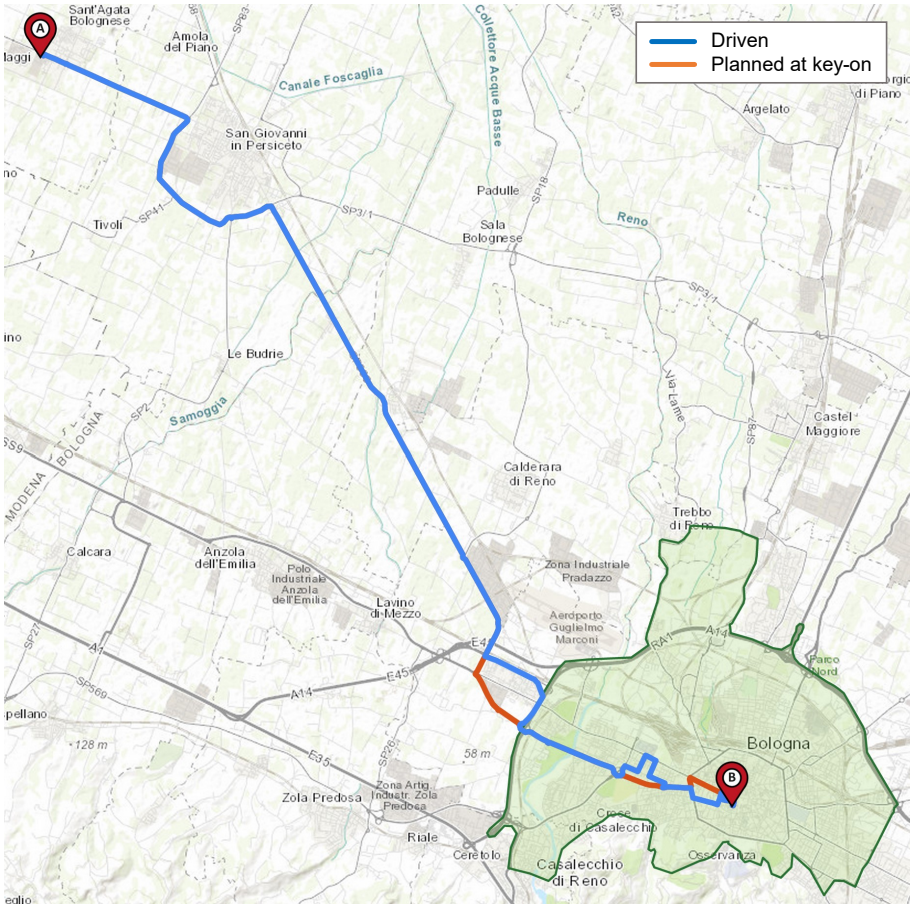

(a) Overview.

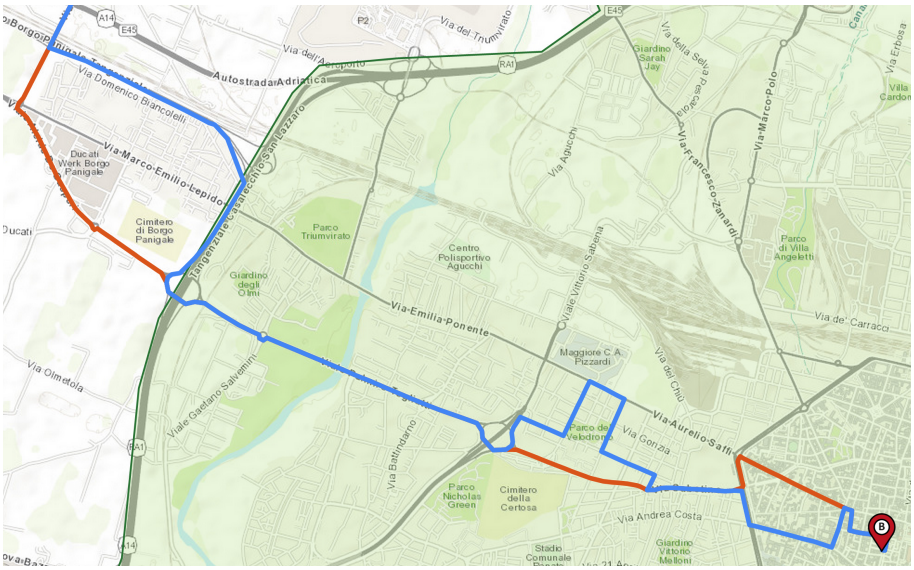

(b) Particular: ZEZ.

Figure 6.16: Comparison between the driven route and the one planned at key-on.

justified by the following reason:

- real navigation data provided by the map service provider have been used since they are always up-to-date, and data variability is taken into account, such as traffic flow evolving over time;

- the speed profile prediction is inherently stochastic
  in fact, as explained in Section 5.3, the SPP algorithm is able to reproduce probabilistic events such as the ones related to the traffic flow (by means of the oscillating MAS) or the traffic lights scheduling (by means of stopover probabilities, affected by traffic conditions, as well).

Thus, for the given scenario, the real navigation data and the resulting speed trace for target speed generation at the c-HiL are depicted in Fig. 6.17. Even in this case, it can be noticed that the legal speed limits represent an upper boundary conditions for the speed profile, while intense traffic leads to MAS reductions. The zero emission zone is represented by the green-filled box. Moreover, since city entrance and exit positions are not provided by the MSP (because no ZEZ exists for the given scenario), they have been calculated via intersection of the given route with the ZEZ map boundary line, that has been temporarily stored within the Telecommunication Control Unit (TeCU) for this purpose.

At this point, the A-ECMS testing at the c-HiL can be performed. As explained in Section 5.4.1, the first query for navigation info to the MSP is made at the beginning of the driving mission, i.e. at key-on (1), when the driver is supposed to select the destination of the trip via HMI. Thus, data are requested by the TeCU and, when received from the MSP, they are then sent to HCU via CAN bus by means of the the Central Gateway (CG). The navigation data received by the HCU at key-on during the test are listed in Tab. 6.6.

Differently from the data sent by the MSP (Tab. 4.1), latitudes and longitudes of the trip are not included because they are not required inputs by the predictive functions, and the slope has been calculated from altitude profile and path coordinates by the CG during data pre-processing. These routing data received at key-on and the predicted speed profile for the entire trip are shown in Fig. 6.18. Compared to Fig. 6.17 and considering Fig. 6.16b, it can be noticed that a slightly

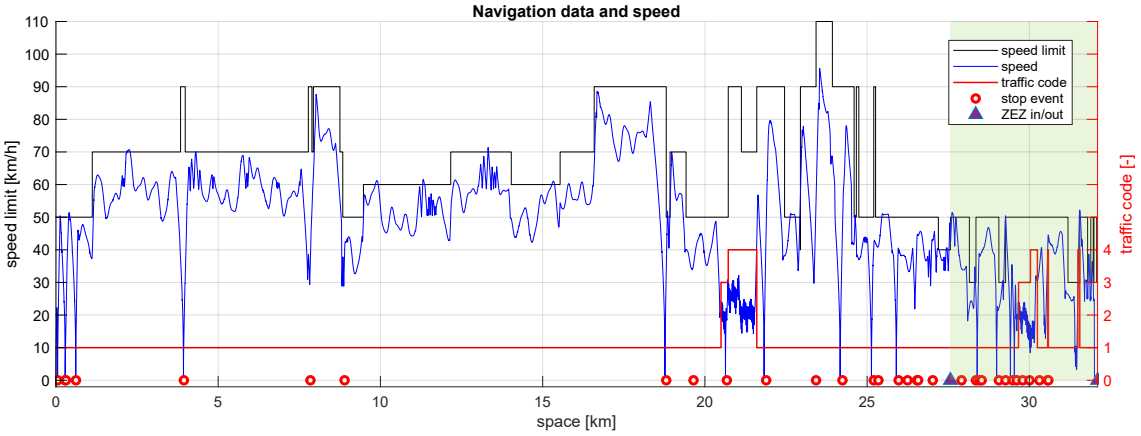

Figure 6.17: Graphical representation of the real-time navigation data received before the test for generating the target speed (blue).

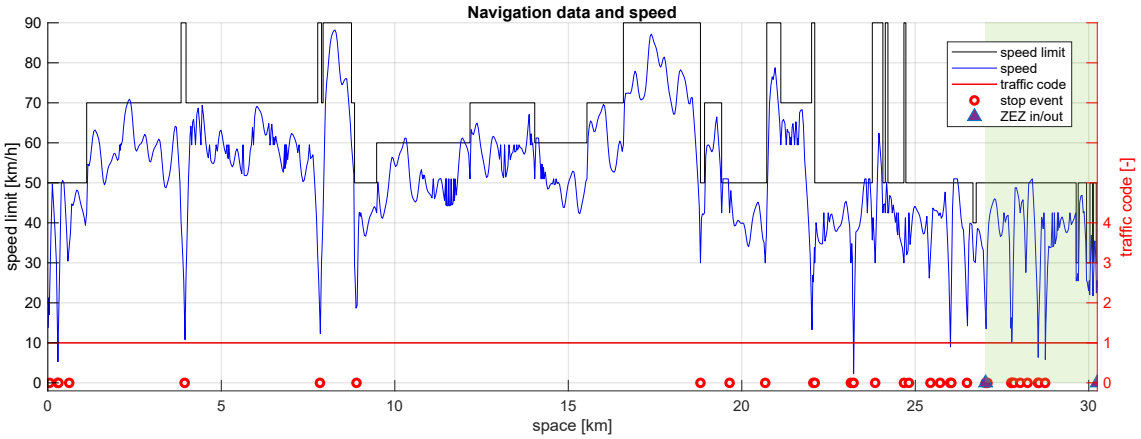

Figure 6.18: Graphical representation of the real-time navigation data received during the test at key-on (first prediction) and predicted speed (blue)

Table 6.6: Real-time navigation data received by the map service provider at key-on (first prediction).

#	speed [km/h]	slope [%]	segment [m]	stop event [-]	stop event position [m]	traffic code [-]	traffic code segment [m]	ZEZ in/out position [m]
1	50	0	306	4	52	1	30245	27028
2	50	1	350	1	287			30245
3	50	0	1120	1	306			
4	70	0	2076	2	617			
5	70	1	2118	2	3944			
6	70	0	3841	2	7843			
7	90	0	3984	2	8896			
8	70	0	4053	2	18809			
9	70	-1	4146	1	19649			
10	70	-2	4256	2	20676			
11	70	-1	4413	1	22062			
12	70	0	4661	2	22103			
13	70	2	4851	2	23144			
14	70	0	5164	1	23221			
15	70	-2	5215	2	23844			
16	70	-1	5625	2	24673			
17	70	0	5869	1	24816			
18	70	-1	5927	1	25438			
19	70	0	6404	1	25715			
20	70	3	6413	1	26006			
21	70	2	6497	1	26039			
22	70	1	6533	2	26491			
23	70	0	6825	1	27028			
24	70	-1	6850	1	27079			
25	70	-2	6876	1	27768			
26	70	-1	7241	1	27785			
27	70	1	7538	1	27841			
28	70	0	7779	1	28024			
29	90	0	7889	1	28236			
30	70	0	7934	1	28537			
31	90	0	8752	2	28560			
32	70	0	8840	1	28743			
33	50	0	8972					
...	...	...	...					
135	30	5	30236					
136	30	-1	30245					

different, shorter trip has been defined by the MSP for the same starting and arrival points because of the different traffic conditions between the two scenarios.

It is now possible to predict the vehicle speed and the battery SoC among the given urban horizon. To this aim, the bit signal shown in Fig. 6.19 triggers the SPP and BVM. Then, the Soc target is evaluated as in Eq. (5.10) by the ZEZ function and it is fed into the A-ECMS as an input parameter. In Fig. 6.19, the charge-blended mode of the sub-optimal strategy can be noticed, aimed at following the reference SoC. In order to produce an effective test, since the target SoC ξ_t is relatively low (due to the short urban trip), the initial condition $\xi_0 < \xi_t$ has been set, analogously to the test cases TC1 and TC2 presented in Section 6.2. Even in this scenario, the electric energy stored in the REES at the beginning of the ZEZ is high enough to ensure the all-electric drive mode along the whole city passage ($\xi_{f,Z} > \xi_{\min} = 20\%$).

In Fig. 6.19 the HCU turnaround time (TAT) is also depicted, which represents the amount of time taken to complete a single calculation process. As it has been anticipated, to avoid computational overflows, it shall be always $t_{ta} < t_s = 10$ ms. As it can be seen, the nominal TAT is shown to be around 4 ms, except when the predictive functions are triggered, resulting in computational load peaks. The amplitude of such peaks, and thus the computational effort, reduces over time because the SPP algorithm has to manage a lower quantity of navigation data, since the vehicle is approaching the given destination.

Multiple predictive tasks occur when up-to-date navigation are available. This could happen because different rerouting events are triggered by the MSP via GPS signal, i.e. when the driver takes the wrong direction or intentionally stops following the suggested route. In this case, the latter is manually reproduced in order to test the robustness of the predictive functions. In fact, since no traffic simulation environment, including an independent driver, has been implemented at the HiL, the GPS signal is generated by interpolation of the latitude and longitude coordinates as a function of the traveled distance. These coordinates are the same provided by the MSP for generating the trip used for target speed evaluation. Since this trip is established before the test and it is not subjected to any modification, it is as if the driver would follow the same driving path for the whole driving mission. Therefore, if slightly different trips are generated by the MSP during the

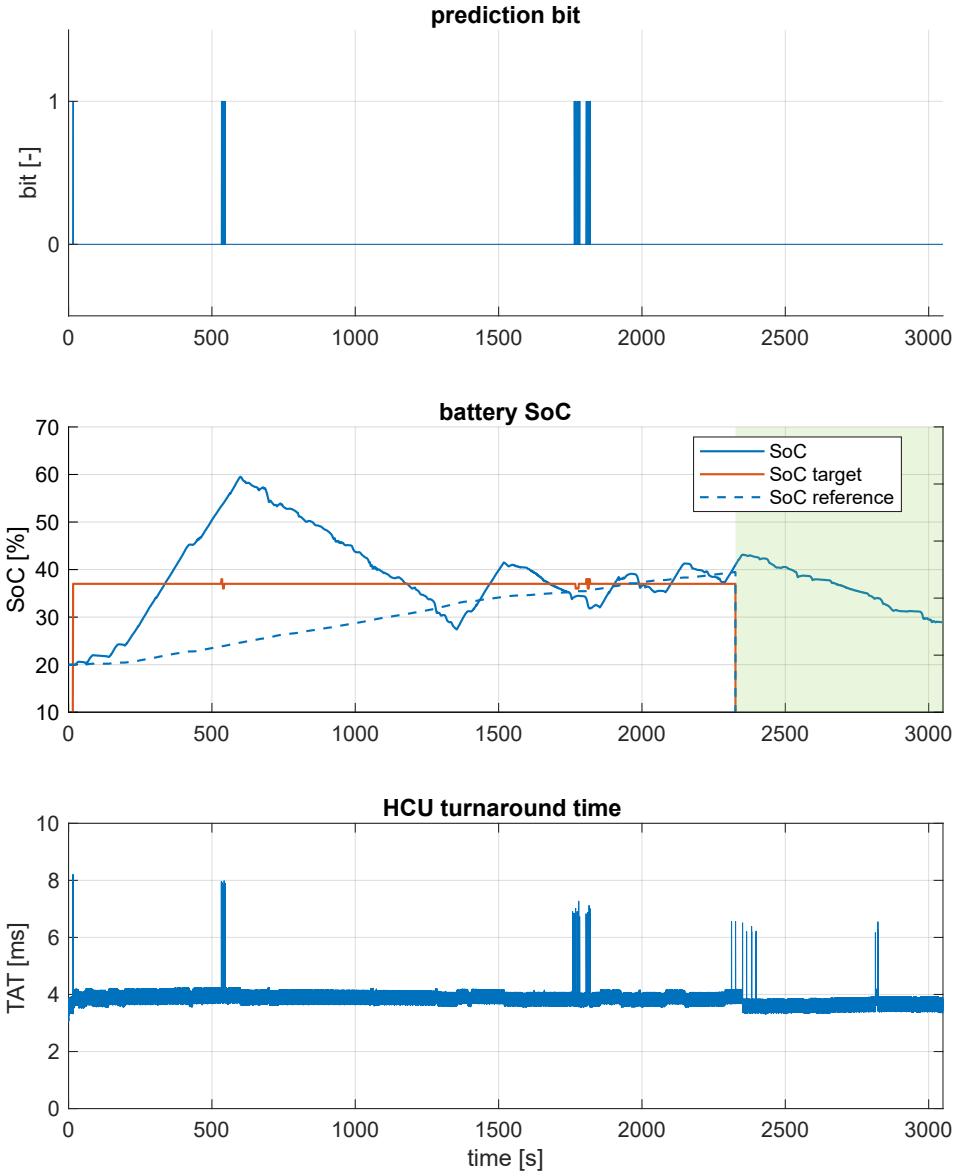

Figure 6.19: Adaptive-ECMS implementation at the connected-HiL.

test because of the variability of real-time traffic conditions, this would result in rerouting events. In this case, the MSP recalculates the trip with the actual GPS position as the new starting point, while the arrival one remains unchanged. This situation is properly handled by the supervisory controller because the SPP is able to predict up-to-date speed traces, as shown in Fig. 6.20. For the sake of simplicity, only the predicted speed trace for the first and the last rerouting are presented.

Since new navigation data are received every time a rerouting is performed, up-to-date traffic codes are available, as well. As a consequence, traffic density variation over time can be noticed during the test. At the first rerouting, no relevant traffic density is present at the end of the trip, within the urban area (about $t = 2800$ s). Considering Fig. 6.18 and Tab. 6.6, this is true for the first prediction, as well, where the traffic code is always equal to $c = 1$. However, at the last rerouting, since a change in traffic density happened during the driving mission, the predicted speed trace in that section is lower than the first case. This is caused by a reduction of the reference MAS affected by the code weight CW, and then the traffic code c. At each rerouting, the BVM is triggered, as well, and the target SoC is evaluated. As a consequence, small variations in the latter parameter can be observed in Fig. 6.19. They are not well appreciable because the up-to-date trip, in particular the traffic density, has only slightly changed since the last data refreshing, without strongly impacting the prediction.

The implementation at the connected HiL of the Adaptive-ECMS strategy for ZEZ handling has thus been demonstrated, showing that the prediction-based energy management functions developed during the PhD research activity can be directly transferred on-board the vehicle. This allows to take advantage of already available information (such as navigation data) to further improve the efficiency of the powertrain, in particular within urban environments in which specific limitations for air pollution reduction are in force.

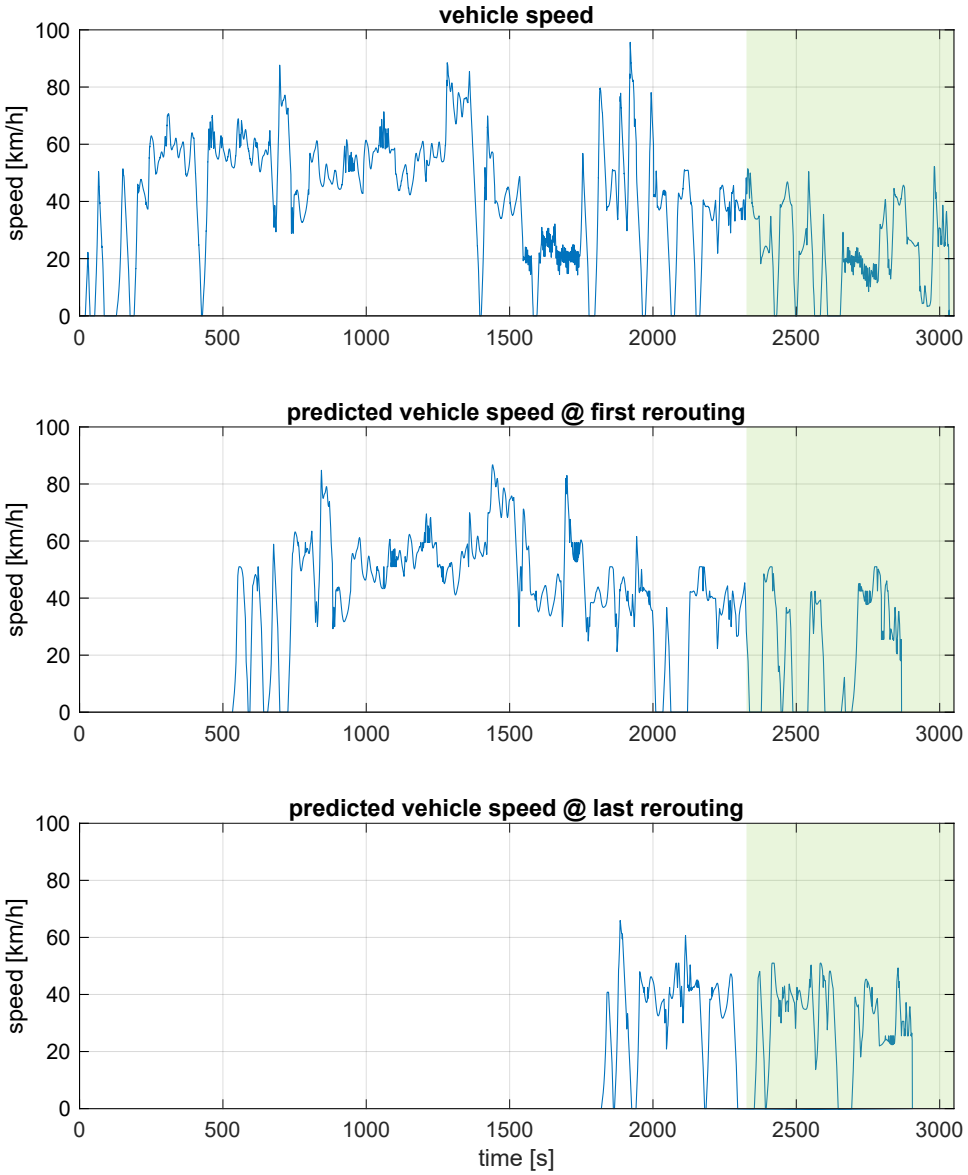

Figure 6.20: Effect of the rerouting on the speed profile prediction.

Chapter 7

Conclusion

Hybrid electric vehicles (HEVs) are a well-established technology to face the global warming and air pollution crisis in the transportation sector. At the same time, the spreading of novel technologies, such as advanced driving assistance systems (ADAS), and the availability for the vehicle to exchange data with the surrounding environment (vehicle-to-everything) are leading the way to the concept of *smart mobility*. It can be intended as a new way of organizing mobility, with important social and cultural implications especially in urban contexts, where zero-emission zones (ZEZ) have been proved to be a promising solution for reducing the vehicles impact on urban air quality.

The objective of this dissertation is to provide advanced control strategies for hybrid powertrains in order to minimize the global energy consumption of the vehicle. The presented control policies, namely the adaptive equivalent consumption minimization strategy, or adaptive-ECMS, and the dynamic programming, lie on the concept of *predictivity*. In other word, the prediction of future working conditions of the powertrain, which is the core part of this work.

In fact, with regards to the adaptive-ECMS [98], the developed supervisory controller architecture is focused on predictive functions which rely on a backward vehicle model which is able to reconstruct the battery state of charge behavior over the ZEZ using navigation data. In this way, it is then possible to prepare the vehicle from an energy management point of view through adaptive-ECMS to ensure all-electric driving mode in urban areas. It has been shown that remarkable

improvements in terms of CO_2 reduction can be obtained, while preventing engine emissions within city centers at the same time.

On the other hand, dynamic programming is able to provide the optimal solution to the energy management problem of HEVs. With regards to the works proposed in literature, and with the aim of enhancing HEVs control, the novel contribution is here represented by the combined, simultaneous optimization of vehicle energy and battery thermal management [99]. In particular, the implementation of parameters like battery temperature and battery cooling circuit control signal led to a CO_2 production lower than the one resulting not only from the baseline rule-based strategy, but also from a dynamic programming based only on energy optimization.

In order to develop, test and asses the energetic effectiveness of the mentioned control strategies, simulation and testing environments have been set up during this work. Therefore, high importance has been given to the control-oriented modeling of the hybrid powertrain under test, including battery electrical and thermal models and a realistic battery management system. With regards to the software of the supervisory controller, already developed by the industrial partner, it has been modified in order to implement the predictive functions and the Adaptive-ECMS, resulting in a highly-detailed Software-in-the-Loop vehicle model. Moreover, a Hardware-in-the-Loop (HiL) system with integrated connectivity has been presented [100]. On one hand, it provides higher flexibility due to the possibility to test different types of predictive functions (long and short horizon). On the other hand, it grants higher reliability, as both the hardware and the software are the same as those implemented on the vehicle, allowing seamless functions implementation on-board once validated at the HiL.

Future works regarding the research project carried out include the testing of the adaptive-ECMS and the predictive function at the HiL in order to further asses the benefits of this approach toward in-vehicle implementation, which is a less demanding task with respect to dynamic programming since the sub-optimal solution is inherently provided at each calculation step. In fact, in order to overcome the high computational load required by dynamic programming, a possible enhancement to on-board implementation could be represented by the integration of the optimization algorithm in a model predictive control, in order to

consider shorter horizons, being able to perform energy and thermal management optimization in real-time, for predictive driving applications. Following improvements could focus on cloud computing-based control strategies and predictive functions in order to reduce the workload of the supervisory controller and, at the same time, increasing the horizon of the prediction.

Bibliography

[1] H. Ritchie and M. Roser, "CO_2 and Greenhouse Gas Emissions," *Our World in Data*, 2020. [Online]. Available: https://ourworldindata.org/co2-and-other-greenhouse-gas-emissions.

[2] European Commission, "Regulation (EU) 2019/631 of the European Parliament and of the Council of 17 April 2019 setting CO_2 emission performance standards for new passenger cars and for new light commercial vehicles, and repealing Regulations (EC) No 443/2009 and (EU) No 510/2011," Regulation (EU) 2019/631, 2019. [Online]. Available: https://eur-lex.europa.eu/legal-content/EN/ALL/?uri=CELEX%3A32019R0631.

[3] Z. Yang and A. Bandivadekar, "Light-duty vehicle greenhouse gas and fuel economy standards," International Council on Clean Transportation (ICCT), 2017, p. 36. [Online]. Available: https://theicct.org/sites/default/files/publications/2017-Global-LDV-Standards-Update_ICCT-Report_23062017_vF.pdf.

[4] P. Mock, "Real-Driving Emissions test procedure for exhaust gas pollutant emissions of cars and light commercial vehicles in Europe," International Council On Clean Transportation (ICCT), 2017. [Online]. Available: https://theicct.org/publications/real-driving-emissions-test-procedure-exhaust-gas-pollutant-emissions-cars-and-light.

[5] ——, "CO_2 emission standards for passenger cars and light-commercial vehicles in the European Union," International Council on Clean Transportation (ICCT), 2019, p. 9. [Online]. Available: https://theicct.org/sites/default/files/publications/EU-LCV-CO2-2030_ICCTupdate_20190123.pdf.

[6] X. Mosquet, A. Dinger, G. Xu, M. Andersen, *et al.*, "The Electric Car Tipping Point," Boston Consulting Group (BCG), 2018. [Online]. Available: https://www.bcg.com/publications/2018/electric-car-tipping-point.

[7] P. Slowik, N. Pavlenko, and N. P. Lutsey, "Assessment of next-generation electric vehicle technologies," International Council on Clean Transportation (ICCT), 2016. [Online]. Available: http://rgdoi.net/10.13140/RG.2.2.17530.49601.

[8] W. Liu, *Hybrid electric vehicle system modeling and control*, 2nd edition, ser. Automotive series. John Wiley & Sons, 2017, 1 p., ISBN 978-1-119-27894-8.

[9] C. Mi and M. A. Masrur, *Hybrid Electric Vehicles: Principles and Applications with Practical Perspectives*. John Wiley & Sons, 2017, 597 pp., ISBN 978-1-118-97056-0.

[10] M. A. Hannan, F. A. Azidin, and A. Mohamed, "Hybrid electric vehicles and their challenges: A review," *Renewable and Sustainable Energy Reviews*, vol. 29, pp. 135–150, 2014, ISSN 1364-0321. doi: 10.1016/j.rser.2013.08.097.

[11] K. V. Singh, H. O. Bansal, and D. Singh, "A comprehensive review on hybrid electric vehicles: Architectures and components," *J. Mod. Transport.*, vol. 27, no. 2, pp. 77–107, 2019, ISSN 2196-0577. doi: 10.1007/s40534-019-0184-3.

[12] P. Harrop, "The next 20 years: Powertrains come and go: When, why, what next?" FPC2017 - Future Powertrain Conference, 2017. [Online]. Available: https://futurepowertrains.co.uk/wp-content/uploads/2017/03/peter-harrop.pdf.

[13] NHTSA. "U.s. department of transportation releases policy on automated vehicle development." (2019), [Online]. Available: https://www.transportation.gov/briefing-room/us-department-transportation-releases-policy-automated-vehicle-development.

[14] ——, "Automated vehicles for safety." (2021), [Online]. Available: https://www.nhtsa.gov/technology-innovation/automated-vehicles-safety.

[15] I. Campero-Jurado, J. Q. Gomez, O. D. Vargas-Buitrón, F. R. Trejo-Macotela, *et al.*, "Embedded system based on IoT and V2X for Smart Cities," *International Journal of Combinatorial Optimization Problems and Informatics*, vol. 10, no. 3, pp. 50–58, 2019, ISSN 2007-1558.

[16] R. Shrestha, S. Y. Nam, R. Bajracharya, and S. Kim, "Evolution of V2X Communication and Integration of Blockchain for Security Enhancements," *Electronics*, vol. 9, no. 9, p. 1338, 2020. doi: 10.3390/electronics9091338.

[17] F. Outay, F. Kamoun, F. Kaisser, D. Alterri, *et al.*, "V2V and V2I Communications for Traffic Safety and CO_2 Emission Reduction: A Performance Evaluation," *Procedia Computer Science*, vol. 151, pp. 353–360, 2019, ISSN 1877-0509. doi: 10.1016/j.procs.2019.04.049.

[18] W. He, H. Li, X. Zhi, X. Li, *et al.*, "Overview of V2V and V2I Wireless Communication for Cooperative Vehicle Infrastructure Systems," *2019 IEEE 4th Advanced Information Technology, Electronic and Automation Control Conference (IAEAC)*, vol. 1, 2019, pp. 127–134. doi: 10.1109/IAEAC47372.2019.8997786.

[19] K. Kiela, V. Barzdenas, M. Jurgo, V. Macaitis, *et al.*, "Review of V2X–IoT Standards and Frameworks for ITS Applications," *Applied Sciences*, vol. 10, no. 12, p. 4314, 2020, ISSN 2076-3417. doi: 10.3390/app10124314.

[20] European Commission, *European Urban Mobility: Policy Context*. Publications Office of the European Union, 2017, ISBN 978-92-79-57527-3. doi: 10.2832/827766.

[21] ETSI, "Technical Specification Group Services and System Aspects," Technical Report 3GPP TS 33.185 V14.1.0, 2020. [Online]. Available: https://portal.3gpp.org/desktopmodules/Specifications/SpecificationDetails.aspx?specificationId=3618.

[22] C. Ress, A. Etemad, D. Kuck, and J. Requejo, "Electronic horizon - providing digital map data for adas applications," *Proceedings of the 2nd International Workshop on Intelligent Vehicle Control Systems - Volume 1: IVCS, (ICINCO 2008)*, INSTICC, vol. 1, SciTePress, 2008, pp. 40–49, ISBN 978-989-8111-34-0. doi: 10.5220/0001508000400049.

[23] C. Ress, D. Balzer, A. Bracht, S. Durekovic, *et al.*, "ADASIS Protocol for advanced in-vehicle applications," 2008. [Online]. Available: https://www.researchgate.net/publication/228880192_Adasis_protocol_for_advanced_in-vehicle_applications.

[24] ADASIS. "New advanced driver assistance systems specification provides impactful and more accurate features to support automated driving." (2020), [Online]. Available: https://adasis.org/2020/11/26/new-advanced-driver-assistance-systems-specification-provides-impactful-and-more-accurate-features-to-support-automated-driving/.

[25] On-Road Automated Driving (ORAD) committee, *Taxonomy and definitions for terms related to driving automation systems for on-road motor vehicles*, SAE International, 2021. doi: 10.4271/J3016_202104.

[26] C. Benevolo, R. P. Dameri, and B. D'Auria, "Smart Mobility in Smart City," *Empowering Organizations*, ser. Lecture Notes in Information Systems and Organisation, Springer International Publishing, 2016, pp. 13–28, ISBN 978-3-319-23784-8. doi: 10.1007/978-3-319-23784-8_2.

[27] M. Pesaresi, M. Melchiorri, A. Siragusa, and T. Kemper, "Atlas of the Human Planet 2016: Mapping Human Presence on Earth with the Global Human Settlement Layer," EUR 28116 EN, 2016. doi: 10.2788/889483.

[28] H. Ritchie and M. Roser, "Urbanization," *Our World in Data*, 2018. [Online]. Available: https://ourworldindata.org/urbanization.

[29] European Commission, *Sustainable Urban Mobility: European Policy, Practice and Solutions*. Publications Office of the European Union, 2017, ISBN 978-92-79-66651-3. doi: 10.2832/51274.

[30] J. Müller and Y. Le Petit, "Low-Emission Zones are a success - but they must now move to zero-emission mobility," 2019. [Online]. Available: https://www.transportenvironment.org/sites/te/files/publications/2019_09_Briefing_LEZ-ZEZ_final.pdf.

[31] "Ultra low emission zone," Transport for London. (), [Online]. Available: https://www.tfl.gov.uk/modes/driving/ultra-low-emission-zone (visited on 2021).

[32] "Central london ultra low emission zone - six month report," 2019, p. 41. [Online]. Available: https://www.london.gov.uk/sites/default/files/ulez_six_month_evaluation_report_final_oct.pdf.

[33] L. Guzzella and A. Sciarretta, *Vehicle Propulsion Systems: Introduction to Modeling and Optimization*, 3rd ed. Springer International Publishing, 2013, ISBN 978-3-642-35912-5. doi: 10.1007/978-3-642-35913-2.

[34] T. J. Böhme and B. Frank, *Hybrid Systems, Optimal Control and Hybrid Vehicles: Theory, Methods and Applications*, ser. Advances in Industrial Control Series. Springer International Publishing, 2017, ISBN 978-3-319-51315-7. doi: 10.1007/978-3-319-51317-1.

[35] P. Caratozzolo, M. Serra, and J. Riera, "Energy management strategies for hybrid electric vehicles," *IEEE International Electric Machines and Drives Conference, 2003. IEMDC'03.*, vol. 1, 2003, pp. 241–248. doi: 10.1109/IEMDC.2003.1211270.

[36] X. He, M. Parten, and T. Maxwell, "Energy Management Strategies for a Hybrid Electric Vehicle," *2005 IEEE Vehicle Power and Propulsion Conference*, 2005, pp. 536–540. doi: 10.1109/VPPC.2005.1554610.

[37] J. Gonder and T. Markel, "Energy Management Strategies for Plug-In Hybrid Electric Vehicles," SAE Technical Paper 2007-01-0290, 2007. doi: 10.4271/2007-01-0290.

[38] M. F. M. Sabri, K. A. Danapalasingam, and M. F. Rahmat, "A review on hybrid electric vehicles architecture and energy management strategies," *Renewable and Sustainable Energy Reviews*, vol. 53, pp. 1433–1442, 2016, ISSN 1364-0321. doi: 10.1016/j.rser.2015.09.036.

[39] P. Pisu and G. Rizzoni, "A Comparative Study Of Supervisory Control Strategies for Hybrid Electric Vehicles," *IEEE Transactions on Control Systems Technology*, vol. 15, no. 3, pp. 506–518, 2007, ISSN 1558-0865. doi: 10.1109/TCST.2007.894649.

[40] L. Serrao, S. Onori, and G. Rizzoni, "A Comparative Analysis of Energy Management Strategies for Hybrid Electric Vehicles," *Journal of Dynamic Systems, Measurement, and Control*, vol. 133, no. 3, 2011, ISSN 0022-0434. doi: 10.1115/1.4003267.

[41] A. Ali and D. Söffker, "Towards Optimal Power Management of Hybrid Electric Vehicles in Real-Time: A Review on Methods, Challenges, and State-Of-The-Art Solutions," *Energies*, vol. 11, no. 3, p. 476, 2018, ISSN 1996-1073. doi: 10.3390/en11030476.

[42] P. Zhang, F. Yan, and C. Du, "A comprehensive analysis of energy management strategies for hybrid electric vehicles based on bibliometrics," *Renewable and Sustainable Energy Reviews*, vol. 48, pp. 88–104, 2015, ISSN 1364-0321. doi: 10.1016/j.rser.2015.03.093.

[43] F. Zhang, L. Wang, S. Coskun, H. Pang, *et al.*, "Energy Management Strategies for Hybrid Electric Vehicles: Review, Classification, Comparison, and Outlook," *Energies*, vol. 13, no. 13, p. 3352, 2020. doi: 10.3390/en13133352.

[44] N. J. Schouten, M. A. Salman, and N. A. Kheir, "Energy management strategies for parallel hybrid vehicles using fuzzy logic," *Control Engineering Practice*, Automotive Systems, vol. 11, no. 2, pp. 171–177, 2003, ISSN 0967-0661. doi: 10.1016/S0967-0661(02)00072-2.

[45] V. Navale and T. C. Havens, "Fuzzy logic controller for energy management of power split hybrid electrical vehicle transmission," *2014 IEEE International Conference on Fuzzy Systems (FUZZ-IEEE)*, 2014, pp. 940–947. doi: 10.1109/FUZZ-IEEE.2014.6891785.

[46] T. Hofman, M. Steinbuch, R. Druten, and A. Serrarens, "Rule-based energy management strategies for hybrid vehicles," *International Journal of Electric and Hybrid Vehicles*, vol. 1, no. 1, 2007. doi: 10.1504/IJEHV.2007.014448.

[47] T. Hofman, M. Steinbuch, R. M. van Druten, and A. F. A. Serrarens, "Rule-Based Energy Management Strategies For Hybrid Vehicle Drivetrains: A Fundamental Approach In Reducing Computation Time," *IFAC Proceedings Volumes*, 4th IFAC Symposium on Mechatronic Systems, vol. 39, no. 16, pp. 740–745, 2006, ISSN 1474-6670. doi: 10.3182/20060912-3-DE-2911.00128.

[48] D. Bianchi, L. Rolando, L. Serrao, S. Onori, *et al.*, "A Rule-Based Strategy for a Series/Parallel Hybrid Electric Vehicle: An Approach Based on Dynamic Programming," *ASME 2010 Dynamic Systems and Control Conference, Volume 1*, Cambridge, Massachusetts, USA, 2010, pp. 507–514, ISBN 978-0-7918-4417-5. doi: 10.1115/DSCC2010-4233.

[49] T. J. Boehme, M. Schori, H. Rabba, and M. Schultalbers, "Analytical Calibration of Map-Based Energy Managements of Parallel Hybrid Vehicles," SAE Technical Paper 2014-01-1902, 2014. doi: 10.4271/2014-01-1902.

[50] S. Onori, L. Serrao, and G. Rizzoni, *Hybrid Electric Vehicles - Energy Managament Strategies*, ser. SpringerBriefs in Electrical and Computer Engineering. Springer London, 2016, ISBN 978-1-4471-6779-2978-1-4471-6781-5. doi: 10.1007/978-1-4471-6781-5.

[51] Y. Huang, H. Wang, A. Khajepour, H. He, *et al.*, "Model predictive control power management strategies for HEVs: A review," *Journal of Power Sources*, vol. 341, pp. 91–106, 2017, ISSN 03787753. doi: 10.1016/j.jpowsour.2016.11.106.

[52] L. Serrao, S. Onori, and G. Rizzoni, "ECMS as a realization of pontryagin's minimum principle for HEV control," *2009 American Control Conference*, 2009, pp. 3964–3969. doi: 10.1109/ACC.2009.5160628.

[53] G. Paganelli, "Conception et commande d'une chaîne de traction pour véhicule hybride parallèle thermique et électrique," Doctoral thesis, Université de Valenciennes et du Hainaut-Cambrésis, Valenciennes, 1999.

[54] G. Paganelli, G. Ercole, A. Brahma, Y. Guezennec, *et al.*, "General supervisory control policy for the energy optimization of charge-sustaining hybrid electric vehicles," *JSAE Review*, vol. 22, pp. 511–518, 2001. doi: 10.1016/S0389-4304(01)00138-2.

[55] G. Paganelli, S. Delprat, T. Guerra, J. Rimaux, *et al.*, "Equivalent consumption minimization strategy for parallel hybrid powertrains," *Vehicular Technology Conference. IEEE 55th Vehicular Technology Conference. VTC Spring 2002 (Cat. No.02CH37367)*, vol. 4, 2002, pp. 2076–2081. doi: 10.1109/VTC.2002.1002989.

[56] F. R. Salmasi, "Control Strategies for Hybrid Electric Vehicles: Evolution, Classification, Comparison, and Future Trends," *IEEE Transactions on Vehicular Technology*, vol. 56, no. 5, pp. 2393–2404, 2007. doi: 10.1109/TVT.2007.899933.

[57] G. Rizzoni and S. Onori, "Energy Management of Hybrid Electric Vehicles: 15 years of development at the Ohio State University," *Oil Gas Sci. Technol. – Rev. IFP Energies nouvelles*, vol. 70, no. 1, pp. 41–54, 2015. doi: 10.2516/ogst/2014006.

[58] G. Paganelli, S. Delprat, T.-M. Guerra, J. Rimaux, *et al.*, "Equivalent consumption minimization strategy for parallel hybrid powertrains," *IEEE 55th Vehicular Technology Conference*, vol. 4, 2002, pp. 2076–2081, ISBN 978-0-7803-7484-3. doi: 10.1109/VTC.2002.1002989.

[59] A. Cerofolini, "Optimal Supervisory Control of Hybrid Vehicles," Doctoral thesis, University of Bologna, 2014. doi: 10.6092/unibo/amsdottorato/6357. [Online]. Available: https://amsdottorato.unibo.it/6357/.

[60] D. E. Kirk, *Optimal Control Theory: An Introduction*. Courier Corporation, 2017, ISBN 978-0-486-43484-1.

[61] Y. Yu, J. Jiang, P. Wang, J. Li, *et al.*, "A-EMCS for PHEV based on real-time driving cycle prediction and personalized travel characteristics," *MBE*, vol. 17, no. 6, pp. 6310–6341, 2020. doi: 10.3934/mbe.2020333.

[62] Z. Lei, D. Qin, L. Hou, J. Peng, *et al.*, "An adaptive equivalent consumption minimization strategy for plug-in hybrid electric vehicles based on traffic information," *Energy*, vol. 190, p. 116 409, 2020. doi: 10.1016/j.energy.2019.116409.

[63] D. Chen, Y. Kim, and A. G. Stefanopoulou, "Predictive Equivalent Consumption Minimization Strategy With Segmented Traffic Information," *IEEE Transactions on Vehicular Technology*, vol. 69, no. 12, pp. 14 377–14 390, 2020. doi: 10.1109/TVT.2020.3034552.

[64] C. Sun, F. Sun, and H. He, "Investigating adaptive-ECMS with velocity forecast ability for hybrid electric vehicles," *Applied Energy*, vol. 185, pp. 1644–1653, 2017. doi: 10.1016/j.apenergy.2016.02.026.

[65] J. Soldo, B. Skugor, and J. Deur, "Optimal Energy Management Control of a Parallel Plug-In Hybrid Electric Vehicle in the Presence of Low Emission Zones," SAE Technical Paper 2019-01-1215, 2019. doi: 10.4271/2019-01-1215.

[66] R. Bellman, "On the Theory of Dynamic Programming," *Proc Natl Acad Sci U S A*, vol. 38, no. 8, pp. 716–719, 1952, ISSN 0027-8424.

[67] ——, "The theory of dynamic programming," *Bull. Amer. Math. Soc.*, vol. 60, no. 6, pp. 503–516, 1954, ISSN 0002-9904. doi: 10.1090/S0002-9904-1954-09848-8.

[68] ——, "Dynamic Programming," *Science*, vol. 153, no. 3731, pp. 34–37, 1966. doi: 10.1126/science.153.3731.34.

[69] M. Back, M. Simons, F. Kirschaum, and V. Krebs, "Predictive Control Of Drivetrains," *IFAC Proceedings Volumes*, 15th IFAC World Congress, vol. 35, no. 1, pp. 241–246, 2002, ISSN 1474-6670. doi: 10.3182/20020721-6-ES-1901.01508.

[70] J. Scordia, M. D. Renaudin, R. Trigui, B. Jeanneret, *et al.*, "Global optimisation of energy management laws in hybrid vehicles using dynamic programming," *International Journal of Vehicle Design (IJVD)*, vol. 39, no. 4, p. 349, 2005, ISSN 0143 - 3369 , 1741 - 5314. doi: 10.1504/IJVD.2005.008467.

[71] R. Wang and S. M. Lukic, "Dynamic programming technique in hybrid electric vehicle optimization," *2012 IEEE International Electric Vehicle Conference*, 2012, pp. 1–8. doi: 10.1109/IEVC.2012.6183284.

[72] E. Vinot and R. Trigui, "Optimal energy management of HEVs with hybrid storage system," *Energy Conversion and Management*, vol. 76, pp. 437–452, 2013, ISSN 0196-8904. doi: 10.1016/j.enconman.2013.07.065.

[73] A. Panday and H. O. Bansal, "A Review of Optimal Energy Management Strategies for Hybrid Electric Vehicle," *International Journal of Vehicular Technology*, vol. 2014, p. 19, 2014, ISSN 1687-5702. doi: 10.1155/2014/160510.

[74] X. Wang, H. He, F. Sun, and J. Zhang, "Application Study on the Dynamic Programming Algorithm for Energy Management of Plug-in Hybrid Electric Vehicles," *Energies*, vol. 8, no. 4, pp. 3225–3244, 2015, ISSN 1996-1073. doi: 10.3390/en8043225.

[75] L. Bruck, A. Lempert, S. Amirfarhangi Bonab, J. Lempert, *et al.*, "A Dynamic Programming Algorithm for HEV Powertrains Using Battery Power as State Variable," SAE Technical Paper 2020-01-0271, 2020. doi: 10.4271/2020-01-0271.

[76] M. R. Khan, M. J. Swierczynski, and S. K. Kær, "Towards an Ultimate Battery Thermal Management System: A Review," *Batteries*, vol. 3, no. 1, p. 9, 2017. doi: 10.3390/batteries3010009.

[77] L. Lefebvre, "Smart Battery Thermal Management for PHEV Efficiency," *Oil Gas Sci. Technol. – Rev. IFP Energies nouvelles*, vol. 68, no. 1, pp. 149–164, 2013, ISSN 1294-4475,1953-8189. doi: 10.2516/ogst/2012076.

[78] C. Zhu, F. Lu, H. Zhang, J. Sun, *et al.*, "A Real-Time Battery Thermal Management Strategy for Connected and Automated Hybrid Electric Vehicles (CAHEVs) Based on Iterative Dynamic Programming," *IEEE Transactions on Vehicular Technology*, vol. 67, no. 9, pp. 8077–8084, 2018, ISSN 1939-9359. doi: 10.1109/TVT.2018.2844368.

[79] L. Tang, G. Rizzoni, and M. Lukas, "Comparison of dynamic programming-based energy management strategies including battery life optimization," *2016 International Conference on Electrical Systems for Aircraft, Railway, Ship Propulsion and Road Vehicles International Transportation Electrification Conference (ESARS-ITEC)*, 2016, pp. 1–6. doi: 10.1109/ESARS-ITEC.2016.7841430.

[80] L. Tang and G. Rizzoni, "Energy management strategy including battery life optimization for a HEV with a CVT," *2016 IEEE Transportation Electrification Conference and Expo, Asia-Pacific (ITEC Asia-Pacific)*, 2016, pp. 549–554. doi: 10.1109/ITEC-AP.2016.7513014.

[81] E. F. Camacho and C. B. Alba, *Model Predictive Control*, 2nd ed., ser. Advanced Textbooks in Control and Signal Processing. London: Springer-Verlag, 2007, ISBN 978-1-85233-694-3. doi: 10.1007/978-0-85729-398-5.

[82] H. Zomorodi, D. Yoon, and B. Ayalew, "Use of predictive information for battery pack thermal management," *2017 American Control Conference (ACC)*, 2017, pp. 5020–5025. doi: 10.23919/ACC.2017.7963733.

[83] H. Esen, T. Tashiro, D. Bernardini, and A. Bemporad, "Cabin heat thermal management in hybrid vehicles using model predictive control," *22nd Mediterranean Conference on Control and Automation*, 2014, pp. 49–54. doi: 10.1109/MED.2014.6961325.

[84] D. Sabadka, V. Molnár, and G. Fedorko, "Shortening of Life Cycle and Complexity Impact on the Automotive Industry," *TEM Journal*, vol. 8, no. 4, pp. 1295–1301, 2019. doi: 10.18421/TEM84-27.

[85] C. Morley, "Automotive Industry Life Cycle Analysis: Shorter Timelines," Survey, 2018. [Online]. Available: https://www.jabil.com/blog/automotive-industry-trends-point-to-shorter-product-development-cycles.html.

[86] W. Wachenfeld and H. Winner, "The release of autonomous vehicles," *Autonomous Driving: Technical, Legal and Social Aspects*. 2016, ISBN 978-3-662-48847-8. doi: 10.1007/978-3-662-48847-8_21.

[87] J. Andert, F. Xia, S. Klein, D. Guse, *et al.*, "Road-to-rig-to-desktop: Virtual development using real-time engine modelling and powertrain co-simulation," *International Journal of Engine Research*, vol. 20, no. 7, pp. 686–695, 2019. doi: 10.1177/1468087418767221.

[88] M. Tideman and M. van Noort, "A simulation tool suite for developing connected vehicle systems," *2013 IEEE Intelligent Vehicles Symposium (IV)*, 2013, pp. 713–718. doi: 10.1109/IVS.2013.6629551.

[89] M. Aramrattana, T. Larsson, J. Jansson, and A. Nåbo, "A simulation framework for cooperative intelligent transport systems testing and evaluation," *Transportation Research Part F: Traffic Psychology and Behaviour*, Special TRF issue: Driving simulation, vol. 61, pp. 268–280, 2019, ISSN 1369-8478. doi: 10.1016/j.trf.2017.08.004.

[90] F. Xu and T. Shen, "Look-Ahead Prediction-Based Real-Time Optimal Energy Management for Connected HEVs," *IEEE Transactions on Vehicular Technology*, vol. 69, no. 3, pp. 2537–2551, 2020, ISSN 1939-9359. doi: 10.1109/TVT.2020.2965163.

[91] T. Grahle, M. Tonne, A. Wiedersberg, and T. Zsebedits, "Regeneration of the Particulate Filter by Using Navigation Data," *MTZ Worldwide*, vol. 77, no. 1, pp. 16–21, 2016. doi: 10.1007/s38313-015-0078-7.

[92] M. Hopka, D. Upadhyay, and M. Van Nieuwstadt, "Smart DPF Regenerations - A Case Study of a Connected Powertrain Function," *SAE International Journal of Advances and Current Practices in Mobility*, vol. 1, no. 2, pp. 762–770, 2019, ISSN 2641-9637. doi: 10.4271/2019-01-0316.

[93] M. Menarini, P. Marrancone, G. Cecchini, A. Bazzi, *et al.*, "TRUDI: Testing Environment for Vehicular Applications Running with Devices in the Loop," *2019 IEEE International Conference on Connected Vehicles and Expo (ICCVE)*, 2019, pp. 1–6. doi: 10.1109/ICCVE45908.2019.8965152.

[94] Z. Szendrei, N. Varga, and L. Bokor, "A SUMO-Based Hardware-in-the-Loop V2X Simulation Framework for Testing and Rapid Prototyping of Cooperative Vehicular Applications," *Vehicle and Automotive Engineering 2*, 2018, pp. 426–440, ISBN 978-3-319-75677-6. doi: 10.1007/978-3-319-75677-6_37.

[95] Ş. Y. Gelbal, S. Tamilarasan, M. R. Cantaş, L. Güvenç, *et al.*, "A connected and autonomous vehicle hardware-in-the-loop simulator for developing automated driving algorithms," *2017 IEEE International Conference on Systems, Man, and Cybernetics (SMC)*, 2017, pp. 3397–3402. doi: 10.1109/SMC.2017.8123155.

[96] Y. Shao, M. A. Mohd Zulkefli, Z. Sun, and P. Huang, "Evaluating connected and autonomous vehicles using a hardware-in-the-loop testbed and a living lab," *Transportation Research Part C: Emerging Technologies*, vol. 102, pp. 121–135, 2019, ISSN 0968-090X. doi: 10.1016/j.trc.2019.03.010.

[97] J. Ma, F. Zhou, Z. Huang, and R. James, "Hardware-In-The-Loop Testing of Connected and Automated Vehicle Applications: A Use Case For Cooperative Adaptive Cruise Control," *2018 21st International Conference on Intelligent Transportation Systems (ITSC)*, 2018, pp. 2878–2883. doi: 10.1109/ITSC.2018.8569753.

[98] A. Capancioni, L. Brunelli, N. Cavina, and A. Perazzo, "Development of Adaptive-ECMS and predictive functions for Plug-in HEVs to handle Zero-Emission Zones using navigation data," SAE Technical Paper 2021-24-0105, 2021. doi: 10.4271/2021-24-0105.

[99] G. Caramia, N. Cavina, A. Capancioni, M. Caggiano, *et al.*, "Combined Optimization of Energy and Battery Thermal Management Control for a Plug-in HEV," SAE Technical Paper 2019-24-0249, 2019. doi: 10.4271/2019-24-0249.

[100] L. Brunelli, A. Capancioni, P. Gonnella, R. Casadio, *et al.*, "A Hybrid Vehicle Hardware-in-the-Loop System With Integrated Connectivity for Ehorizon Functions Validation," *IEEE Transactions on Vehicular Technology*, vol. 70, no. 5, pp. 4340–4352, 2021. doi: 10.1109/TVT.2021.3073807.

[101] H. Beglerovic, S. Metzner, and M. Horn, "Challenges for the Validation and Testing of Automated Driving Functions," *Advanced Microsystems for Automotive Applications 2017*, 2018, pp. 179–187. doi: 10.1007/978-3-319-66972-4_15.

[102] N. Cavina, G. Caramia, S. Patassa, and M. Caggiano, "Predictive Energy Management Strategies for Hybrid Electric Vehicles: Fuel Economy Improvement and Battery Capacity Sensitivity Analysis," SAE Technical Paper 2018-01-0998, 2018. doi: 10.4271/2018-01-0998.

[103] G. Caramia, N. Cavina, M. Caggiano, S. Patassa, *et al.*, "Battery state of charge management strategies for a real-time controller of a Plug-in Hybrid Electric Vehicle," *Energy Procedia*, vol. 148, pp. 258–265, 2018. doi: 10.1016/j.egypro.2018.08.076.

[104] M. Shams-Zahraei, A. Z. Kouzani, S. Kutter, and B. Bäker, "Integrated thermal and energy management of plug-in hybrid electric vehicles," *Journal of Power Sources*, vol. 216, pp. 237–248, 2012, ISSN 03787753. doi: 10.1016/j.jpowsour.2012.05.055.

[105] T. M. Padovani, M. Debert, G. Colin, and Y. Chamaillard, "Optimal Energy Management Strategy including Battery Health through Thermal Management for Hybrid Vehicles," *IFAC Proceedings Volumes*, vol. 46, no. 21, pp. 384–389, 2013, ISSN 14746670. doi: 10.3182/20130904-4-JP-2042.00137.

[106] R. Parenti, S. Mazzetti, F. Belletti, F.-W. Speckens, *et al.*, "Will the 95g/km Limit Affect Fun and Emotion? The Lamborghini Answer," *Fahrzeug- und Motorentechnik : 24. Aachen Colloquium; October 5th - 7th, 2015, Eurogress Aachen, Germany*, 2015, ISBN 978-3-00-049205-1. [Online]. Available: http://www.gbv.de/dms/tib-ub-hannover/838524583.pdf.

[107] "ISO 10521-1:2006 - Road vehicles — Road load — Part 1: Determination under reference atmospheric conditions," 2006, p. 30. [Online]. Available: https://www.iso.org/standard/37533.html.

[108] İ. Dinçer, H. S. Hamut, and N. Javani, *Thermal management of electric vehicle battery systems*, ser. Automotive Series. John Wiley & Sons, Inc, 2017, ISBN 978-1-118-90024-6.

[109] H. He, R. Xiong, H. Guo, and S. Li, "Comparison study on the battery models used for the energy management of batteries in electric vehicles," *Energy Conversion and Management*, vol. 64, pp. 113–121, 2012. doi: 10.1016/j.enconman.2012.04.014.

[110] X. Hu, S. Li, and H. Peng, "A comparative study of equivalent circuit models for Li-ion batteries," *Journal of Power Sources*, vol. 198, pp. 359–367, 2012. doi: 10.1016/j.jpowsour.2011.10.013.

[111] R. Xiong and W. Shen, *Advanced Battery Management Technologies for Electric Vehicles*, ser. Automotive Series. Wiley, 2019, 400 pp., ISBN 978-1-119-48164-5.

[112] J. D'Errico. "Fminsearchbnd, fminsearchcon," MATLAB Central File Exchange. (2012), [Online]. Available: https://it.mathworks.com/matlabcentral/fileexchange/8277-fminsearchbnd-fminsearchcon.

[113] N. Nieto, L. Díaz, J. Gastelurrutia, I. Alava, *et al.*, "Thermal Modeling of Large Format Lithium-Ion Cells," *J. Electrochem. Soc.*, vol. 160, no. 2, A212–A217, 2013. doi: 10.1149/2.042302jes.

[114] B. Pollak, P. Ebner, C. Schyr, T. Pels, *et al.*, "Consistent Development Methodology for hybrid AWD powertrains," SAE Technical Paper 2008-28-0003, 2008. doi: 10.4271/2008-28-0003.

[115] A. Rabofsky, C. Walther, J. Rothdeutsch, R. Hanfstingl, *et al.*, "Electrical and Hybrid Drive Lines: New Demands for N&V Integration," SAE Technical Paper 2010-01-1403, 2010. doi: 10.4271/2010-01-1403.

[116] European Commission, "Regulation No 101 of the Economic Commission for Europe of the United Nations (UN/ECE) — Uniform provisions concerning the approval of passenger cars powered by an internal combustion engine only, or powered by a hybrid electric power train with regard to the measurement of the emission of carbon dioxide and fuel consumption and/or the measurement of electric energy consumption and electric range, and of categories M1 and N1 vehicles powered by an electric power train only with regard to the measurement of electric energy consumption and electric range," Regulation (EU) 2012/101, 2012. [Online]. Available: https://eur-lex.europa.eu/legal-content/IT/TXT/?uri=CELEX%3A42012X0526%2801%29.

[117] "MicroAutoBox II," dSPACE. (), [Online]. Available: https://www.dspace.com/en/inc/home/products/hw/micautob/microautobox2.cfm.

[118] "MIRACLE2," Alma Automotive. (), [Online]. Available: https://www.alma-automotive.it/en/products/rapid-control-prototyping/miracle2-013.

[119] J. Santa, F. Pereñíguez, A. Moragón, and A. F. Skarmeta, "Experimental evaluation of CAM and DENM messaging services in vehicular communications," *Transportation Research Part C: Emerging Technologies*, vol. 46, pp. 98–120, 2014, ISSN 0968-090X. doi: 10.1016/j.trc.2014.05.006. [Online]. Available: https://www.sciencedirect.com/science/article/pii/S0968090X14001193.

[120] "APU3C4," PC Engines. (), [Online]. Available: https://www.pcengines.ch/apu3c4.htm.

[121] M. Boccolini, "Development of a speed profile prediction algorithm based on navigation data for energy management optimization," Master's thesis, University of Bologna, 2021. [Online]. Available: https://amslaurea.unibo.it/22543/.

[122] S. Lefèvre, C. Sun, R. Bajcsy, and C. Laugier, "Comparison of parametric and non-parametric approaches for vehicle speed prediction," *2014 American Control Conference*, ISSN: 2378-5861, 2014, pp. 3494–3499. doi: 10.1109/ACC.2014.6858871.

[123] K. Liu, Z. Asher, X. Gong, M. Huang, *et al.*, "Vehicle Velocity Prediction and Energy Management Strategy Part 1: Deterministic and Stochastic Vehicle Velocity Prediction Using Machine Learning," SAE Technical Paper 2019-01-1051, 2019. doi: 10.4271/2019-01-1051.

[124] "SAE J2951: Drive Quality Evaluation for Chassis Dynamometer Testing," SAE J2951:201401, 2014. [Online]. Available: https://www.sae.org/standards/content/j2951_201401/.

[125] C. Musardo, G. Rizzoni, Y. Guezennec, and B. Staccia, "A-ECMS: An Adaptive Algorithm for Hybrid Electric Vehicle Energy Management," *European Journal of Control*, vol. 11, no. 4, pp. 509–524, 2005. doi: 10.3166/ejc.11.509-524.

[126] S. Onori, L. Serrao, and G. Rizzoni, "Adaptive equivalent consumption minimization strategy for hybrid electric vehicles," *ASME 2010 Dynamic Systems and Control Conference, Volume 1*, 2010, pp. 499–505. doi: 10.1115/DSCC2010-4211.

[127] D. P. Bertsekas, *Dynamic Programming and Optimal Control*, 1st ed. Athena Scientific, 1995.

[128] European Commission, "Worldwide harmonised Light-duty vehicles Test Procedure (WLTP) and Real Driving Emissions (RDE)," Regulation (EU) 2017/1151, 2017. [Online]. Available: https://eur-lex.europa.eu/legal-content/EN/TXT/?uri=LEGISSUM:4390810.